

THE INTERACTION OF NEPTUNE WITH THE SOLAR WIND

by

ADAM SZABO

B.A. Physics, The University of Chicago
(1988)

SUBMITTED TO THE DEPARTMENT OF PHYSICS
IN PARTIAL FULFILLMENT OF THE REQUIREMENTS
FOR THE DEGREE OF
DOCTORATE OF PHILOSOPHY IN PHYSICS

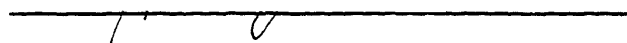
at the

MASSACHUSETTS INSTITUTE OF TECHNOLOGY

August, 1993

© Massachusetts Institute of Technology 1993
All rights reserved

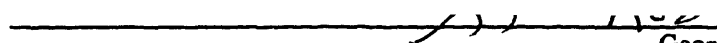
Signature of Author


Department of Physics
August, 1993

Certified by


John W. Belcher
Professor, Physics
Thesis Supervisor

Accepted by


George F. Koster, Chairman
Graduate Committee
Department of Physics

ARCHIVES

MASSACHUSETTS INSTITUTE
OF TECHNOLOGY

NOV 02 1993

LIBRARIES

THE INTERACTION OF NEPTUNE WITH THE SOLAR WIND

by

ADAM SZABO

Submitted to the Department of Physics on August 9, 1993, in partial fulfillment of the requirements for the Degree of Doctor of Philosophy.

ABSTRACT

The Voyager 2 encounter with Neptune in August 1989 allowed the detailed study of the interaction of the solar wind with the furthest of the giant planets of our solar system. The low-energy plasma and magnetic field data obtained by Voyager 2 in the subsolar interaction regions of Neptune is analyzed and discussed in this thesis. Theoretical models which may account for the observed phenomena are proposed.

As the supersonic solar wind approaches the magnetic obstacle of Neptune, it cannot smoothly flow around the magnetosphere of the planet, but forms a magnetohydrodynamic (MHD) shock, the bow shock. To enhance the analysis of the bow shock, the non-linear least squares, MHD jump conditions fitting technique of *Viñas and Scudder [1986]* is extended to include plasma temperature observations in the form of the conservation of the normal momentum flux and energy density flux. The improved analysis technique reveals that the nearly subsolar Neptunian bow shock is a low β , high Mach number, quasi-perpendicular strong shock slowly moving away from the planet toward the Sun. Also, the shock microstructure features are resolved and presented. The shock foot, overshoot region and magnitude, and downstream damped oscillation wavelength are in good agreement with model predictions and with observations at other planetary systems. However, the ramp region appears significantly thicker than expected, which can be explained by an anomalously high electron resistivity.

After crossing the bow shock, the now subsonic and heated solar wind plasma passes through the turbulent magnetosheath before reaching the boundary of the planet's magnetosphere, the magnetopause (MP). The observed magnetofluid parameters in the inbound sheath are well modeled by a simple gas dynamic simulation with convected magnetic fields. Significant discrepancies are observed by Voyager 2 only near the MP crossing. Because of the relatively large tilt angle of the Neptunian magnetic dipole axis from the planet's rotation axis, the southern magnetic polar regions face into the solar wind flow for a short period of time in every planetary rotation. Voyager 2 had the good fortune to encounter Neptune's MP at such a configuration. To analyze this unusually positioned planetary MP, the traditional magnetic variance analysis is supplemented by a newly developed MHD rotational discontinuity fitting method. The two independent techniques agree that the Neptunian MP is a rotational or rotational-like discontinuity allowing the flow of sheath plasma into the upper regions of the magnetosphere. This observation of the open magnetosphere provides a possible explanation for the deviations observed near the MP from the predictions of the gas dynamic model which assumes an impenetrable magnetosphere.

The magnetic variance and MHD techniques, however, yield widely different results for the orientation of the MP surface normal. A model is proposed which includes surface ripples on the MP boundary and thus provides a mechanism to resolve this apparent discrepancy.

Finally, the observed sheath plasma in the upper regions of the Neptunian magnetosphere is shown to form a layer similar in characteristics to the Earth's entry layer. Deeper in the magnetosphere, this boundary layer exhibits characteristics of a plasma mantle region thus suggesting a source for the plasma supply of the previously observed tailside plasma mantle.

Thesis Supervisor: John W. Belcher

Title: Professor of Physics

TABLE OF CONTENTS

Chapter 1. The Voyager 2 Spacecraft at Neptune	6
1.1 Introduction	6
1.2 The Voyager 2 Spacecraft	7
1.2.1 The Voyager 2 PLS Instrument	9
1.2.2 The Basic Data Processing	12
1.2.3 The MAG Experiment	17
1.3 The General Structure of Solar Wind Interaction with Magnetospheres	18
1.3.1 The Voyager 2 Trajectory During the Neptune Encounter	21
Chapter 2. The Neptune Inbound Bow Shock	26
2.1 Introduction	26
2.2 The MHD Fitting Technique	26
2.2.1 The Technique	27
2.2.2 Analysis of Synthetic Shocks	41
2.2.3 Confidence Regions in the MHD Fit Method	48
2.3 The MHD Characteristics of the Shock	50
2.4 The Shock Microstructure	56
Chapter 3. The Inbound Magnetosheath	64
3.1 Introduction	64
3.2 The Gas Dynamic Model of the Sheath	65
3.3 Voyager 2 Observations of the Sheath	68
Chapter 4. The Subsolar Magnetopause and Cusp	74

4.1 Introduction	74
4.2 The MHD Fitting Technique	75
4.3 The Magnetic Variance Technique	86
4.4 Physical and Geometrical Properties of the MP	89
4.5 The Cusp: Entry Layer or Mantle?	99
Chapter 5. Conclusions	107
References for Chapter 1	111
References for Chapter 2	114
References for Chapter 3	118
References for Chapter 4	120
References for Chapter 5	122
Acknowledgements	124
Biography	125

CHAPTER 1

THE VOYAGER 2 SPACECRAFT AT NEPTUNE

1.1 Introduction

The extended mission of Voyager 2 brought the spacecraft to its closest approach to Neptune on August 25, 1989. During the encounter of this planetary system, Voyager 2 discovered that Neptune has a substantial planetary magnetic field and a fully developed magnetosphere [Belcher *et al.*, 1989; Ness *et al.*, 1989]. The Plasma Science (PLS) experiment is one of the eleven scientific investigations on board of the spacecraft, and was used to measure low-energy plasma in the magnetosphere as well as in the interplanetary medium. This instrument obtained a large amount of data relevant to the study of the plasma physics of the interaction between the solar wind and the Neptunian magnetosphere.

In this work, we concentrate on plasma phenomena, found in the solar wind and in the outer dayside regions of the Neptunian magnetosphere, which are caused by the interaction of the solar wind and the magnetosphere. Though the interaction of the solar wind with other planetary magnetospheres has already been extensively studied, Neptune presents a very unique configuration of this interaction worthy of our attention. Thus this study promises not just simply to add a new member to the list of already analyzed planetary systems, but also to provide an opportunity to compare the observations from other planets (primarily from Earth) to a previously unseen scenario, and to check the validity of various theories over an extended range of configurations.

Chapter 1 describes the Voyager spacecraft and the PLS and magnetometer (MAG) experiments. Also a brief review of the solar wind - magnetosphere interaction regions is given, and the Voyager 2 trajectory at Neptune is fully described. In Chapter 2, the details of

our magnetohydrodynamic (MHD) shock jump condition fitting technique is given. This new method is employed to analyze the inbound bow shock, and we describe both the macro and microscale features found there. In Chapter 3, we follow the solar wind flow through the shocked region of the subsolar magnetosheath and the observations are compared to the predictions of gas dynamic modeling. Finally, the encounter with the high magnetic latitude magnetopause and cusp regions are analyzed in Chapter 4.

1.2 The Voyager 2 Spacecraft

The Voyager 2 spacecraft was launched by a Titan III/Centaur launch vehicle from Cape Canaveral, Florida on 20 August, 1977. It carries a high-gain antenna, an electric power generator, and eleven science instruments. The nuclear-fueled Voyager spacecraft uses three radioisotope thermoelectric generator (RTGs), which, at launch time, generated a minimum total power of 384 watts, sufficient to power the craft well into the next century. The eleven science investigations and their abbreviations, instruments, and measurement limits are listed in Table 1.1. In this work, we focus on the observations of the MIT plasma science (PLS) instrument built under the leadership of Professor Herbert S. Bridge, and for which the current principal investigator is Professor John W. Belcher.

Voyager 2 is one of the most successful spacecraft built by NASA. During a decade of voyage it encountered all of the four gas giants of our solar system (Jupiter, Saturn, Uranus, and Neptune). And after 16 years of operation, all of the instruments and engineering subsystems are still functional. The spacecraft is currently at 40 AU heading toward the local interstellar medium in search of the heliopause, the boundary between the heliosphere and the local interstellar medium.

Table 1.1 Voyager Science Investigations

Investigation Team	Instrument	Measurement
Imaging science (ISS)	Se-S vidicon cameras	Imaging of planets, satellites, and rings
Infrared spectroscopy and radiometry (IRIS)	Michelson interferometer and radiometer	Spectrum of infrared emission (3.3–50 μm and 0.33–2 μm)
Photopolarimetry (PPS)	Photometer and polarimeter	Polarized Ultraviolet emission (2350–7500 <i>angstrom</i>)
Ultraviolet spectroscopy (UVS)	Grating spectrometer	Spectrum of ultraviolet emission (500–1700 <i>angstrom</i>)
Radio science (RSS)	Radio oscillator	Coherent radio Doppler shift and ranging at 2.3 GHz and 8.4 GHz
Magnetic fields (MAG)	Triaxial fluxgate magnetometer	Magnetic fields (6×10^{-8} –20 G)
Plasma (PLS)	Modulated grid Faraday cup	Energy spectrum of ions and electrons (10–6000 eV/charge)
Plasma wave (PWS)	Electric linear antenna	Wave spectrum of plasma oscillations (10 Hz–56 kHz)
Planetary radio astronomy (PRA)	Electric linear antenna	Radio spectrum of planetary emission (1.2 kHz–40.5 MHz)
Low-energy charged particles (LECP)	Solid-state particle detector	Energy spectrum of charged particles (28 keV–150 MeV for ions and 22 keV–20 MeV for electrons)
Cosmic rays (CRS)	Solid-state particle detector	Energetic particles and cosmic rays (3–110 MeV for electrons and 1–500 MeV for ions)

1.2.1 The Voyager 2 PLS Instrument

The Voyager 2 PLS instrument was designed to measure low-energy positive ions and electrons in the solar wind and in planetary magnetospheres. The instrument is fully described in *Bridge et al.*, [1977]. It consists of four modulated-grid Faraday cup detectors, each of which samples velocity space in a different direction. Three of them (the "A", "B", and "C" cups), which are electrically and physically arranged into a single main sensor, point roughly toward the Earth and the Sun, allowing 3-dimensional plasma measurement of the nearly anti-sunward moving supersonic solar wind. The fourth detector (the "D" cup) points perpendicular to the Earth-spacecraft line, thus with proper roll of the spacecraft, this detector can sample corotating plasma in the planetary magnetospheres. This side sensor is also the only one capable of detecting electrons.

Each of the Faraday cups contains a collector plate and several grids. A composite ac-dc electric potential is applied to one of the grids, the modulator grid. This retarding potential forms a variable lower energy limit a particle must have in order to reach the collector. By taking the difference between the particle flux at the upper and lower value of the potential, we gain the differential particle flux in that energy window. This differential flux is measured in the form of current on the collector plate, amplified, and transmitted back to Earth. By varying the upper and lower limits of the electric potential on the modulator grid we are effectively changing the energy window and obtaining spectra of particle flux versus energy-per-charge. The instrument range of energy-per-charge for both positively and negatively charged particles is 10 V to 5950 V. As mentioned earlier, only the side or "D" cup is capable of measuring the negatively charged electron distribution.

The geometrical structure of the Faraday cups is quite shallow. Therefore, the full field of view of an individual sensor, corresponding to the angular range the charged particles can

reach the collector, is quite large. The half angle of the view cone is 45° for the main sensor Faraday cups. However, the conical field of view of the side sensor is somewhat narrower with a half angle of 30° . These large field-of-view detectors are very suitable for the three-axis stabilized Voyager spacecraft because no scanning is required to measure the solar wind and magnetosheath plasmas. On the other hand, the instrument measures the total particle flux into the cup from many different directions in a given energy-per-charge window; the plasma angular distribution is convolved with the instrument response, and therefore information about many details of the distribution function are lost. This is particularly true of the electron measurements, which are made only in the side sensor.

For positive ions, measurements are made simultaneously in all of the Faraday cups with two sequential energy-per-charge scans used over the entire range of 10 V to 5950 V. The low resolution mode (L mode) consists of 16 contiguous voltage windows with an energy-per-charge resolution $\Delta E/E \approx 29\%$; the high resolution mode (M mode) consists of 128 voltage windows with $\Delta E/E \approx 3.6\%$. During the Neptune encounter the L mode had two sampling schemes: one with a short integration time of 210 ms (L-short) and the other with a longer integration time of 930 ms (L-long). The integration time for the M mode measurements is 930 ms. Electrons are measured only in the side sensor in two energy ranges: the low energy E1 mode (10-140 V) and the high energy E2 mode (10-5959 V). Both electron modes are composed of 16 energy windows, and like the L mode, both the E1 and E2 modes have two integration time schemes: a 210 ms short mode (E1-short and E2-short) and a 930 ms long mode (E1-long and E2-long).

The measurement sequence used during the Neptune encounter is tabulated in Table 1.2 [Sittler *et al.*, 1987]. Each frame is 48 seconds long. There are 15 frames in a 12 minute measurement cycle. One M mode spectrum is obtained every 12 minutes with 25 L mode spectra in between. Twelve of these L modes are obtained with the short integration scheme,

**Table 1.2 Voyager PLS Measurement Sequence
During the Neptune Encounter**

Frame (48 s)	Modes			
1	L-short	E1-short	L-long	E2-long
2	L-short	E2-short	L-long	E1-long
3-12	Above frames repeat 5 more times			
13-14	M			
15	M(cont.)		L-long	

L is low resolution mode

M is high resolution mode (integration time 930 ms)

E1 is low energy electron mode

E2 is high energy electron mode

Short means short integration time (210 ms)

Long means long integration time (930 ms)

which have a very poor signal to noise ratio, and thus are usually discarded in our analysis. Therefore, the effective time resolution for the L mode spectra is slightly less than one per minute. The two electron modes, E1 and E2, are made alternatively in the frames 1 to 12, as shown in Table 1.2. Of all the 12 pairs of E1 and E2 spectra, 6 use the short time integration scheme and are usually discarded due to the low signal to noise ratio. Thus the effective time resolution of the electron measurements is about 96 seconds. In addition, during the Neptune encounter, the PLS data suffered a systematic noise contamination due to interference from other instruments on board the spacecraft. This contamination effects some of the spectra in frames 2, 3, 10 and 11 which have to be discarded.

1.2.2 The Basic Data Processing

The basic PLS data is electric current from the collector plates of the various detectors as a function of the energy-per-charge windows defined by the varying electric potential on the modulator grid. The PLS data processing effort characterizes the plasma distribution function in velocity space from the discrete set of measured currents and then derives magnetohydrodynamic plasma parameters such as plasma density, temperature, and bulk velocity for the observed particle species.

The relationship between the plasma distribution function and the measured currents are explicitly described by *Vasyliunas* [1971], and *Belcher et al.* [1980]. Consider a particle species of atomic number A_a and charge state Z_a with a given velocity distribution function $f_a(v)$. Let I_k be the electric current in the k -th energy window which has a lower potential of Φ_k and an upper potential Φ_{k+1} , and therefore selects particles with speeds normal to the detector surface between $u_k = \sqrt{2Z_a e \Phi_k / A_a m_p}$ and $u_{k+1} = \sqrt{2Z_a e \Phi_{k+1} / A_a m_p}$, where e and m_p are the charge and mass of a proton, respectively. Then the contribution of the particle species a to I_k is

$$I_k = Z_a e S \int_{u_k}^{u_{k+1}} dv_n \int_{-\infty}^{+\infty} \int_{-\infty}^{+\infty} dv_t f_a(v) G(v, \hat{n}) \quad (1.1)$$

where S is the effective area of the entrance aperture of the detector at normal incidence, v_n and v_t are the normal and tangential components of the velocity to the detector, and $G(v, \hat{n})$ is the response function of the detector whose axis lies along the unit vector \hat{n} . The response function is determined by the geometry of the instrument and the charge-to-mass ratio of the particle. The response functions of the main and side sensors were determined by *Barnett and Olbert* [1986], and are used in all of our calculations.

Next we have to answer what information about the plasma can be obtained from the measured currents. Since the solar wind plasma is collisionless [see for example *Olbert*, 1969], in the sense that the mean free path for Coulomb collisions is much longer than the characteristic macroscopic length scales, there is no *a priori* reason to expect any kind of thermodynamic equilibrium or applicability of the temperature concept. A complete description of the plasma requires the specification of the velocity distribution function for each species of particles present. Nevertheless, it has been found empirically that, at least in the solar wind and magnetosheath, the plasma can be described to a surprisingly adequate extent for many purposes by specifying only its hydrodynamic parameters: density, bulk velocity, pressure tensor, and sometimes the heat flux vector [*Vasyliunas*, 1971]. These may have to be specified separately for each species of particles. Charge neutrality requires that the number densities of positive and negative particles be equal to a very high approximation. We also assume that the bulk velocities of the positive and negative particles are the same, which has been shown observationally to be a good approximation. But the pressures and heat fluxes for individual species may very well be different. Much of the plasma analysis consists of determining these hydrodynamic parameters which are the moments of the velocity distribution function $f_a(v)$. If n is the number density, V the bulk velocity, P the pressure tensor, and q the heat flux

vector, then these parameters are defined for each species by

$$n = \int d\mathbf{v} f(\mathbf{v}) \quad (1.2)$$

$$n\mathbf{V} = \int d\mathbf{v} \mathbf{v} f(\mathbf{v}) \quad (1.3)$$

$$\tilde{\mathbf{P}} = m \int d\mathbf{v} f(\mathbf{v})(\mathbf{v} - \mathbf{V})(\mathbf{v} - \mathbf{V}) \quad (1.4)$$

$$\mathbf{q} = \frac{1}{2}m \int d\mathbf{v} f(\mathbf{v})(\mathbf{v} - \mathbf{V})|\mathbf{v} - \mathbf{V}|^2 \quad (1.5)$$

where all the integrals are volume integrals over velocity space. All space plasmas contain magnetic field and the pressure tensor is usually assumed to be axially symmetric:

$$\tilde{\mathbf{P}} = P_{\perp}\tilde{\mathbf{I}} + (P_{\parallel} - P_{\perp})\hat{\mathbf{b}}\hat{\mathbf{b}} \quad (1.6)$$

where $\tilde{\mathbf{I}}$ is the unit dyadic and $\hat{\mathbf{b}}$ is the unit vector in the direction of the magnetic field. Though in space plasmas anisotropic pressures are often observed, the low densities at the Neptunian environment prohibits us to estimate the degree of anisotropy. Therefore, throughout our analysis we are assuming an isotropic plasma condition where the pressure tensor becomes purely diagonal and can be represented by a scalar quantity P :

$$\tilde{\mathbf{P}} = P\tilde{\mathbf{I}} \quad (1.7)$$

Then we define the "temperature" as the ratio $kT=P/n$. The use of the term "temperature" does not in any way imply the existence of thermal equilibrium or a Maxwellian velocity distribution.

At this point, if we can find the appropriate functional form of the velocity distribution function, then we can fit it to the observed currents in the detectors using a non-linear least squares fitting technique. The obtained best fit constrains the adjustable parameters in the chosen distribution function, and substituting this result into the definitions of the plasma parameters, equations (1.2) - (1.5), gives the hydrodynamic description of the plasma. In the solar wind, we are using a convected Maxwellian as our fitting function:

$$f(\mathbf{v}) = \frac{n}{\pi^{3/2}w^3} \exp\left\{-\frac{(\mathbf{v} - \mathbf{V})^2}{w^2}\right\} \quad (1.8)$$

where the adjustable parameters are the density n , bulk velocity \mathbf{V} , and the most probable speed w , which is related to the temperature T by $kT = \frac{1}{2}mw^2$. This simple model function fits the solar wind observations very well and was historically the first to be used [Scherb, 1964]. However, the ion distributions in the dayside magnetosheath are often not well represented by a single Maxwellian distribution. The data from many early Earth orbiting satellites indicate that the ion distributions in the magnetosheath have high-energy tails [Howe, 1970; Hundhausen et al., 1969; Wolfe and McKibben, 1968; Montgomery et al., 1970]. Later, using the more sophisticated instrumentation of ISEE, Sckopke et al. [1983] found that downstream of high Mach number perpendicular shocks high energy tails are very common. This high energy tail, due to reflected ions, is well modeled by a second, hotter Maxwellian ion peak [Richardson, 1987], especially when the ratio of reflected ions is high (over 50%), which is the case for the dayside magnetosheath of Neptune. The two Maxwellian distributions are constrained to have the same bulk velocities, but the individual number densities and thermal speeds can be varied to produce the best fit to the observed currents. Then the distribution function takes the form

$$f(\mathbf{v}) = f_c(\mathbf{v}) + f_h(\mathbf{v}) = \frac{n_c}{\pi^{3/2}w_c^3} \exp\left\{-\frac{(\mathbf{v} - \mathbf{V})^2}{w_c^2}\right\} + \frac{n_h}{\pi^{3/2}w_h^3} \exp\left\{-\frac{(\mathbf{v} - \mathbf{V})^2}{w_h^2}\right\} \quad (1.9)$$

where the subscripts c and h refer to the cold and hot components, respectively. In this case there are 7 adjustable parameters, the densities of the cold and hot components n_c and n_h , the "thermal speeds" of the same components w_c and w_h , and the three components of the common bulk velocity \mathbf{V} .

Because of the low plasma densities near Neptune, only the proton peak can be fitted in the solar wind and magnetosheath. The heavier elements in the solar wind typically make up less

than 5% of the total number density, therefore, using only the proton observations introduces only a small error. In our analysis of the Neptunian bow shock and magnetopause, the complexity of the problem limits us to the use of the single fluid magnetohydrodynamic (MHD) approximation. Therefore, the electron and proton observations have to be combined into a single fluid description. As mentioned earlier, we take the number densities and bulk velocities of the protons and electrons to be the same. Therefore, since the proton mass is almost 2000 times more than the electron mass, the proton mass density is an acceptable description of the single fluid mass density. Of course, the common bulk velocities are adopted as the single fluid bulk velocity, and the pressures of each component needed to be added together to form the single fluid pressure.

In the magnetosheath, the situation is further complicated by the double Maxwellian distribution function of the protons. Turning to our definitions, given in equations (1.2) - (1.5), and referring to the double Maxwellian distribution function given in equation (1.9) as $f(\mathbf{v}) = f_c(\mathbf{v}) + f_h(\mathbf{v})$, the total proton number density is given by

$$n = \int d\mathbf{v} f(\mathbf{v}) = \int d\mathbf{v} \left[f_c(\mathbf{v}) + f_h(\mathbf{v}) \right] = \int d\mathbf{v} f_c(\mathbf{v}) + \int d\mathbf{v} f_h(\mathbf{v}) = n_c + n_h \quad (1.10)$$

and the unified proton "temperature":

$$P = nkT = m_p \int d\mathbf{v} \left[f_c(\mathbf{v}) + f_h(\mathbf{v}) \right] |\mathbf{v} - \mathbf{V}|^2 = n_c kT_c + n_h kT_h \quad (1.11)$$

therefore

$$kT = \frac{n_c kT_c + n_h kT_h}{n_c + n_h} \quad (1.12)$$

In the analysis of the electron spectra in the Neptunian magnetosheath, a three component Maxwellian often has to be employed to give acceptable fits to the measured currents [Zhang *et al.*, 1991]. The above described method for protons is also used to define a total electron

number density and "temperature".

In the solar wind, where the particle temperatures are very cold (on the order of a half eV for the protons) the high resolution M mode measurements are analyzed for the proton parameters. Electron analysis in the solar wind is not possible because its total energy is below the instrument threshold of 10 eV. In the magnetosheath, however, the electron temperatures are much increased, and in the low energy long integration mode (E1-long) the analysis of the electron data is possible. The similarly heated proton component has a significantly reduced count rate per energy channel as the distribution function widens. Therefore, the lower resolution L modes have to be analyzed. To further improve the signal to noise ratio, several neighboring L modes are averaged together, but never more than 5 spectra to avoid time aliasing problems.

1.2.3 The MAG Experiment

In addition to the PLS plasma data, data from the magnetic field (MAG) experiment on Voyager 2 are used in this study. In this section, we briefly describe the MAG experiment. Details of this instrument and the data processing used are published in *Behannon et al.* [1977].

The MAG experiment on Voyager 2 consists of a low field magnetometer (LFM) system and a high field magnetometer (HFM) system. Each system contains two identical triaxial fluxgate magnetometers which measure the magnetic field along three mutually orthogonal axis simultaneously. This provides direct vector measurements of the magnetic field. The two low field magnetometers are located along a 13 m long boom, one at the extreme end and the other about half way out from the spacecraft. The high field magnetometers are mounted 1 m apart on the frame structure of the spacecraft. This dual magnetometer configuration permits the

separation of the magnetic field induced by the spacecraft from the ambient magnetic field.

The magnetic field measurements cover a wide dynamic range from 0.006 γ to 20 G. The low field magnetometer system has 8 dynamic ranges with a quantized uncertainty of about 0.025%. The high field magnetometer system has 2 ranges with the same relative uncertainty. The magnetic field vector measurements are made every 60 msec, but in our study we use a 48 s averaged data set. Unfortunately, during the Neptune encounter the outer low field magnetometer system did not function properly. This introduced some uncertainty in the determination of the "zero" point of the measurements. The MHD bow shock fits, described in Chapter 2, were used in part to reduce this uncertainty [Lepping *et al.*, 1993]. The magnetic field data shown in this work incorporates the latest zero point calibrations.

1.3 The General Structure of Solar Wind Interaction with Magnetospheres

In this section a short overview of the gross solar wind-planetary magnetosphere interaction is given. The purpose is to give the reader some orientation as in subsequent chapters we are going to discuss in depth the individual features of this interaction. The description here is kept general and non-specific to the Neptunian system. The unique characteristics of the Neptunian system are discussed in their appropriate sections.

The solar wind is the supersonically expanding solar corona. Its primary composition is protons and electrons, but it also contains 3-4% He^{++} or α particles and to a lesser degree (< 1%) heavier and or multiply ionized atoms (i.e. C^+ , N^+ , O^+ , and O^{++}). The solar wind plasma is neutral to a very good approximation, and carries with it "frozen in" the solar magnetic field lines. The magnetic field of the magnetized planets (like Neptune) presents an obstacle to the solar wind flow. From several planetary radii away, the planetary magnetic fields are dipolar to a good approximation. When the supersonic solar wind encounters these planetary systems, and

if the planet's magnetic field is sufficiently strong, then the solar wind is deflected around the planet leaving a magnetic bubble where it could not enter. This bubble is called the planet's magnetosphere. (For a schematic diagram of the regions mentioned in this section see Figure 1.1.) Since the solar wind flow is supersonic, that is no information of the oncoming planetary obstacle can pass upstream, a shock forms upstream from the magnetosphere where the solar wind suddenly drops in speed to subsonic values. This shock, enveloping the whole planet, is called the bow shock. It is very similar in cause and shape to aerodynamic shocks forming in supersonic gases which encounter large blunt objects. One main difference is that the solar wind plasma is collisionless, that is the mean free path of the solar wind particles are much larger than the typical scale lengths of the bow shock. Therefore, the thickness of the shock cannot be related to collisional mean free paths, and the heating of the particles on passage through the shock must be explained in terms of damping of plasma waves rather than collisional processes. The details of the Neptunian subsolar bow shock are discussed in Chapter 2.

After the solar wind crosses the bow shock it becomes more dense, subsonic, and acquires a much higher temperature. The slower speeds allow the plasma to flow around the magnetospheric obstacle draping the solar magnetic field lines with it. This region of shocked solar wind plasma is called the magnetosheath. Gas dynamic calculations originally carried out by *Spreiter et al.* [1966] show that an ideal gas approximation for the magnetosheath plasma gives surprisingly good correlation with observations. In Chapter 3, we apply these calculations to the Neptunian magnetosheath. As the magnetosheath plasma flow reaches the dawn and dusk sides of the planet, it regains most of its original speed, and becomes supersonic again.

The boundary around which the magnetosheath flow is deviated has been termed the magnetopause. This boundary surface is located at the position where the shocked

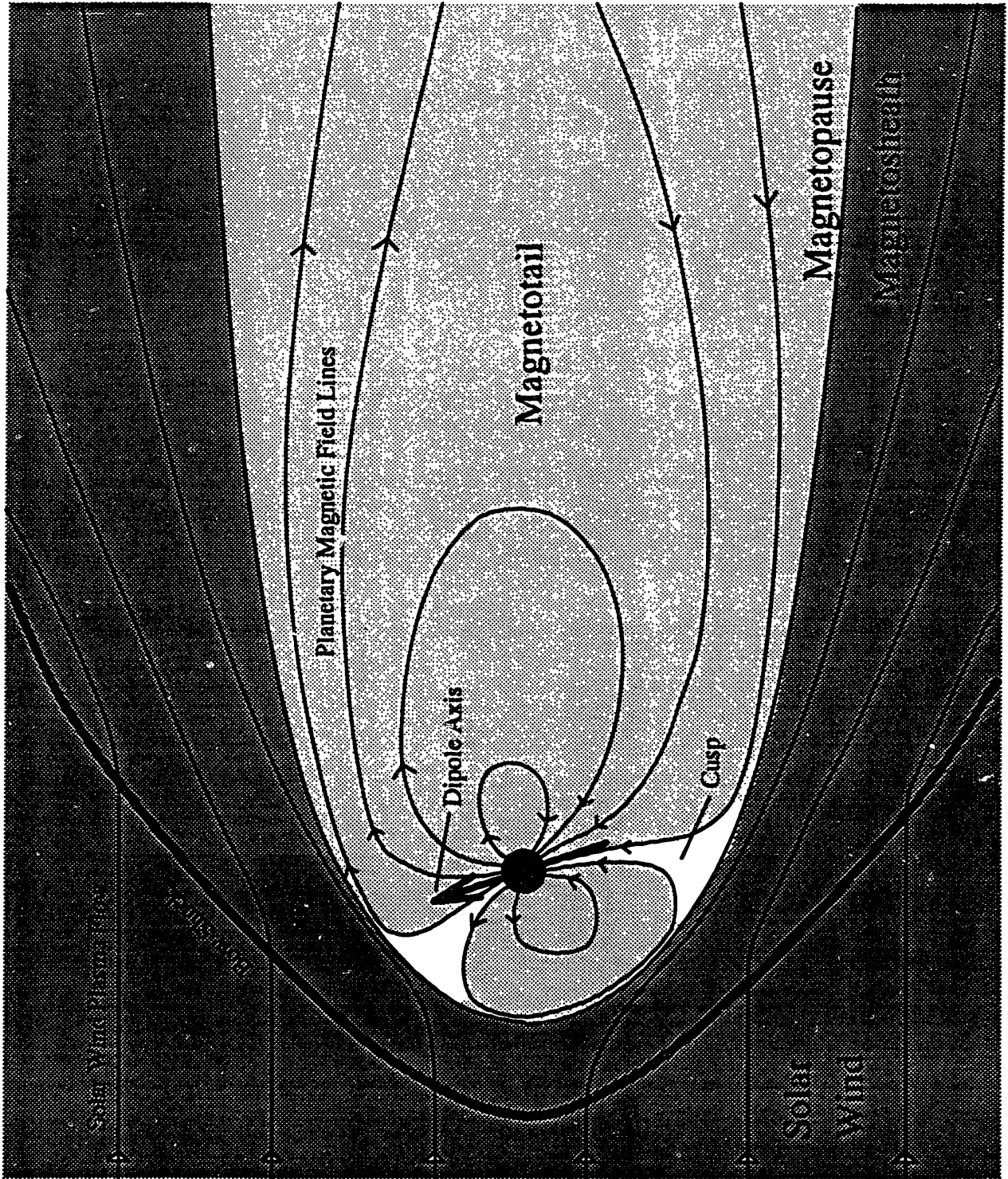


Figure 1.1. Schematic of solar wind - magnetosphere interaction

magnetosheath plasma pressure (ram and thermal) balances the primarily magnetic pressure of the magnetosphere. With regard to the nature of this boundary, considerable attention has been focused on whether it is a rotational discontinuity (i.e. a large amplitude standing Alfvén wave), or a tangential discontinuity (i.e. an equipotential current sheet with unequal particle pressures on either side). If it is a rotational discontinuity, then there can be a component of magnetic field normal to the boundary surface, and plasma can flow through the boundary at a speed equal to the Alfvén speed based on the normal component of the field. If it is a tangential discontinuity, then no such plasma flow through the boundary is possible, and there can be no interconnection of magnetic field lines between the magnetosphere and magnetosheath.

Since only the perpendicular component of the magnetic field can exert pressure on the incoming magnetosheath flow, there is a region both on the northern and southern hemisphere where the planetary field lines are mostly pointing along the plasma flow and unable to keep the shocked solar wind plasma out of the magnetosphere. These polar regions are called the cusps, and are the regions where the shocked solar wind plasma has access into the upper planetary magnetosphere. The entering magnetosheath plasma forms a turbulent boundary layer called the entry layer. Further downstream, this entry plasma acquires a more organized flow pattern tailward and slowly expands the thickness of the boundary layer. At this stage, the boundary layer is referred to as the plasma mantle. Voyager 2 crossed the Neptunian magnetopause at very high magnetic latitudes inbound, and the question of the nature of the magnetopause and the boundary layer behind it is addressed in Chapter 4.

1.3.1 The Voyager 2 Trajectory During the Neptune Encounter

Voyager 2 arrived in the vicinity of Neptune on August 24, 1989. This outermost gas giant planet, is at an average distance of 30.2 AU from the Sun. It completes one cycle of its orbit

(one Neptunian year) in 165 years. Neptune is slightly smaller than Uranus, with an equatorial radius of 24,765 km, but the mass of Neptune is 1.2×10^{26} kg [Tyler *et al.*, 1989], heavier than Uranus, probably because Neptune has a larger rocky core. The core rotates at the period of 16.11 hours, as determined from the PRA radio emission data [Warwick *et al.*, 1989]. The orientation of the rotation axis is quite conventional. It is tilted only 29° from the normal to the orbital plane of Neptune. Neptune also possesses a strong and complicated internal magnetic field. The magnetic field between 4 and $15 R_N$ ($1 R_N$ is one planetary radius) can be well represented by a strongly offset and tilted magnetic dipole (OTD) field. The displacement of the dipole from the planetary center is $0.55 R_N$, and it is tilted by 47° with respect to the rotation axis of Neptune. The dipole moment of this model is $0.133 GR_N^3$ [Ness *et al.*, 1989]. The combination of strongly tilted magnetic dipole and tilted rotation axis creates the unique situation of a subsolar cusp region in every planetary rotation, depicted in Figure 1.2, which is fully investigated in Chapter 4.

Voyager crossed the inbound bow shock at 1438 SCET (Spacecraft Event Time) on August 24, 1989, $34 R_N$ from Neptune. The spacecraft was nearly at the subsolar point from the planet at that time. The Voyager 2 trajectory at Neptune is shown on Figure 1.3 in cylindrical coordinates. Thick lines on the trajectory indicate regions where magnetosheath plasma was observed. The model curves of the bow shock and magnetopause are determined from the inbound and outbound locations of these boundaries as described by Belcher *et al.* [1989].

The inbound magnetopause was crossed at 1800 SCET on August 24, 1989 when the spacecraft was $26 R_N$ from Neptune [Ness *et al.*, 1989; Belcher *et al.*, 1989]. After this time, Voyager continued its flight in the Neptunian magnetosphere and had its closest approach to the planet at 0356 SCET on August 25, 1989. Regions of the Neptunian magnetosphere not accessible to the solar wind plasma are not considered in this study. However, it is worth mentioning that, though relatively empty, the Neptunian magnetosphere does contain plasma

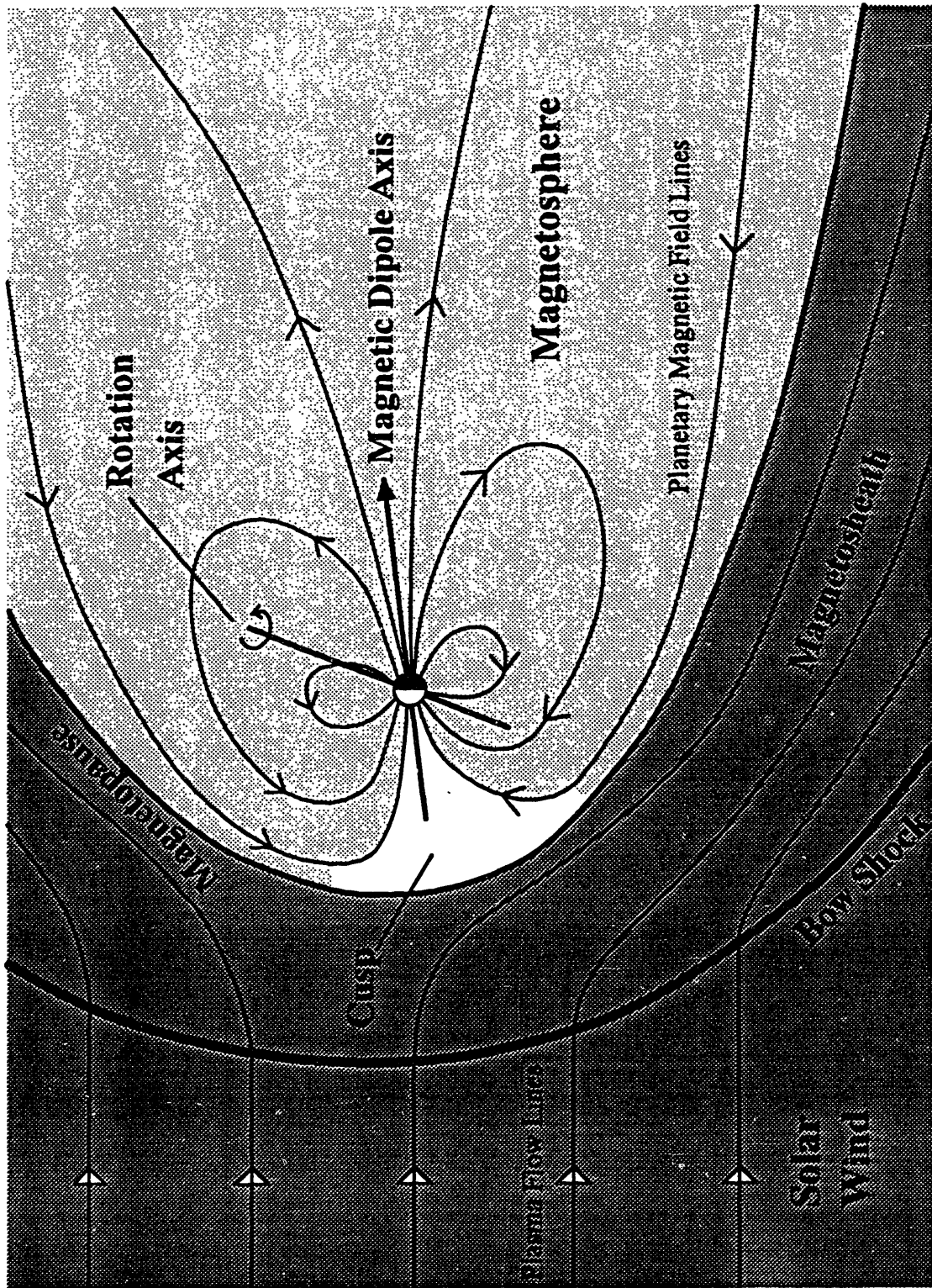


Figure 1.2. Schematic of Neptune's pole-on magnetic configuration.

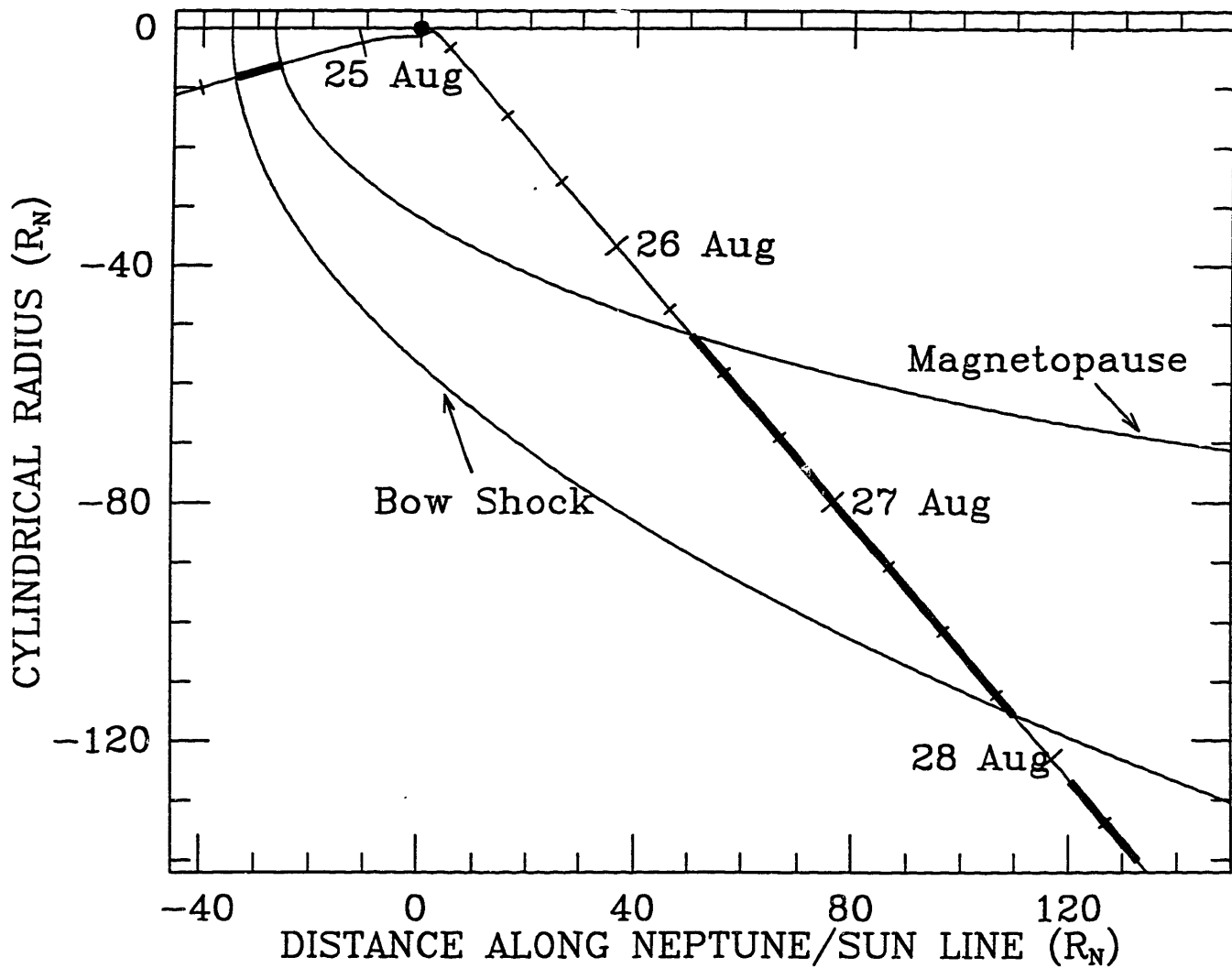


Figure 1.3. Voyager 2 trajectory at Neptune rotated about the Sun-planet line into a meridional plane. The shapes of the bow shock and magnetopause assume axial symmetry about the Sun-planet line. Bold lines indicate where magnetosheath plasma was detected.

from both the surface of the planet and from its largest moon, Triton.

After its closest approach, Voyager 2 turned sharply southward and visited Triton. The spacecraft left the Neptunian magnetosphere at 0819 SCET on August 26, and continued its voyage in the magnetosheath for 36 hours. On the outbound leg, the bow shock was encountered at least four different times before Voyager 2 left the Neptunian system.

CHAPTER 2

THE NEPTUNE INBOUND BOW SHOCK

2.1 Introduction

The first evidence the supersonic solar wind plasma has of the oncoming magnetospheric obstacle is the crossing of the planetary bow shock. In this chapter, we examine the inbound Neptunian bow shock region in detail with the aid of our new MHD fitting technique described in Section 2. Section 3 focuses on the macroscale characteristics of the fitted bow shock, while Section 4 examines the microstructure of this region and compares the scale lengths of the different sub-regions to that observed at other planets and predicted by plasma theory.

Voyager 2 crossed the upstream Neptunian bow shock at 1430 SCET (Spacecraft Event Time) on August 24, 1989 [*Belcher et al.*, 1989; *Ness et al.*, 1989]. The plasma and magnetic field observations of Voyager 2 allow us to study the interaction of the solar wind with the outermost gas giant. The bow shocks of Jupiter and Saturn have been extensively studied and modeled thanks to the ever increasing number of spacecraft flybys [*Spreiter and Stahara*, 1985; *Slavin et al.*, 1985; *Moses et al.*, 1985; and *Stahara et al.*, 1989]. Uranus was visited only by Voyager 2. Preliminary results on the Uranian bow shock are reported by *Bagenal et al.* [1987]. In the case of Neptune, we are also limited to a single spacecraft observation which is not likely to be augmented in the near future. Therefore, we want to fully exploit the Voyager 2 observations in order to understand the Neptunian bow shock.

2.2 The MHD Fitting Technique

Plasma temperatures estimated from data obtained by space probes often have high uncertainties, or are not available at all. As a result, previous shock analysis techniques avoid

the use of equations which include the plasma temperature [e.g. *Lepping and Argentiero, 1971; Viñas and Scudder, 1986*]. Although the Voyager 2 plasma science (PLS) experiment cannot detect the electron distribution in the solar wind near Neptune (since the electron temperature is below the instrument threshold of 10 eV), well resolved ion temperatures are available in the solar wind and magnetosheath; electron temperatures are available in the magnetosheath [see, for example *Bridge et al., 1977; Bagenal et al., 1987; Belcher et al., 1989*]. In order to make full use of this data, we improved the non-linear least squares fitting technique of the non-dissipational magnetohydrodynamic (MHD), "Rankine-Hugoniot" jump conditions originally developed by *Viñas and Scudder [1986]*. We add to their set of conservation equations the conservation of normal momentum flux and energy density flux. Both of these equations require plasma temperature measurements. The first part of this section discusses the improvements in the fitting technique. The second part applies this new method to a set of synthetic shocks of various known physical and geometrical properties to validate it. These synthetic shocks are also used to compare the new method both with the original *Viñas-Scudder* method (hereafter VS method) and the often-used velocity coplanarity technique. And finally, we apply this new method to the Neptune inbound bow shock data set. Both macro and microstructure of the shock are discussed.

2.2.1 The Technique

Several techniques have been developed to determine the characteristics of MHD shocks. The widely used magnetic coplanarity [*Lepping and Argentiero, 1971*], velocity coplanarity [*Abraham-Shrauner, 1972*], and the mixed data method of Abraham-Shrauner [*Abraham-Shrauner and Yun, 1976*] all depend on a single averaged data point, one on each side of the shock. Reducing the measured data set on each side of the shock to a single averaged point,

before the actual analysis is performed, makes these procedures prone to errors introduced by waves and noise in the spacecraft data. Considering all the measured data in an iterative manner, as we do in our technique, eliminates this source of errors. Also, these techniques use only a small subset of the MHD conservation equations across the shock, often resulting in disparate solutions for the same set of measurements. Iterative schemes, such as the *Lepping and Argentiero* [1971] method, try to resolve this problem by solving directly a slightly expanded subset of these equations for the asymptotic magnetofluid variables. Asymptotic magnetofluid variables are the plasma and magnetic field parameters predicted by the chosen physical theory in the absence of any source of noise and error. These variables are subsequently used together with the magnetic coplanarity and mass flux conservation equations to determine the shock normal direction and the bulk speed of the shock. While this method is certainly self-consistent, it requires finding the solution in an 11 dimensional parameter space, which raises the question of the uniqueness of the solution. This method is also expensive in computer time and has difficulty determining the solution for perpendicular shocks. More recently, *Viñas and Scudder* [1986] describe an iterative method which is not only self-consistent and fast, but also addresses the question of the uniqueness of the solution. They replace the 11 dimensional space of unknown magnetofluid variables of the plasma densities and magnetic field strength vectors on both sides of the shock along with the plasma bulk speed difference ($\rho_1, \rho_2, V_2 - V_1, B_1$ and B_2) with a new set of 11 "natural" variables ($\phi, \theta, V_S, G_n, B_n, S_t, E_t, \rho_1$ and ρ_2), where ϕ and θ are angles that define the unit shock normal, \hat{n} . Specifically, θ is the angle measured from a designated axis (usually the Sun-planet line) and ϕ is the azimuth angle such that the unit shock normal is given by the relations $\hat{n}_x = \cos \theta$, $\hat{n}_y = \cos \phi \sin \theta$, and $\hat{n}_z = \sin \phi \sin \theta$. The other variables are defined so that V_S is the shock speed along the normal, G_n the conserved mass flux, B_n the normal component of the magnetic field, S_t the tangential component of the momentum flux, E_t the tangential

component of the electric field, and ρ_1 and ρ_2 the upstream and downstream plasma mass densities. The the "Rankine-Hugoniot problem" then becomes separable, that is, the solution process is reducible to a sequence of one and two dimensional subspace procedures where uniqueness can be established analytically (for one dimension) or graphically (for two dimensions).

The MHD conservation equations in the spacecraft reference frame are:

$$\Delta[G_n] = \Delta[\rho(V_n - V_S)] = 0 \quad (2.1)$$

$$\Delta[B_n] = \Delta[\mathbf{B} \cdot \mathbf{n}] = 0 \quad (2.2)$$

$$\Delta[S_t] = \Delta \left[\rho(V_n - V_S)V_t - \frac{B_n}{\mu_0} B_t \right] = 0 \quad (2.3)$$

$$\Delta[E_t] = \Delta[(\mathbf{n} \times \mathbf{V})B_n - (V_n - V_S)(\mathbf{n} \times \mathbf{B})] = 0 \quad (2.4)$$

$$\Delta[S_n] = \Delta \left[P + \frac{B_t^2}{2\mu_0} + \rho(V_n - V_S)^2 \right] = 0 \quad (2.5)$$

$$\Delta[\epsilon] = \Delta \left[\rho(V_n - V_S) \frac{(\mathbf{V} - V_S \mathbf{n})^2}{2} + \rho(V_n - V_S) \left(\frac{\gamma}{\gamma - 1} \frac{P}{\rho} + \frac{B^2}{\mu_0 \rho} \right) - \frac{B_n(\mathbf{V} - V_S \mathbf{n}) \cdot \mathbf{B}}{\mu_0} \right] = 0 \quad (2.6)$$

where ρ is the mass density and \mathbf{V} and \mathbf{B} are the plasma bulk velocity and the magnetic field, respectively, as measured by the spacecraft. The subscripts n and t refer to the normal and tangential components of the above quantities. The total scalar isotropic thermal pressure $P = nkT$, \mathbf{n} is the shock unit normal, and γ is the ratio of the specific heats. The variables G_n , B_n , S_t , E_t , S_n and ϵ represent the conservation constants corresponding to the mass flux, normal magnetic field, tangential momentum flux (stress), tangential electric field, normal

momentum flux, and energy flux, respectively. The notation $\Delta[]$ refers to the difference across the shock. Note that since equations (2.3) and (2.4) are vector equations, equations (2.1) through (2.6) represent 10 independent equations.

While the Viñas and Scudder (VS) method is fast and optimal, it uses only the first four conservation equations. Therefore, we will also refer to the VS method as the incomplete R-H method. We extend the VS method to include the last two conservation equations in order to be able to use the temperature measurements available from the Voyager mission [Szabo, 1993]. We will refer to this extension as the Szabo method, or equivalently, the complete R-H method. The sequence of shock parameter determination follows the original VS method. The set of "natural" variables is extended to include S_n and ϵ , the normal component of the momentum flux and the energy density flux, respectively. We still make the assumption that non-dissipational, single fluid MHD jump conditions provide an adequate approximation of space plasma shocks. Also, we limit the scope of our analysis to plasma described by isotropic, scalar pressure. Furthermore, we assume that a meaningful set of plasma parameters (density, bulk velocity and temperature) can be obtained in the regions of interest because either the plasma is completely thermalized and a Maxwellian distribution function can be fitted to the measured spectra, or some other appropriate approximation can be made. Once these assumptions are met, first the shock normal is found, followed by the shock speed, the conservation constants, and finally the self-consistent Rankine-Hugoniot (RH) asymptotic states. A detailed description of the method follows:

(I) Equation (2.1) is used to obtain an expression of the shock bulk speed which can be substituted in the other jump condition equations, removing this unknown quantity from the system, to wit:

$$V_s = \frac{\Delta[\rho V]}{\Delta[\rho]} \cdot \mathbf{n} \quad (2.7)$$

At this point, we assume that the value of γ , the ratio of specific heats, is known on both sides of the shock, and assign preliminary, best guess values to it. The determination of the proper values of γ will be discussed later. This gives us a system of nine equations (equations (2.2)-(2.6) where (2.3) and (2.4) are vector equations) in terms of the plasma mass density ρ , velocity \mathbf{V} , magnetic field \mathbf{B} , total particle temperature T and the shock normal \mathbf{n} , which is expressed in spherical coordinates (θ, ϕ) . The plasma density, velocity, temperature and magnetic field are observed on both sides of the shock, leaving θ and ϕ , the parameters of the unit shock normal, as the only two unknowns in the system. This system of equations can be solved by the iterative non-linear least squares fit technique of the Levenberg-Marquardt method [Press *et al.*, 1986]. If we represent the individual equations of our system of MHD jump conditions by $Y_j(\mathbf{x}; \mathbf{p}) = 0$, where $\mathbf{x} = (\rho_1, \mathbf{V}_1, \mathbf{B}_1, T_1, \rho_2, \mathbf{V}_2, \mathbf{B}_2, T_2)$ are the observed quantities and $\mathbf{p} = (\theta, \phi)$ are the unknown parameters, then we can express $\chi^2(\theta, \phi)$, the norm of the residuals which is minimized by the best fit solution, as

$$\chi^2(\theta, \phi) = \sum_{i=1}^N \sum_{j=1}^K \frac{\left[Y_j(\mathbf{x}_i; \mathbf{p}) - y_j \right]^2}{\sigma_{ij}^2} \quad (2.8)$$

where N are the number of data pairs \mathbf{x} across the shock, K is the number of equations in the system, namely 9, and y_j is the theoretically expected value of the model equation Y_j , which in our case is zero. Finally, σ_{ij} is the standard deviation in the j -th model equation when the i -th observed data pair is used to calculate the value of the model equation. The standard deviations are propagated from the individual standard errors in the observed quantities. Through the division by σ_{ij}^2 , we have made χ^2 dimensionless and independent of the units used in the particular conservation equations. In fact, the standard deviations behave as a weighting factor

of the individual measured data pairs. The higher the uncertainty in the measured data point, the less weight it is given in the fitting procedure.

Two different methods are used to construct the observed data pairs \mathbf{x} . In one method, each data point on one side of the shock is paired with one data point on the other side, symmetrically moving away from the shock. In the other method, all data points on one side are paired with all data points on the other side. The second method, although it provides many more data pairs, and therefore better statistics, is not based on more physical measurements. It is, however, very well suited for noisy data sets where fluctuations are not a function of distance from the shock. On the other hand, when a systematic change in plasma conditions with distance from the shock is observed, the first method is better able to determine the true MHD regions of the shock.

When the χ^2 function reaches a minimum, we have a best fit for the parameters θ and ϕ . If we map out the χ^2 function over the locus of all possible solutions (a hemisphere $0 \leq \theta \leq \pi/2$, $0 \leq \phi \leq 2\pi$), we can find all local minima of the function and therefore investigate all likely solutions, removing the question of uniqueness. Each possible solution has to be investigated separately to see if it represents a valid shock [i.e. there is plasma flow across the surface, the normal plasma flow is supersonic on one side and subsonic on the other, there is a density jump in the same sense as the temperature change (entropy increases), and the plasma flow is toward the density increase] and to see that the calculated asymptotic magnetofluid parameters are in good agreement with the observations.

We apply the new analysis to an oblique synthetic shock as a demonstration of each step of the procedure. Synthetic shocks are artificially created shock data sets with prescribed physical and geometrical properties. A complete description of the generation of synthetic shock data will be presented later in this chapter in Section 2.2. The input parameters and solutions to the synthetic oblique shock from various techniques are shown in Table 2.1. Figure 2.1 shows

Results of Different Techniques on a Synthetic Oblique Shock

	Exact Solution	Complete R-H Method (Szabo)		Incomplete R-H Method (VS)		Velocity Coplanarity
		One to One	All Pairs	One to One	All Pairs	
$\theta_{B_{00}}$ deg	40.2	40.7 ± 4.8	40.7 ± 2.0	40.6 ± 4.8	40.6 ± 2.1	43.9
V_S , km/s	-60.0	-55.9 ± 18.8	-56.1 ± 18.8	-55.8 ± 18.8	-55.8 ± 18.8	-50.3
n_x	0.816	0.820 ± 0.014	0.819 ± 0.004	0.820 ± 0.014	0.820 ± 0.004	0.840
n_y	-0.408	-0.401 ± 0.024	-0.400 ± 0.007	-0.400 ± 0.025	-0.399 ± 0.007	-0.371
n_z	0.408	0.409 ± 0.024	0.410 ± 0.007	0.408 ± 0.024	0.410 ± 0.007	0.396
n_1 , $10^{-5}/\text{cm}^3$	500.	495. ± 2.1	496. ± 1.1	492. ± 5.8	492. ± 5.6	498.*
V_{x1} , km/s	400.0	400.8 ± 11.0	400.0 ± 10.3	402.5 ± 11.5	402.4 ± 10.9	404.3*
V_{y1} , km/s	20.0	22.9 ± 6.5	23.4 ± 5.6	22.2 ± 6.7	22.5 ± 5.8	23.0*
V_{z1} , km/s	20.0	19.3 ± 6.9	19.3 ± 4.3	20.0 ± 7.1	20.4 ± 6.1	19.6*
B_{x1} , nT	0.05	0.048 ± 0.006	0.048 ± 0.005	0.049 ± 0.006	0.049 ± 0.005	0.047*
B_{y1} , nT	-0.15	-0.146 ± 0.009	-0.146 ± 0.004	-0.145 ± 0.009	-0.145 ± 0.004	-0.151*
B_{z1} , nT	0.10	0.098 ± 0.012	0.098 ± 0.004	0.098 ± 0.012	0.098 ± 0.004	0.103*
$kT_{\text{tot}1}$, eV	2.6	6.3 ± 5.2	13.1 ± 5.7			2.6*
n_2 , $10^{-5}/\text{cm}^3$	1500.	1520. ± 26.	1522. ± 25.	1525. ± 27.	1525. ± 26.	1523.5*
V_{x2} , km/s	184.7	184.1 ± 10.0	184.0 ± 10.0	183.7 ± 10.0	183.8 ± 10.0	184.3*
V_{y2} , km/s	118.5	119.6 ± 6.1	119.7 ± 5.5	119.8 ± 6.1	119.7 ± 5.4	120.3*
V_{z2} , km/s	-82.2	-83.1 ± 6.3	-83.3 ± 5.7	-83.3 ± 6.3	-83.4 ± 5.7	-84.0*
B_{x2} , nT	-0.09	-0.091 ± 0.017	-0.092 ± 0.012	-0.092 ± 0.017	-0.092 ± 0.012	-0.094*
B_{y2} , nT	-0.34	-0.341 ± 0.026	-0.341 ± 0.017	-0.342 ± 0.026	-0.342 ± 0.018	-0.341*
B_{z2} , nT	0.19	0.188 ± 0.034	0.188 ± 0.018	0.189 ± 0.034	0.188 ± 0.018	0.187*
$kT_{\text{tot}2}$, eV	327.1	319.8 ± 22.2	319.6 ± 21.9			332.8*
γ_z	2.08	1.88 ± 0.16	1.81 ± 0.14			

* The preaveraged values of the magnetofluid parameters.

Table 2.1. Comparison of the results yielded by different techniques for a synthetic oblique shock. Exact solution refers to the values used to generate the model shock. The two data pairing modes are explained in the text.

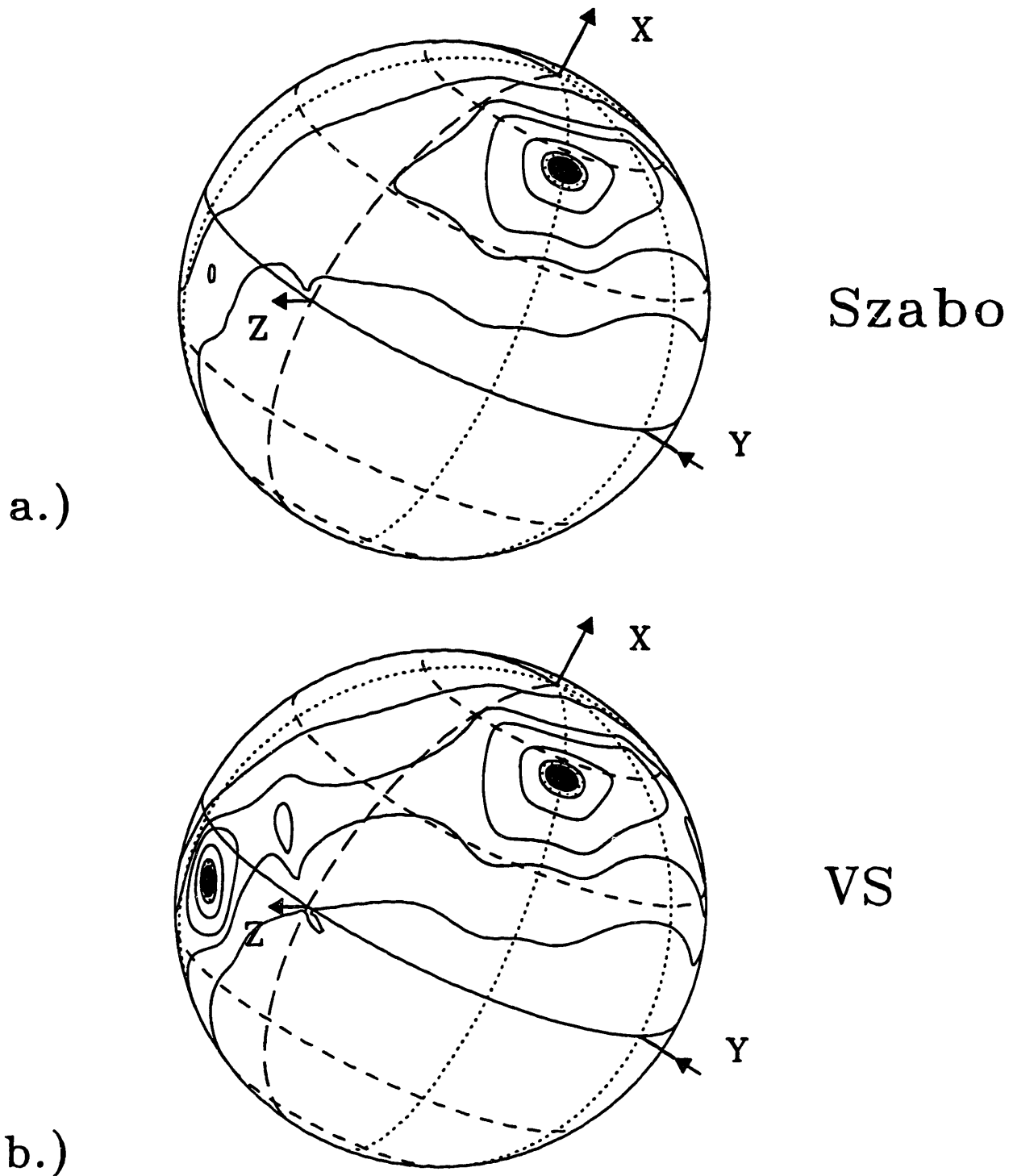


Fig. 2.1. Confidence regions of the fitted shock normal for a synthetic oblique shock shown on unit spheres which are the locus of all possible solutions. The same data is analyzed by our technique (a) and the VS method (b). Note that our technique eliminates the spurious solution obtained by the VS method.

graphical solutions for this shock. The upper panel (a) shows the χ^2 map for the new technique on the unit sphere, whereas the lower panel (b) shows the same synthetic data fitted by the VS method. The black shaded area is the 99% confidence region and the dotted area represents the 99.99% confidence level. Higher contour levels are added to show the general outline of the map. Our method gives one outstanding peak, while the VS method yields two distinct solutions with the same confidence levels. Clearly, one of the VS peaks is spurious; our method is able to eliminate the spurious solution.

(II) Once the best shock normal \mathbf{n} is established, Equation (2.7) is used with the observed data to calculate the bulk shock speed V_S . We could employ a one dimensional version of the above described non-linear least squares technique to establish the best fit value of V_S ; however, since V_S is linear in the model equation, a unique analytical solution is possible. The χ^2 function to be minimized can be written as:

$$\chi^2(V_S) = \sum_{i=1}^N \frac{\left[\frac{\Delta[\rho_i \mathbf{V}_i] \cdot \mathbf{n}}{\Delta[\rho_i]} - V_S \right]^2}{\sigma_i^2} \quad (2.9)$$

This differs again from the VS technique in that, rather than assigning an average standard deviation σ for all the data pairs, the standard deviations are calculated individually for each data pair and are used as a weighting function in our procedure. Setting the first derivative of χ^2 with respect to V_S equal to zero and checking the second derivatives provides the analytical solution for V_S :

$$V_S = \frac{\sum_{i=1}^N \frac{\Delta[\rho_i \mathbf{V}_i] \cdot \mathbf{n}}{\sigma_i^2 \Delta[\rho_i]}}{\sum_{i=1}^N \frac{1}{\sigma_i^2}} \quad (2.10)$$

This equation differs from its VS equivalent in that the individual σ_i 's cannot be pulled through the summation signs. This solution is unique because the second derivative of the χ^2 function can be shown to be positive everywhere.

(III) Once the shock normal and speed are determined, we proceed to find the RH conservation constants. The conservation constants, by definition, are calculated from locally measured plasma and magnetic field data on one or the other side of the shock, and not from differences of these parameters taken across the shock. That is, for example, the conserved mass flux density $G_n = \rho(V_n - V_S)$ should compute to the same value regardless which side of the shock we take the plasma density and normal bulk speed data from, and it is not dependent on any difference taken across the shock. The other conserved quantities have the same characteristic and are defined in equations (2.1) - (2.6). Inspection of these equations also reveal that they are all linear and independent. Therefore, the same analytical method can be used to obtain the solutions as was demonstrated for the case of the shock speed. Since the conserved quantities can be independently calculated at each data point, the summation in our solution runs over all of the available data points, numbering M , and not over the N number of data pairs across the shock constructed in various ways in the previous equations. Again, we differ from the VS technique by using individually propagated standard deviations, rather than an averaged error method, yielding the following unique solutions for the conservation constants:

$$G_n = \sum_{i=1}^M \frac{\rho_i (V_{n_i} - V_S)}{\sigma_i^2} / \sum_{i=1}^M \frac{1}{\sigma_i^2} \quad (2.11)$$

$$\mathbf{B}_n = \sum_{i=1}^M \frac{\mathbf{B}_{n_i}}{\sigma_i^2} / \sum_{i=1}^M \frac{1}{\sigma_i^2} \quad (2.12)$$

$$\mathbf{S}_t = \sum_{i=1}^M \frac{\rho_i (\mathbf{V}_{n_i} - \mathbf{V}_S) \mathbf{V}_t - \mathbf{B}_{n_i} \mathbf{B}_t / \mu_0}{\sigma_i^2} / \sum_{i=1}^M \frac{1}{\sigma_i^2} \quad (2.13)$$

$$\mathbf{E}_t = \sum_{i=1}^M \frac{(\mathbf{n} \times \mathbf{V}_i) \mathbf{B}_{n_i} - (\mathbf{V}_{n_i} - \mathbf{V}_S)(\mathbf{n} \times \mathbf{B}_i)}{\sigma_i^2} / \sum_{i=1}^M \frac{1}{\sigma_i^2} \quad (2.14)$$

$$\mathbf{S}_n = \sum_{i=1}^M \frac{\frac{\rho_i}{2} \left[\frac{m_e}{m_i} w_{e_i}^2 + w_{i_i}^2 \right] + \frac{B_i^2 - B_{n_i}^2}{2\mu_0} + \rho_i (\mathbf{V}_{n_i} - \mathbf{V}_S)^2}{\sigma_i^2} / \sum_{i=1}^M \frac{1}{\sigma_i^2} \quad (2.15)$$

$$\begin{aligned} \varepsilon = \sum_{i=1}^M \left[\rho_i (\mathbf{V}_{n_i} - \mathbf{V}_S) \left[\frac{V_t^2 + (\mathbf{V}_{n_i} - \mathbf{V}_S)^2}{2} + \frac{1}{2} \frac{\gamma}{\gamma - 1} \left(\frac{m_e}{m_i} w_{e_i}^2 + w_{i_i}^2 \right) + \frac{B_i^2}{\mu_0 \rho_i} \right] - \right. \\ \left. - \frac{1}{\mu_0} \left[\mathbf{B}_{n_i} (\mathbf{V}_i \cdot \mathbf{B}_i) - B_{n_i}^2 \mathbf{V}_S \right] \right] / \sigma_i^2 / \sum_{i=1}^M \frac{1}{\sigma_i^2} \quad (2.16) \end{aligned}$$

where w_e and w_i are the electron and ion thermal speeds (which are observed quantities) and m_e/m_i is the ratio of the electron to positive ion mass, which is typically assumed equal to the proton mass introducing a small error due to the ignored α -particle component. The electron and positive ion thermal pressures and energies are added together as required by the single fluid description. From now on, we assume that all the positive ions are protons to keep the equations relatively simple. However, should the need arise to include heavier elements, the modification is trivial. Equations (2.11) - (2.16) assume charge neutrality, meaning that the proton and electron number densities are the same.

(IV) Finally, the self-consistent RH asymptotic states can be determined. After some

algebraic manipulation of equations (2.1) - (2.6) the magnetofluid variables can be expressed as

$$\mathbf{V}(\rho) = \frac{G_n \mathbf{S}_t + \rho \frac{B_n}{\mu_0} (\mathbf{n} \times \mathbf{E}_t)}{G_n^2 - \rho B_n^2 / \mu_0} + \mathbf{n} (G_n / \rho + V_S) \quad (2.17)$$

$$\mathbf{B}(\rho) = \frac{\rho \left[B_n \mathbf{S}_t + G_n (\mathbf{n} \times \mathbf{E}_t) \right]}{G_n^2 - \rho B_n^2 / \mu_0} + \mathbf{n} B_n \quad (2.18)$$

$$P(\rho) = S_n - \frac{B(\rho)^2 - B_n^2}{2\mu_0} - G_n^2 / \rho \quad (2.19)$$

$$\frac{\gamma}{\gamma-1} P(\rho) = \frac{\epsilon \rho}{G_n} - \frac{V(\rho)^2 \rho}{2} - \frac{B(\rho)^2}{\mu_0} + G_n V_S + V_S^2 \rho + \rho \frac{B_n G_n}{\mu_0} \left[\mathbf{V}(\rho) \cdot \mathbf{B}(\rho) - B_n V_S \right] \quad (2.20)$$

where each equation is employed on both sides of the shock independently yielding the upstream and downstream asymptotic magnetofluid variables. A short inspection of these equations reveals that the plasma velocity, pressure, magnetic field and γ are all expressed as functions of only the conservation constants and the plasma mass density. (Of course, $\mathbf{V}(\rho)$ and $\mathbf{B}(\rho)$ have to be determined first, then P and γ will be functions of the density only.) That is, if we can solve for the mass density on both sides of the shock, we immediately gain the rest of the magnetofluid variables.

To find the asymptotic values of the plasma mass densities upstream and downstream of the shock, we again apply the non-linear least squares technique described above. Our model functions are the differences between the measurements and the theoretical predictions of equations (2.17) - (2.20). We add a 9-th equation to our system of the form:

$$Y_9(\mathbf{x}_i; \mathbf{p}) = \rho_i - \rho = 0 \quad (2.21)$$

where Y_9 is the 9-th model equation as defined in step (I), ρ_i refers to the individual measurements of the plasma density, and ρ stands for the asymptotic fit value. Again, in our

case, all nine model equations should evaluate to zero; i.e. $Y_j(\mathbf{x}_i; \mathbf{p}) = 0$. The input variables are $\mathbf{x}_i = (\rho, \mathbf{V}, \mathbf{B}, P, \gamma)_i$ measured on either the upstream or downstream side of the shock (the values of γ are still the previously assumed ones). This time, we only have one fit parameter, namely the plasma mass density ρ which we still denote, for the sake of generality, by the vector notation \mathbf{p} . The best fit is determined by evaluating the $\chi^2(\rho)$ function summed over all the model equations and data points on one side of the shock at a time and is weighted by the individually propagated standard deviations as it was done in equation (2.8). The minima of the $\chi^2(\rho)$ function represent the solutions of the fit. Uniqueness of the solution can be ascertained by plotting χ^2 as a function of ρ and individually inspecting all local minima. Such a plot is presented in Figure 2.2 for the same synthetic oblique shock for which the shock normal was found in Figure 2.1. The upper panel shows the χ^2 map for both the upstream (solid line) and the downstream (dashed line) data. The horizontal axis is the normalized number density ($\hat{n} = n/n^*$) where the normalization constant is the best fit value of the number density (n^*) used in order to be able to compare the goodness of fit for both sides of the shock. The lower panel shows the same quantities as obtained by the VS method. A slight improvement over the VS results is evident in the reduction of the size of the confidence regions (the valleys on the graph are narrower).

One should note that equations (2.17) - (2.20) have singularities for ρ equal to 0 and $\mu_0 G_n^2/B_n^2$. The first value is non-physical (it refers to no plasma present), while the second singularity corresponds to a rotational discontinuity. These values of ρ are discriminated against in the fitting procedure and show up as maxima in the χ^2 map. To deal with rotational discontinuities properly, further improvements of the technique are required, as discussed in Chapter 4.

Once the asymptotic value of the mass density is known, equations (2.17) - (2.20) are used to find the rest of the asymptotic magnetofluid parameters on each side of the shock, including

Synthetic Oblique Shock

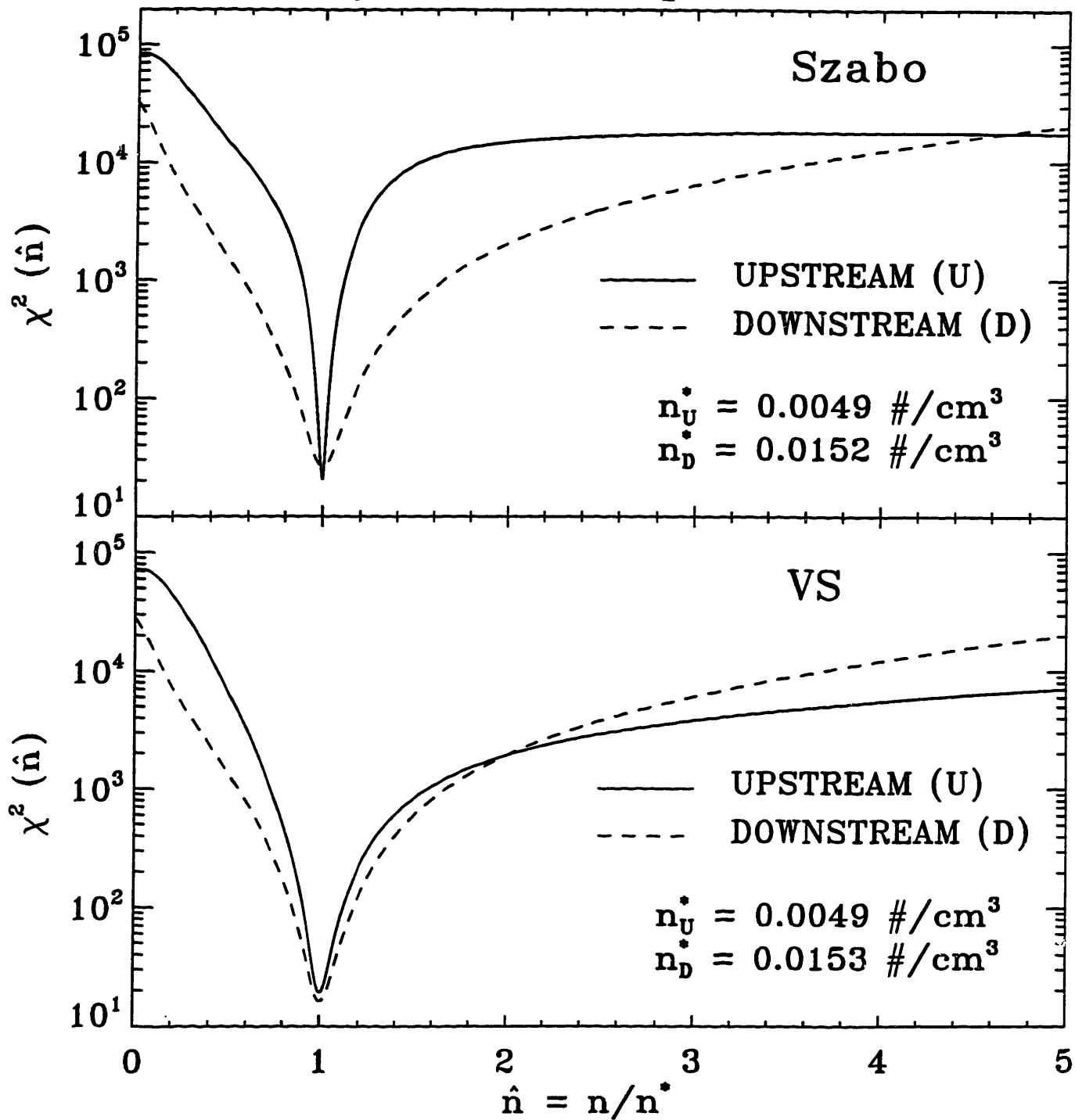


Fig. 2.2. χ^2 map of the plasma number density determined both upstream and downstream from a synthetic oblique shock. The horizontal axis shows the trial number densities normalized by the best fit values (n^*). The upper panel shows our results, whereas the lower panel presents the solutions of the VS method.

the better approximations to the values of the ratio of the specific heats, γ . The plasma density, velocity, temperature and magnetic field strength are measured quantities, and discrepancies from our fit results are due to either noise in the data or an indication of the limits of the physical theory. We do not measure γ , and started with an educated guess of its value based on years of observations at different planets. Once the asymptotic values of γ , which are better approximations to the true value of γ , are obtained on both sides of the shock, it can be substituted as our new initial guess improving our fit procedure. We find that looping over our procedures three or four times completely stabilizes the values of γ , within the measurement uncertainties.

In addition to obtaining asymptotic values of the total particle temperatures and eliminating spurious solutions produced by the VS method, the determination of the ratio of specific heats on both sides of a shock is a feature of our technique not available using the VS method.

2.2.2. Analysis of Synthetic Shocks

To test the range of validity of our shock fitting technique, a program was developed to simulate pure, non-dissipational MHD shocks once the upstream magnetofluid parameters (plasma density, velocity, total particle thermal energy, magnetic field strength and the ratio of specific heats), the shock bulk parameters (shock normal direction and shock speed), and the strength of the shock (ρ_2/ρ_1) are supplied. The program generates an upstream and downstream data set with random noise and error bars characteristic of the Voyager 2 measurements near the outer planets. These synthetic data sets are given to the shock analysis program and the resulting fit values are compared with the exact solutions used to generate the data. This procedure was demonstrated with an oblique shock in Table 2.1, Figure 2.1, and Figure 2.2. To illustrate the wide range of applicability and success of the technique, Table 2.2

compares the fit results with the exact solutions for a nearly perpendicular, a nearly parallel and an oblique high compression shock, characteristic of planetary bow shocks.

One immediately notes that the exact solutions are nearly always inside the small one standard deviation intervals of the fits. Some deviation from the input parameters occurs, mainly because up to a 15% random noise level was superimposed on the model data sets which can slightly alter the MHD solutions. The model data sets are shown in Figure 2.3 for the quasi-perpendicular shock, in Figure 2.4 for the quasi-parallel shock, and in Figure 2.5 for the oblique shock. The quasi-parallel shock solution shows large uncertainties in the fit values indicating its high sensitivity to parameter fluctuations. Also, the technique encounters some difficulty finding the synthetic solar wind particle thermal energies in the upstream regions. This effect is due to the extremely cold environment with ram kinetic energy orders of magnitude above the thermal energy, and the magnetic field energy at least 10 times higher. Therefore, even small errors in the plasma velocity, density and magnetic field can completely wipe out information about the thermal conditions or the value of γ . The fitting technique fares much better in the shocked downstream regions, where the particle thermal energies are much higher. The fit results are graphically illustrated in Figure 2.3-2.5 for all three synthetic shocks. The solid dots with error bars represent the simulated measurements, while the solid straight lines represent the fit values with one standard deviation intervals indicated by dotted lines. The technique of standard error determination is explained in detail in the next section. The close agreement between the simulation and the fit values is apparent.

As mentioned earlier, the synthetic oblique shock is used to compare the results obtained using different fitting procedures. Specifically, we compared our technique to the original VS method and the preaveraged method of velocity coplanarity (see Table 2.1). For those parameters determined by both our technique and the VS method, they give comparably good results. The statistics of both methods improve if we form all the possible data pairs rather than

Results of the Analysis of Synthetic Shocks Using the Szabo Method

	Quasi-Perp. Shock		Quasi-Parallel Shock		Oblique Shock	
	Exact Solution	Results	Exact Solution	Results	Exact Solution	Results
θ_{B0} , deg	93.6	92.7 ± 3.1	5.8	4.6 ± 29.9	40.2	40.7 ± 4.8
V_S , km/s	30.0	44.5 ± 16.5	10.0	17.2 ± 11.6	-60.0	-55.9 ± 18.8
n_x	0.943	0.943 ± 0.009	0.577	0.594 ± 0.035	0.816	0.820 ± 0.014
n_y	0.236	0.227 ± 0.029	-0.577	0.566 ± 0.039	-0.408	-0.401 ± 0.024
n_z	0.236	0.244 ± 0.029	-0.577	0.572 ± 0.038	0.408	0.409 ± 0.024
n_1 , $10^{-5}/\text{cm}^3$	500.	$469. \pm 1.2$	500.	$508. \pm 3.4$	500.	$495. \pm 2.1$
V_{x1} , km/s	400.0	405.7 ± 10.3	400.0	395.7 ± 5.0	400.0	400.8 ± 11.0
V_{y1} , km/s	20.0	21.0 ± 6.2	20.0	22.9 ± 7.5	20.0	22.9 ± 6.5
V_{z1} , km/s	20.0	23.8 ± 6.7	20.0	22.9 ± 7.4	20.0	19.3 ± 6.9
B_{x1} , nT	0.05	$0.048 \pm 7.9 \times 10^{-3}$	0.10	0.101 ± 0.013	0.05	0.048 ± 0.006
B_{y1} , nT	-0.15	$-0.136 \pm 6.6 \times 10^{-3}$	-0.10	-0.100 ± 0.017	-0.15	-0.146 ± 0.009
B_{z1} , nT	-0.10	$-0.092 \pm 11.6 \times 10^{-3}$	-0.08	-0.085 ± 0.014	0.10	0.098 ± 0.012
$kT_{\text{tot}1}$, eV	2.6	1.1 ± 1.2	2.6	1.5 ± 1.4	2.6	6.3 ± 5.2
n_2 , $10^{-5}/\text{cm}^3$	1500.	$1522. \pm 22.$	1500.	$1514. \pm 40.$	1500.	$1520. \pm 26.$
V_{x2} , km/s	175.6	178.1 ± 10.2	325.1	321.1 ± 6.4	184.7	184.1 ± 10.0
V_{y2} , km/s	-35.1	-33.1 ± 6.8	94.9	93.3 ± 9.5	118.5	119.6 ± 6.1
V_{z2} , km/s	-35.5	-34.5 ± 7.0	98.7	97.5 ± 9.4	-82.2	-83.1 ± 6.3
B_{x2} , nT	0.17	0.173 ± 0.009	0.12	0.111 ± 0.050	-0.09	-0.091 ± 0.017
B_{y2} , nT	-0.44	-0.437 ± 0.023	-0.12	-0.117 ± 0.052	-0.34	-0.341 ± 0.026
B_{z2} , nT	-0.29	-0.295 ± 0.035	-0.05	-0.061 ± 0.043	0.19	0.188 ± 0.034
$kT_{\text{tot}2}$, eV	249.5	233.2 ± 17.6	91.2	87.4 ± 6.8	327.1	319.8 ± 22.2
γ_2	2.06	1.90 ± 0.17	1.85	1.99 ± 0.36	2.08	1.88 ± 0.16

Table 2.2. Results of the analysis of various synthetic shocks. The fit results are compared to the exact values used to generate the synthetic shocks. The model shocks incorporate a large, up to 15%, random noise.

Synthetic Quasi-Perpendicular Shock

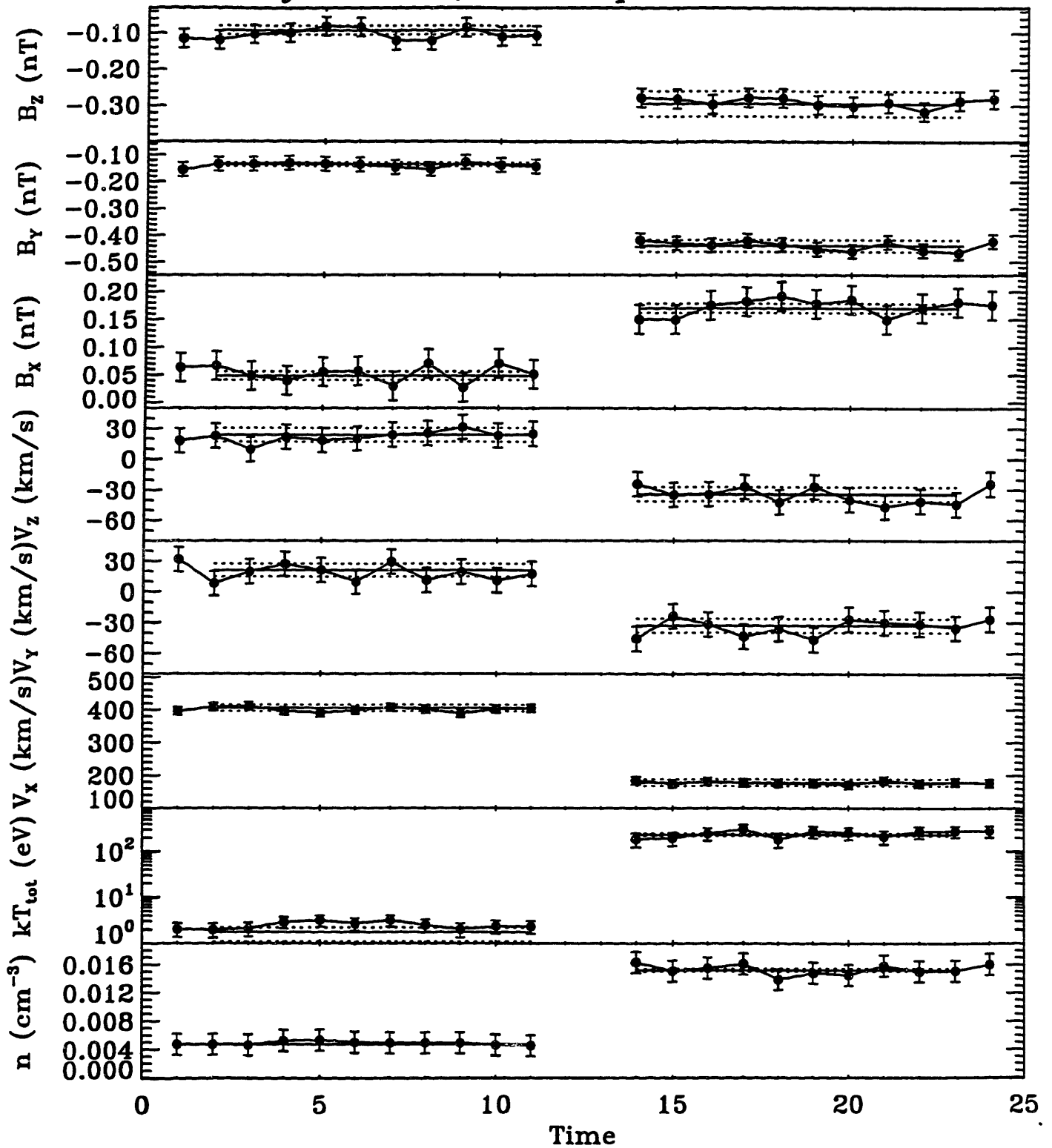


Fig. 2.3. Fit results of the asymptotic magnetofluid variables for a synthetic quasi-perpendicular shock. The dots with error bars represent the simulated measurements, the solid lines show the results of the fit, and the dotted lines show the standard deviation intervals.

Synthetic Oblique Shock

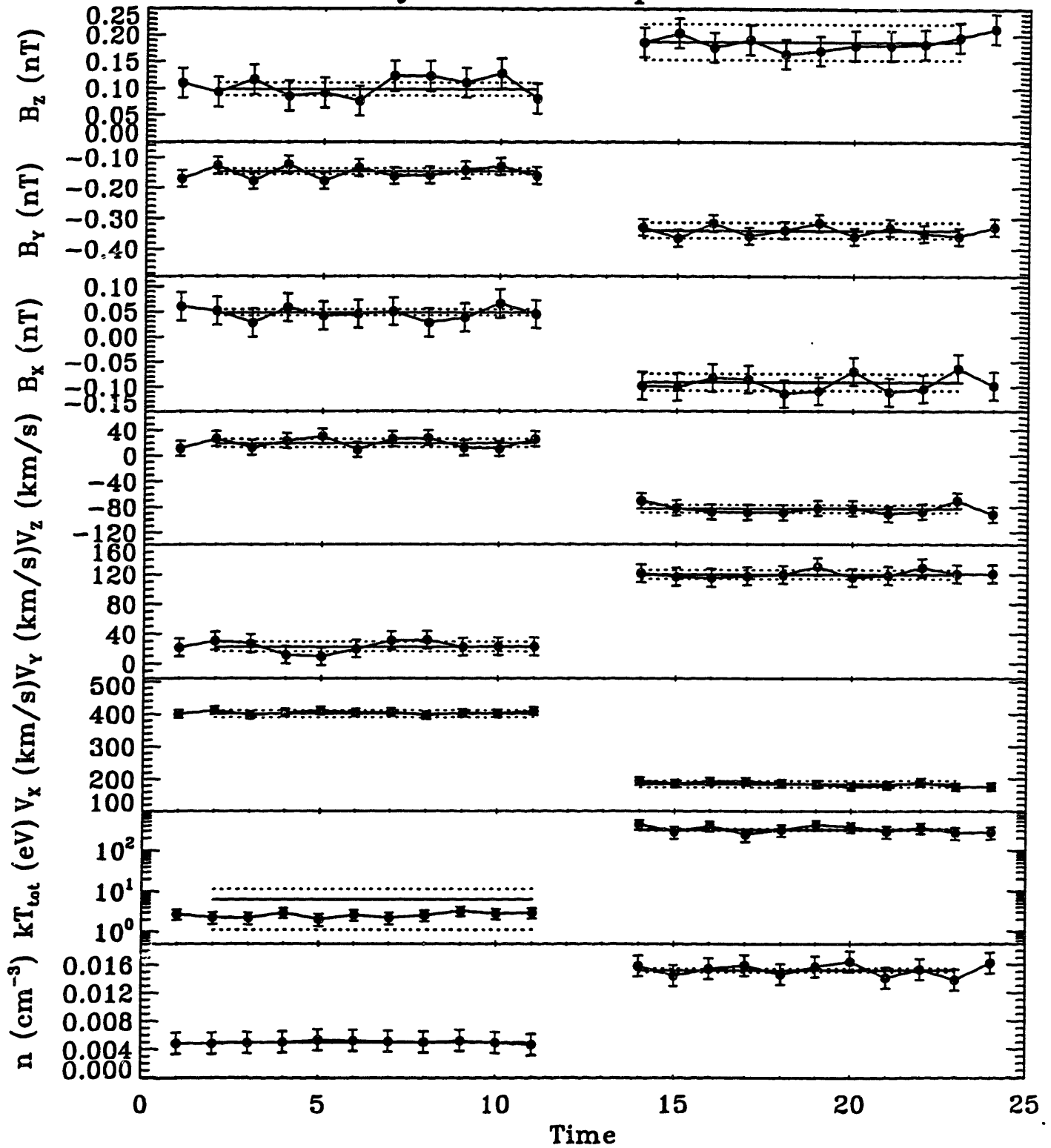


Fig. 2.4. Fit results of the asymptotic magnetofluid variables for a synthetic quasi-parallel shock. The dots with error bars represent the simulated measurements, the solid lines show the results of the fit, and the dotted lines show the standard deviation intervals.

Synthetic Quasi-Parallel Shock

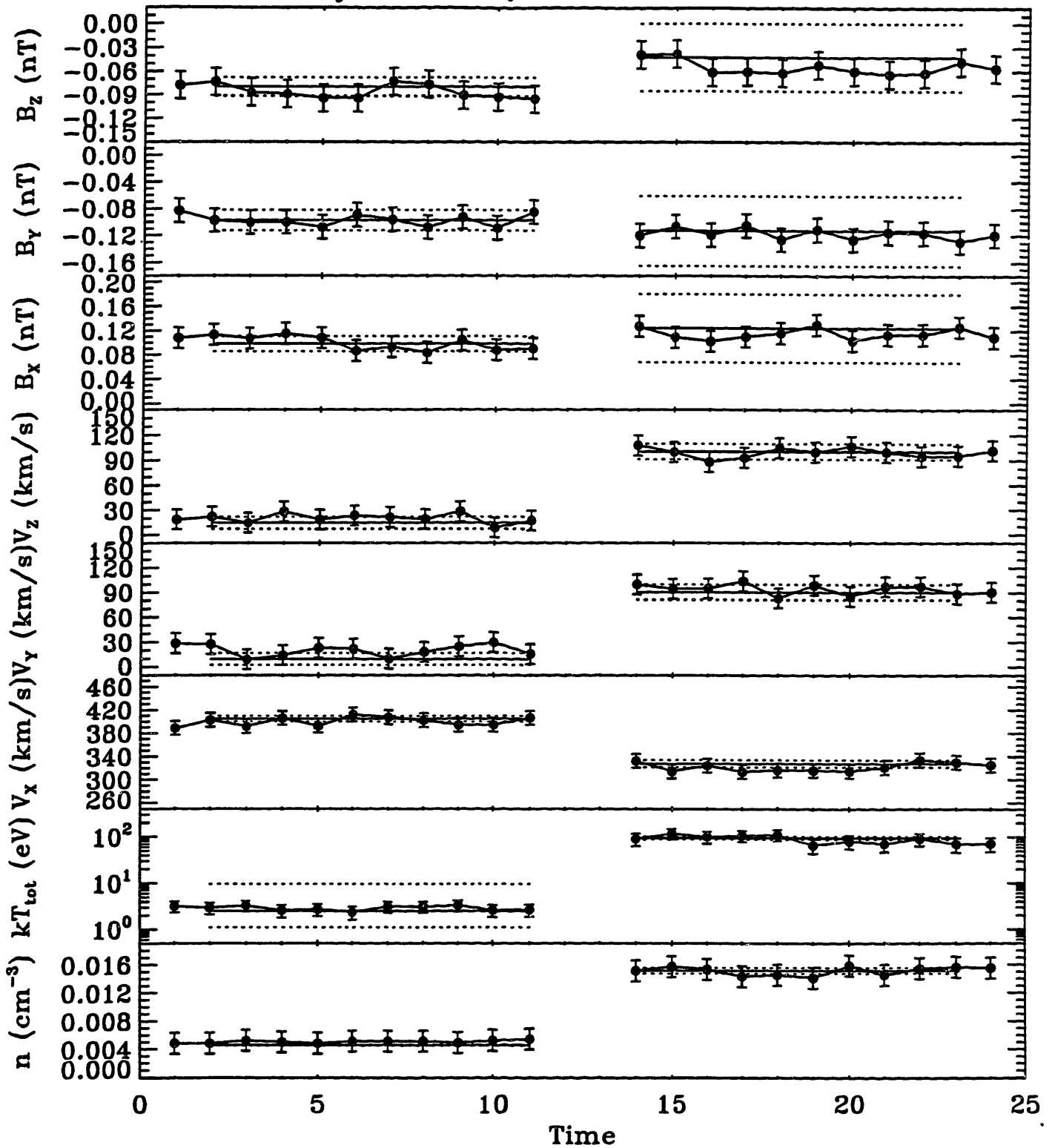


Fig. 2.5. Fit results of the asymptotic magnetofluid variables for a synthetic oblique shock. The dots with error bars represent the simulated measurements, the solid lines show the results of the fit, and the dotted lines show the standard deviation intervals.

symmetrically pairing up points one-to-one. The same comparison using quasi-parallel or quasi-perpendicular synthetic shocks yields similar results. Our method is preferred because, in addition to determining more parameters, it automatically eliminates spurious solutions which have to be manually checked and rejected if the VS method is used. The velocity coplanarity method gave reasonable solutions, but clearly the newer techniques fared much better. The velocity coplanarity technique becomes particularly unreliable for shocks of θ_{Bn} less than $30^\circ - 35^\circ$.

In summary, an improved iterative non-linear least squares technique was developed to fit spacecraft measurements to the idealized non-dissipational MHD jump conditions of shocks known as the "Rankine-Hugoniot problem". This method largely builds on the earlier method of *Viñas and Scudder* [1986]. Both techniques make the assumption that ideal MHD jump conditions provide good descriptions of observed space plasma shocks. Further, they assume that the plasma pressure is isotropic (can be described by a single scalar quantity), and that the plasma distribution function is a completely thermalized Maxwellian distribution or appropriate corrections can be introduced to obtain meaningful plasma density, velocity and temperature parameters. If these conditions are satisfied, then both methods provide geometrical (shock normal direction and shock bulk speed) and physical (the asymptotic magnetofluid parameters on both sides of the shock) characteristics of the analyzed shock.

Our new method improves on the VS technique by including the plasma temperature observations via use of the perpendicular momentum flux and energy density flux conservation equations in our model. The constraints of these two equations remove spurious solutions given by the VS method. Also, this improvement makes it possible to find the asymptotic values of the total plasma temperatures, and to fit for the best values of the ratio of the specific heats, γ , on both sides of the shock. Further improvement includes the proper treatment of individual measurement errors: weighting against less reliable observation points, and a complete

description of possible representations of confidence limits of the fit solutions (presented in the next section). Furthermore, we allow the formation of all possible combinations of the data point pairs across the shock to improve the statistics of the results. Synthetic shocks with a wide range of geometry and with very large error bars and superimposed noise are used to validate and compare our method with earlier techniques. We find that our method fares better than the preaveraged technique of velocity coplanarity and at least as well as the VS method while still providing the above described improvements.

2.2.3. Confidence Regions in the MHD Fit Method

We can find or estimate the confidence regions around our best fit results in several ways. When an analytical solution of the fit problem is not possible and we resort to the non-linear least squares technique of χ^2 minimization, knowledge of the confidence regions is essential for the determination of the best shock normal direction in two dimensional parameter space.

The simplest but crudest technique involves the use of only the diagonal elements of the covariance matrix C generated by the Levenberg-Marquardt method. The one standard deviation error in one of the fitted parameters a_i is given by:

$$\delta a_i = \pm \sqrt{\Delta\chi_v^2} \sqrt{C_{ii}} \quad (2.22)$$

[Press *et al.*, 1986] where the square root of the appropriate diagonal element of the covariance matrix is multiplied by the square root of the change in χ^2 corresponding to v number of fitted parameters (2 in the case of the shock normal fit) and a certain confidence interval p . Normally p is selected to be 68.3% to correspond to the one dimensional definition of one standard deviation. The appropriate value for a two dimensional fit with a one σ confidence region is $\Delta\chi_v^2 = 2.3$ [Press *et al.*, 1986]. This technique, though quick and simple, ignores the

correlation between the fitted parameters, since the off-diagonal elements of C , containing the correlation coefficients, are not used. However, the other two techniques provide 2-dimensional regions of various shapes rather than simple scalars. Therefore, whenever one wants to give simple error bars in numerical form, this method has to be employed.

For the two dimensional problem, a more accurate measure of a confidence region is an elliptical shape centered on the best fit value. The matrix equation of the elliptical confidence region is:

$$\Delta\chi_v^2 = \delta\mathbf{a} \cdot [\mathbf{C}]^{-1} \cdot \delta\mathbf{a} \quad (2.23)$$

[Press *et al.*, 1986] where $[\mathbf{C}]^{-1}$ is the inverse of the covariance matrix. Again, the value of $\Delta\chi_v^2$ corresponds to v number of fitted parameters and a certain degree of confidence p . The above matrix equation can be expanded into scalar form:

$$\Delta\chi_v^2 = C_{11}^{-1}\delta a_1^2 + (C_{12}^{-1} + C_{21}^{-1})\delta a_1\delta a_2 + C_{22}^{-1}\delta a_2^2 \quad (2.24)$$

where C_{ij}^{-1} are the elements of the inverted covariance matrix. Equation (2.24) is an equation of an ellipse; if provided with the appropriate offset to center it on the best fit, it describes the elliptical confidence region. This technique, though more sophisticated than the previous one, has serious limitations in describing the shape of the confidence region.

The most comprehensive and accurate description of the confidence region of a fit is given by a complete χ^2 map. Once the appropriate value of $\Delta\chi_v^2$ is determined based on the number of fitted parameters and the degree of confidence required, a contour line is sought at the altitude of $\chi_{\min}^2 + \Delta\chi_v^2$ in the parameter space of our solution. With this method no limitation is placed on either the shape or location of the confidence region sought. (Note that nowhere is it required that the region be simply connected. Actually, for high confidence levels, it is quite often disjoint.) This method was used to determine the shape of various confidence levels

shown in the graphical representation of our results.

2.3. The MHD Characteristics of the Shock

We now use the technique developed above to fit the Voyager 2 observations of the Neptunian inbound bow shock. Since our analysis requires a single fluid approximation, the ion density and bulk velocity along with the sum of the electron and ion temperatures are taken as the single fluid parameters. Downstream from the shock the situation is further complicated by the double Maxwellian ion distribution. The total ion density we use is the sum of the two components and the total temperature is the density-weighted average of the individual ion component temperatures. The velocities of the two components, as described in Chapter 1, are constrained to remain the same during the fitting procedure. In addition to the single fluid limitation, our analysis requires the prior selection of an upstream and downstream region of measurement where small scale, non-MHD shock effects are negligible, yet where we are still close enough to the shock that large scale variations in the solar wind and magnetosheath are not included. In the case of Neptune, we are fortunate that the solar wind conditions are extremely steady for a number of hours before the bow shock crossing, eliminating any difficulty in the selection of the proper upstream region for the MHD approximation (see Figure 2.6). In the downstream region, however, the situation is markedly different. For the beginning of the downstream region, we select the time when the R component of the plasma bulk velocity and the T component of the magnetic field become steady at 15.15 hr on day 236, 1989. (Throughout this thesis, velocity and magnetic field measurements are quoted in a non-inertial heliographic 'RTN' coordinate system centered on Neptune. The R direction is radially outward along the Sun-Neptune line, T is perpendicular to R and the Sun's spin axis and is in the direction of the Sun's rotation, and N completes the right-handed system.) These

Neptunian Inbound Bow Shock

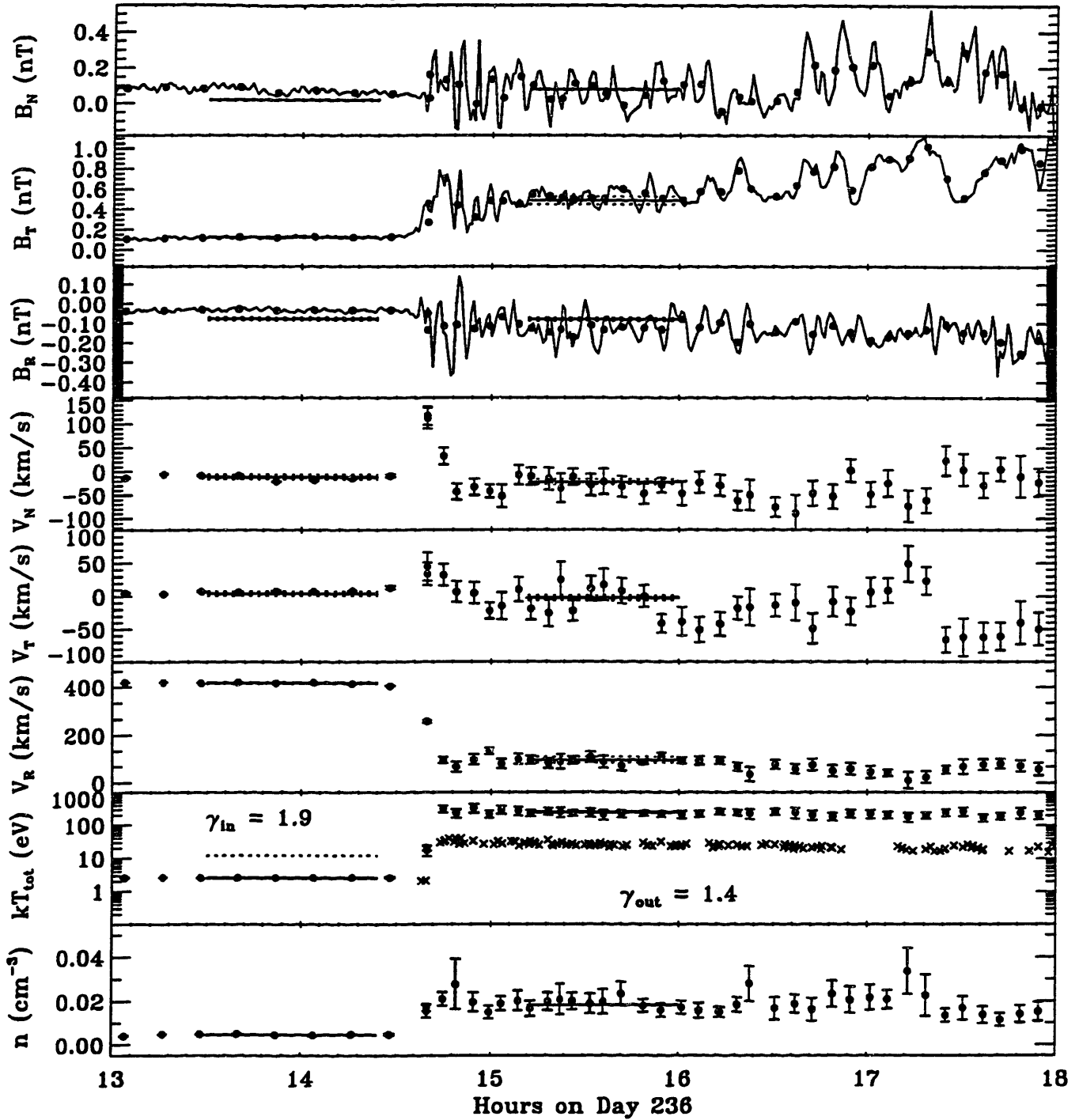


Fig. 2.6. Fit results of the asymptotic magnetofluid variables for the Neptunian bow shock. The solid dots represent the Voyager measurements, the solid lines show the fit results, and the dotted lines show the one standard deviation intervals. The solid dots on the thermal energy panel show the sum of ion and electron thermal energies; the crosses show the electron measurements where available. On the magnetic field panels, the wiggly lines show the high time resolution data, whereas the solid dots represent the averaged values used in our analysis.

components are selected because they show the largest variation during the shock crossing. The MHD region we select runs from this time until large scale changes not induced by the shock are observed. This end point is not well defined but seems to fall somewhere between 16 and 17 hrs on the same day. In our analysis various endpoints ranging between 16 and 17 hrs were explored; these resulted in only minor variations in the fitted parameters, well below one standard deviation level.

The plasma and magnetic field parameters in these regions are obtained from the Voyager 2 observations as described in Chapter 1. The only parameter not directly observable by the Voyager PLS instrument is the cold solar wind electron component. In order to obtain at least an approximate value of the upstream electron thermal energy, we turn to the empirical polytrope law of *Sittler and Scudder* [1980]. This empirical law is based on solar wind thermal electron observations between 0.45 and 4.76 AU as measured by Voyager 2 and Mariner 10. The law is extrapolated to the position of Neptune giving an estimated 2.1 eV electron thermal energy. This value we take as an upper limit, because an electron distribution any hotter than this would have an observable high energy tail by Voyager 2.

As expected for the nearly subsolar crossing of the Neptunian bow shock, the plasma bulk velocity drops to subsonic values across the shock. To conserve mass flux, the plasma density increases giving a shock strength η ($\eta = \rho_2/\rho_1$) of 4.2 ± 0.8 . A value larger than 4 is not physically impossible for η because even in the polytrope approximation the maximum value of $\eta_{\max} = (\gamma + 1)/(\gamma - 1)$ is larger than 4 for γ less than 5/3. Also the single standard deviation includes values for η less than 4. The magnetic field strength increases significantly across the shock. When our complete RH non-linear least squares technique is applied to the Neptunian shock data in the MHD region, the shock unit normal found is $(-0.999, 0.001, -0.030) \pm (0.001, 0.009, 0.014)$ in RTN coordinates, almost exactly anti-sunward in direction as is expected from Voyager 2's nearly subsolar crossing of the bow shock. The unit shock normal

is very well resolved as is shown graphically by the confidence regions in spherical parameter space in Figure 2.7 (The loci of all of the possible unit shock normals is the unit sphere. Our analysis technique finds regions on this sphere giving the best possible fit to the measured data corresponding to various confidence levels. In Figure 2.7 only a 7° conical section of the sphere around the Sun-Neptune line is shown. The gray scale bar at the bottom of the graph indicates the various confidence levels.) The angle between the shock normal and the local interplanetary magnetic field (θ_{BN}) is $58.2^\circ \pm 2.3^\circ$, characterizing the Neptunian inbound bow shock as a quasi-perpendicular shock. The shock moves with a speed of 15 ± 12 km/s away from the planet towards the Sun. Since the solar wind ram pressure is very stable upstream from the shock for a considerable amount of time, the most likely reason for the bulk motion of the shock is the changing magnetic configuration of the planetary magnetosphere.

The asymptotic magnetofluid parameters obtained by our analysis are plotted in Figure 2.6 as solid lines; dotted lines show one σ standard deviations (for some parameters, i.e., the density, the standard deviation is so small that it is lost in the width of the solid line). On the downstream side, the asymptotic results are plotted over the shortest range used in the analysis, while upstream a longer range was used in the analysis than suggested by the length of the solid lines. The same results are numerically tabulated in Table 2.3. As is evident, the plasma and magnetic field results show remarkable agreement with the spacecraft measurements. Based on these results, the Neptunian inbound bow shock can be characterized as a low β , high Mach number, strong quasi-perpendicular shock. Upstream the polytrope index (γ) could not be clearly resolved because of large uncertainties, but the value of 1.9 gave the best fit with a large uncertainty. This large value of γ is just 1 σ away from the upper limit allowed by the polytrope shock strength limitation discussed earlier. A value of γ close to 2 is consistent with the results of *Slavin et al.* [1985] obtained from gas dynamic models of the Jupiter and Saturn bow shocks. The higher value of γ implies that the available number of degrees of

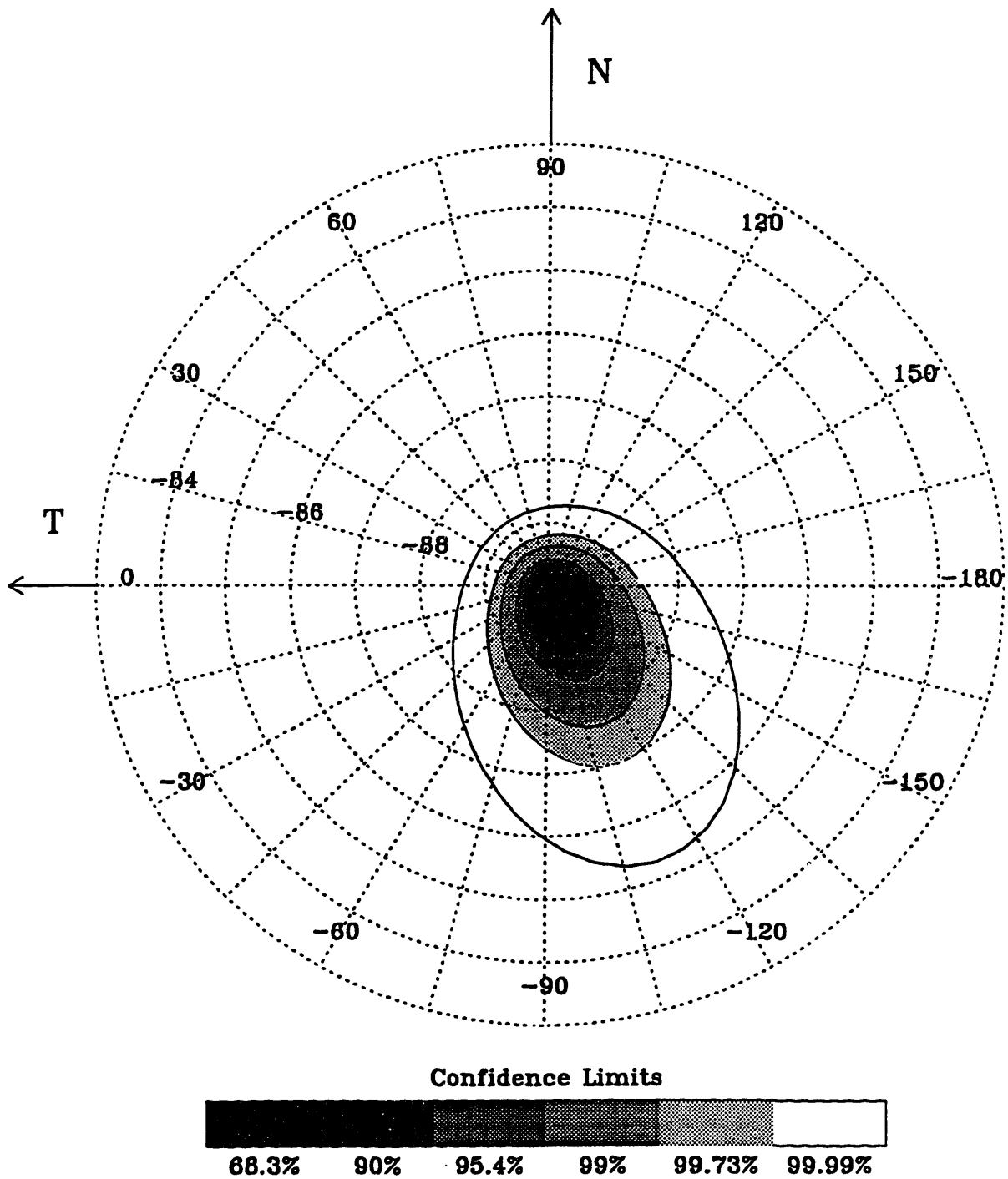


Fig. 2.7. Confidence regions of the Neptunian bow shock unit normal; an expanded view of parameter space near the -R direction. The annotation is in spherical coordinate angles with the polar angle measured from the R axis (0° at the TN plane) and the azimuth angle from the T axis following the right hand rule. The various confidence limits are indicated by the shaded bar at the bottom.

Neptune Inbound Bow Shock

		Observations	Fit Results
\hat{n}_R		...	0.999 ± 0.001
\hat{n}_T		...	-0.001 ± 0.009
\hat{n}_N		...	0.030 ± 0.014
V_S	(km/s)	...	-15.0 ± 12.0
θ_{Bn}	(deg)	...	58.2 ± 2.3
<hr/>			
n_1	(cm ⁻³)	0.0046 ± 0.0003	0.0047 ± 0.0001
V_{R_1}	(km/s)	419.11 ± 1.68	418.08 ± 3.25
V_{T_1}	(km/s)	5.82 ± 1.38	4.26 ± 3.67
V_{N_1}	(km/s)	-11.85 ± 4.30	-11.41 ± 5.47
T_{tot_1}	(eV)	$< 2.6^*$	2.6 ± 9.6
B_{R_1}	(nT)	-0.035 ± 0.017	-0.078 ± 0.009
B_{T_1}	(nT)	0.116 ± 0.018	0.123 ± 0.003
B_{N_1}	(nT)	0.077 ± 0.019	0.018 ± 0.003
<hr/>			
n_2	(cm ⁻³)	0.0188 ± 0.0026	0.0183 ± 0.0005
V_{R_2}	(km/s)	93.39 ± 12.96	95.79 ± 12.41
V_{T_2}	(km/s)	-8.95 ± 24.10	-2.22 ± 4.09
V_{N_2}	(km/s)	-25.23 ± 15.57	-22.18 ± 5.54
T_{tot_2}	(eV)	235.7 ± 27.8	249.5 ± 3.3
B_{R_2}	(nT)	-0.124 ± 0.029	-0.079 ± 0.009
B_{T_2}	(nT)	0.518 ± 0.042	0.488 ± 0.039
B_{N_2}	(nT)	0.076 ± 0.053	0.078 ± 0.033

* The upper limit of the electron component of the total temperature is estimated based on the *Sittler and Scudder* [1980] polytrope law.

Table 2.3. Neptunian shock parameters derived from our MHD fit model and a comparison of the asymptotic magnetofluid parameters to the error-weighted average of the same observed quantities.

freedom of the plasma is closer to two than to three. Downstream, the polytrope index is resolved and equals to 1.4, suggesting an increased number of degrees-of-freedom.

2.4. The Shock Microstructure

Unfortunately, the plasma measurements do not have a high enough time resolution to clearly resolve the microstructure of the Neptunian bow shock. Therefore, the much higher resolution magnetic field data is used to determine the apparent scale lengths of the different non-MHD features. The shock foot is characterized by a small but systematic increase in the magnetic field over the steady solar wind values, immediately upstream. It is generally attributed to the presence of reflected ions from the shock [*Paschmann et al.*, 1982]. After the foot, the magnetic field increases sharply in the ramp, reaching values well above the steady downstream conditions and producing the overshoot. After the peak of the overshoot, a strongly damped oscillation occurs until conditions stabilize on the downstream side. All of these features are clearly marked on Figure 2.8. The thinner, highly oscillating line is the 48s average magnetic field magnitude. The thicker line is the 4 point box-car averaged graph of the same data. It helps to eliminate some of the high frequency noise in order to localize the various microstructure features.

Voyager 2 was in the foot region between 1446 SCET and 1461 SCET (The uncertainties in the times, due to the ambiguity in the boundaries of the region, are marked on Figure 2.8). Using the above obtained shock speed and the known velocity of the spacecraft perpendicular to the shock surface (16.2 km/s), the width of the foot is 16800 ± 8600 km. There are several available model calculations of similar quasi-perpendicular shocks. *Schwartz et al.* [1983] estimates the foot width to be 0.7 times the effective ion gyroradius defined as $r'_{gi} = (\mathbf{V}_{sw} \cdot \hat{\mathbf{n}} - V_{shock}) / \Omega_{ci}$, where \mathbf{V}_{sw} is the upstream solar wind velocity, V_{shock} is the

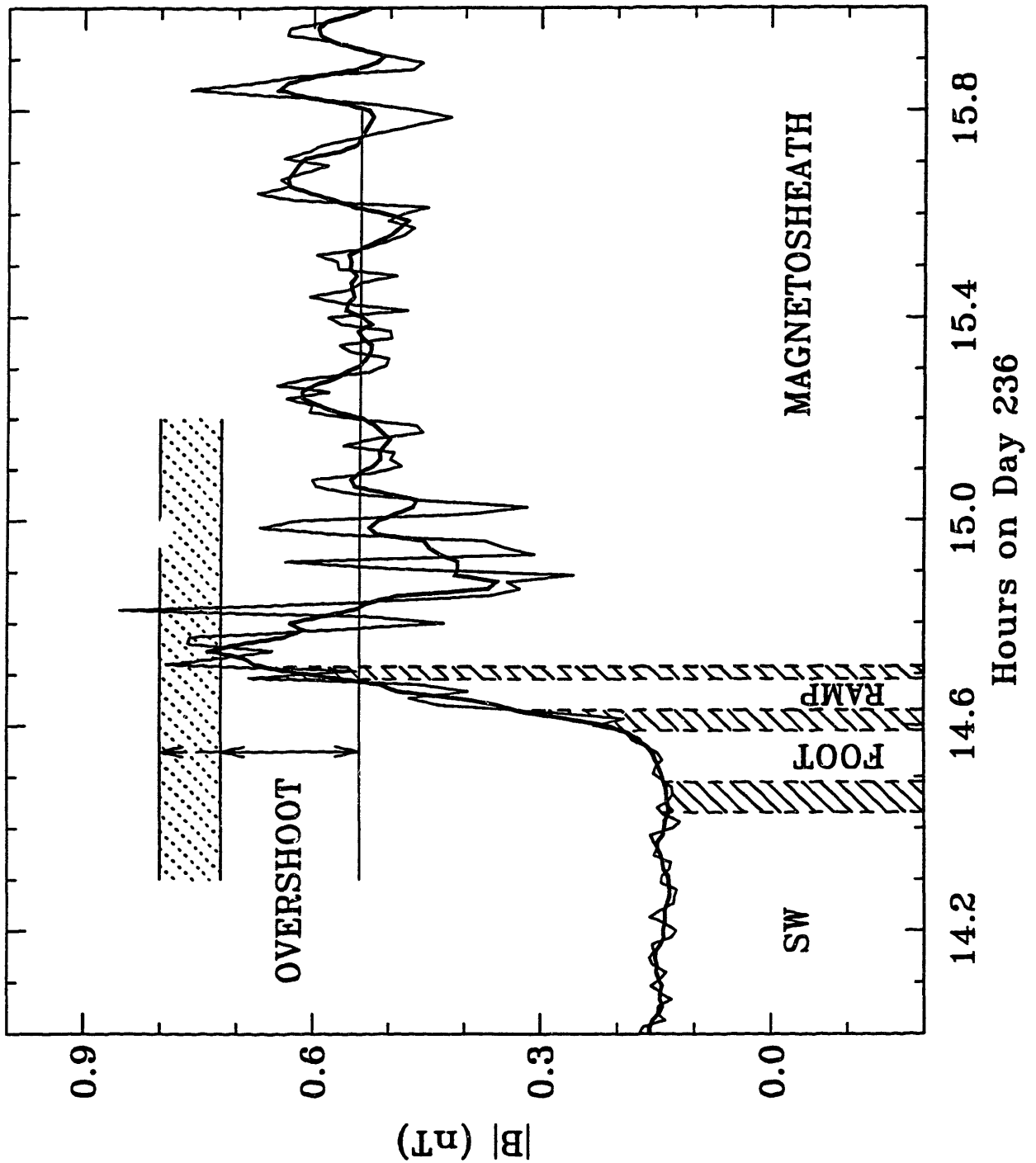


Fig. 2.8. A description of the microstructure of the Neptunian bow shock as observed in the magnetic field magnitude. The shaded regions show the uncertainties, due to the ambiguity in the boundaries, in the scale length of each structure. See the text for detailed definitions.

above obtained bulk speed of the shock, and $\Omega_{ci} = eB/m_p$ is the proton cyclotron frequency. If we substitute the appropriate values from the Neptunian bow shock region into this expression, we obtain for the theoretically predicted value of the foot width 22000 ± 2800 km. (See Table 2.4 for relevant scale lengths.) The model calculations of *Goodrich* [1985] give a smaller value of $0.33 r'_{gi}$ i.e. 10500 ± 1300 km. *Leroy et al.* [1982] find that the foot scales with c/ω_{pi} (3360 ± 110 km), where ω_{pi} is the proton plasma frequency upstream of the shock ($\omega_{pi}^2 = ne^2/\epsilon_0 m_p$ with n the proton number density), as an order of magnitude estimate. All of these results fall within the error bars of our observations, and therefore, we are unable to differentiate between the various models based on which describes the observations better. Turning from theoretical predictions to observations of the same features at the Earth's bow shock, ISEE 1 measurements give a foot width of $3 c/\omega_{pi}$ [*Scopke et al.*, 1983]. Using parameters appropriate for Neptune, this result yields 10110 ± 330 km for the foot width, somewhat smaller than what is observed. At Uranus, *Bagenal et al.* [1987] was able to match the observed shock foot length with the predictions of *Schwartz et al.* [1983] by allowing the shock to move away from the planet at 2 km/s. The observed scale lengths at Neptune and at other planets of the various microstructure features, along with the theoretical predictions are tabulated in Table 2.5.

The ramp, where the magnetic field strength increases at a very high rate, lasted in the Neptune inbound bow shock till 1470 SCET, giving a ramp width of 10950 ± 5600 km. (The uncertainties of this region are marked again in Figure 2.8) Early theoretical studies suggest that the ramp is governed by the electron resistivity and therefore it should scale with the electron inertial skin depth, c/ω_{pe} , where ω_{pe} is the electron plasma frequency upstream of the shock [see for example the review of *Goodrich*, 1985 and references within]. However, observations at Earth suggest an order of magnitude larger scale length [*Scopke et al.*, 1983], which with Neptune parameters gives 784 ± 26 km, still an order of magnitude too small

Shock Parameters and Scale Lengths

	Definition	Upstream	Downstream
T_i (eV)		0.49 ± 0.04	207.5 ± 27.6
T_e (eV)		$< 2.1^*$	27.8 ± 3.9
β_i	$2\mu_0nkT_i/B^2$	0.044 ± 0.012	5.4 ± 1.3
β_e	$2\mu_0nkT_e/B^2$	$< 0.19^*$	0.73 ± 0.18
β_T	$\beta_i + \beta_e$	$< 0.23^*$	6.2 ± 1.4
$M_S = U/C_S$	$U = V_n - V_S; C_S^2 = kT_e/m_p$	$> 30.6^*$	2.09 ± 0.37
$M_p = U/w_{th}$	$w_{th}^2 = 2kT_i/m_p$	44.5 ± 2.1	0.54 ± 0.10
$M_A = U/V_A$	$V_A^2 = B^2/\mu_0nm_p$	9.36 ± 1.24	1.26 ± 0.25
$M_{MS} = U/C_{fms}$	$C_{fms}^2 = C_S^2 + V_A^2$	8.95 ± 1.09	1.08 ± 0.20
M	$M^2 = m_p U^2/k(T_i + T_e)$	$> 27.5^*$	0.72 ± 0.13
<hr/>			
r_{gi} (km)		$706. \pm 92.$	$3870. \pm 395.$
r_{ge} (km)		$< 33.9^*$	33.1 ± 3.5
c/ω_{pi} (km)		$3360. \pm 110.$	$1660. \pm 115.$
c/ω_{pe} (km)		78.4 ± 2.6	38.8 ± 2.7
r'_{gi} (km)	$r'_{gi} = U_{Upstream} / \Omega_{ci}$	$31400. \pm 4000.^a$	$8400. \pm 700.^b$

* The upper limit of the solar wind electron temperature is estimated from the polytrope model of *Sittler and Scudder [1980]*

^a $(V_{sw} \cdot \hat{n} - V_{shock}) / (\Omega_{ci})_{Upstream}$

^b $(V_{sw} \cdot \hat{n} - V_{shock}) / (\Omega_{ci})_{Downstream}$

Table 2.4. Observed plasma parameters and scale lengths at the Neptunian inbound bow shock.

The Microstructure of the Neptunian Bow Shock

Definition	Neptune Observations	Model Predictions	Observations at Other Planets
Foot (km)	16800 ± 8600	<i>Schwartz et al.</i> [1983] $0.7 r'_{gi}$ 22000 ± 2800 <i>Goodrich</i> [1985] $0.33 r'_{gi}$ 10500 ± 1300 <i>Leroy et al.</i> [1982] $\approx c/\omega_{pi}$ 3360 ± 110	<i>Sckopke et al.</i> [1983] ISEE 1 at Earth $3 c/\omega_{pi}$ 10110 ± 330 <i>Bagenal et al.</i> [1987] Voyager 2 at Uranus $0.7 r'_{gi}$ 22000 ± 2800
Ramp (km)	10950 ± 5600	Early studies $\approx c/\omega_{pe}$ 78.4 ± 2.6 <i>Leroy et al.</i> [1982], <i>Schwartz</i> [1985] c/ω_{pi} 3360 ± 110	<i>Sckopke et al.</i> [1983] ISEE 1 at Earth $10 c/\omega_{pe}$ 784 ± 26 <i>Bagenal et al.</i> [1987] Voyager 2 at Uranus $0.2 c/\omega_{pi}$ 672 ± 22
Overshoot Region (km)	17000 ± 5000	<i>Goodrich</i> [1985] $2V_{up}/3\Omega_{ci}$ 20960 ± 2660	<i>Sckopke et al.</i> [1983] ISEE 1 at Earth $6 c/\omega_{pi}$ 20160 ± 660
Damped Oscillation Wavelength (km)	22900 ± 3300		<i>Bagenal et al.</i> [1987] Voyager 2 at Uranus $\approx r'_{gi}$ 31000 ± 4000

Table 2.5. Comparison of the Neptunian inbound bow shock microstructure with model predictions and observations at other planets.

compared to our observations. Other model calculations succeed increasing the ramp size by increasing the electron resistivity (η) in this region, and reach the estimate of an ion inertial skin depth, c/ω_{pi} (3360 ± 110 km) [Leroy *et al.*, 1982, Schwartz, 1985]. The Neptune observations give a ramp width on the order of $3 c/\omega_{pi}$, which can be modeled if we adapt a resistive scale length, $L_r = c^2\eta/4\pi V_{up}$ with an electron resistivity of $\eta/4\pi = 5.3 \times 10^{-5}$ (where $V_{up} = V_{sw} \cdot \hat{n} - V_{shock}$). This value corresponds to a collision frequency of $\nu/\omega_{pi} = \eta\omega_{pe}^2/4\pi\omega_{pi} = 8.7$. This value of resistivity, though is within the range explored by Leroy *et al.* [1982], is an order of magnitude higher than typically used even for anomalous resistivity expected from cross field instabilities. Although this model's treatment of the electron component is only approximate, our observational result raises the question whether the plasma density is still sufficiently coupled to the magnetic field. In contrast, preliminary studies at the Uranus subsolar bow shock reveal a much thinner ramp region [Bagenal *et al.*, 1987].

After the fast rising ramp, the magnetic field overshoots the average downstream value. After it reaches its maximum value at 1473 SCET, it starts a downward trend resulting in an undershoot and continues in a strongly damped oscillatory phase. The overshoot region has the physical extent of 17000 ± 5000 km. The ISEE 1 observations at Earth reveal an overshoot region of $6 c/\omega_{pi}$ thickness [Sckopke *et al.*, 1983] corresponding to 20160 ± 660 km at Neptune. The model calculations of the same region by Goodrich [1985] result in a thickness of $2V_{up}/3\Omega_{ci}$. This model approximation gives 20960 ± 2660 km for Neptune, well within the error bars of our observations.

The maximum value of magnetic field strength (B_{max}), measured inside the shock region, is 0.76 ± 0.04 nT, after which it settles at an average value of $B_{down} = 0.54 \pm 0.02$ nT. The overshoot $O = (B_{max} - B_{down}) / B_{down}$ is 0.41 ± 0.09 . Comparing this value with observations of supercritical shocks at other planets compiled by Russell *et al.* [1982] (the Uranus result is

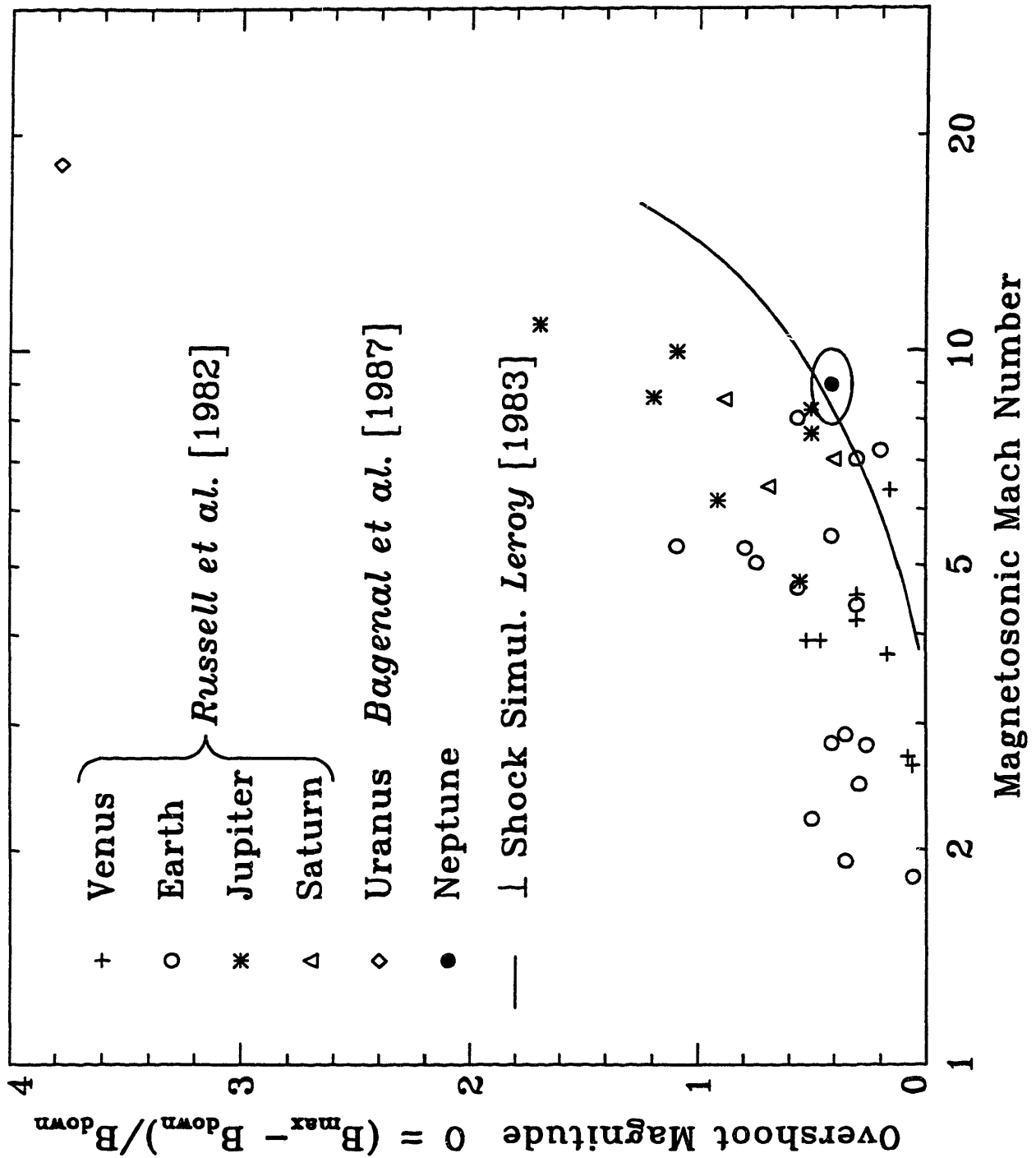


Fig. 2.9. Plot of shock overshoot vs. magnetosonic Mach number for various planetary bow shocks. The ellipse around the Neptune data point is the one standard deviation confidence region. The solid curve is the result of theoretical modeling by Leroy [1983] of low β perpendicular shocks.

from *Bagenal et al.* [1987]), the Neptune results fall on the edge of a cluster of observations in excellent agreement with model predictions [*Leroy*, 1983] (see Figure 2.9). *Leroy* has modeled low β (0.25) perpendicular shocks very similar to the observed Neptunian inbound bow shock. The bow shocks of the other gas giants usually show greater difference from this model, possibly due to the much higher values of β typically observed. The magnetosonic Mach number of the Neptune bow shock, although large in respect to typical Earth observations, is not high compared to shocks observed at the other outer planets, so the Neptune results do not improve the analysis of the possible power law dependence of the overshoot on the Mach number of the shock [*Leroy*, 1983; *Quest*, 1986].

After the overshoot, the magnetic field passes through a deep undershoot followed by a strongly damped oscillation. Based on the first full period of oscillation, the wavelength is 22900 ± 3300 km corresponding to about one upstream effective gyroradius. At Uranus, a similar relationship was observed [*Bagenal et al.*, 1987]. After 3 periods, the oscillation is lost in the general fluctuation of the sheath magnetic field.

In summary, the Voyager 2 observation of the upstream, nearly subsolar crossing of the Neptunian bow shock prompted us to extend the non-linear MHD shock jump condition fitting technique of *Viñas and Scudder* [1986], described by *Szabo* [1993]. This improved method was applied to the data set collected at Neptune. Based on the fit results, we characterize the Neptunian inbound bow shock to be a low β , high Mach number, quasi-perpendicular strong shock slowly moving away from the planet toward the Sun. Once the shock speed was established, we were able to determine the scale lengths of the various shock microstructure features. The shock foot, overshoot region and magnitude, and downstream damped oscillation wavelength are in good agreement with model predictions. The ramp region appeared significantly thicker than expected from model predictions. The observed ramp size can be modeled with an anomalously high electron resistivity.

CHAPTER 3

THE INBOUND MAGNETOSHEATH

3.1 Introduction

After the analysis of the inbound bow shock described in the previous chapter, we now turn our focus to the inbound magnetosheath. The magnetosheath is the region of the shocked solar wind between the bow shock and the magnetopause of a planet. (For a graphical representation see Figure 1.1.) The plasma flow lines in this region divert around the obstacle posed by the planetary magnetosphere. At the inner boundary of this region, where the magnetosheath plasma abuts the magnetopause, energy is transferred from the solar wind to the magnetosphere. Also, because of the unique subsolar cusp configuration of Neptune occurring once every planetary rotation, significant amount of magnetosheath plasma is expected to enter the upper magnetospheric regions. Thus it is important to understand the physics controlling the plasma processes in the magnetosheath.

The goal of this chapter is to quantify the plasma and magnetic field changes which occur in the dayside magnetosheath by comparing the observations with gas dynamic predictions of the plasma and magnetic field parameters in this region. The gas dynamic model with convected magnetic field, first described by *Spreiter et al.* [1966], has had great success in modeling magnetosheath flow at Venus, Earth, Jupiter, and Saturn [*Spreiter et al.*, 1966; *Spreiter and Stahara*, 1985; *Slavin et al.*, 1985; *Russell*, 1985; *Stahara et al.*, 1989]. In this chapter we apply this model to Neptune's magnetosheath. Due to Neptune's rotation and unique dipole axis configuration, as described in Chapter 1, Voyager 2 travels into the high magnetic latitude regions of the dayside magnetosheath never observed by any other spacecraft. Thus we have the opportunity to test the accuracy of the model for a new magnetospheric orientation and in a

new region of space.

3.2 The Gas Dynamic Model of the Sheath

The objective of the gas dynamic model is not a complicated theory that encompasses all phenomena in the magnetosheath, but rather the simplest body of analysis that appears able to describe the average bulk properties of the solar wind as it flows steadily through the bow shock and around the forward portion of the magnetosphere. The fundamental assumption is that the flow can be described adequately by the standard magnetohydrodynamic equations for steady flow (i.e. all time derivatives vanish) of a dissipationless perfect gas. No attempt will be made here to justify this assumption in detail, except to remark that the presence of a weak and irregular magnetic field in the incident solar wind plasma seems sufficient to couple the motions of the particles even in the absence of collisions. Also, as pointed out above, the empirical evidence from other planets seems to support the use of this simplified model.

The differential equations of the steady state plasma flow in MKS system, which are the magnetohydrodynamic (MHD) equations and the Maxwell equations with all the time derivatives set to zero, as well as the equation of entropy conservation and perfect gas equation are as follows (see e.g. *Landau et al.* [1984])

$$\nabla \cdot (\rho \mathbf{v}) = 0 \quad (3.1)$$

$$\rho(\mathbf{v} \cdot \nabla)\mathbf{v} + \nabla P = -\frac{1}{\mu_0} \mathbf{B} \times (\nabla \times \mathbf{B}) \quad (3.2)$$

$$\nabla \times (\mathbf{v} \times \mathbf{B}) = 0 \quad (3.3)$$

$$\nabla \cdot \mathbf{B} = 0 \quad (3.4)$$

$$(\mathbf{v} \cdot \nabla)S = 0 \quad (3.5)$$

$$P = e^{S/c_v} \rho^\gamma \quad (3.6)$$

where ρ , P , S , and \mathbf{v} refer to the density, pressure, entropy, and velocity of the plasma, B refers to the magnetic field strength, $\gamma = c_p/c_v$ with c_p and c_v the constants representing the specific heats at constant pressure and constant volume, and $\mu_0 = 4\pi \times 10^{-7}$ H/m, the magnetic permeability of free space. Important auxiliary relations for γ , the temperature T , the speed of sound C_s , the internal energy ε , and the enthalpy h are

$$\gamma = (N + 2)/N \quad (3.7)$$

$$P = nkT \quad (3.8)$$

$$C_s = \sqrt{\partial P / \partial \rho} = \sqrt{\gamma P / \rho} \quad (3.9)$$

$$\varepsilon = c_v T \quad (3.10)$$

$$h = c_p T = \varepsilon + P/\rho \quad (3.11)$$

where N represents the number of degrees of freedom, $n = \text{number of particles/cm}^3 = 2n_p$ where n_p is the number of protons/cm³, and $k = \text{Boltzmann's constant}$.

Although only first derivatives appear in this system of equations, the neglected dissipative terms are described by second derivatives. Their neglect requires that the gradients be small. In MHD, as in gas dynamics, however, compressions tend to coalesce and steepen into shock waves of such small thickness that they can be considered as virtual discontinuities. In addition, attraction between like currents tends to cause current distributions to collapse into thin sheaths, across which the magnetic field can be considered in the same sense to be nearly discontinuous. Mathematically, continuous solutions of the dissipationless differential equations cease to exist, and the flow is no longer governed solely by the equations given above. Mass, momentum, magnetic flux, and energy must still be conserved, however, and the jump condition equations given in Chapter 2 (equations (2.1) - (2.6)) must describe the plasma quantities on both sides of such a discontinuity.

The boundaries of the dayside magnetosheath are discontinuities of this kind. As was

discussed in detail in Chapter 2, the dayside bow shock is a fast shock. In contrast, a tangential discontinuity is assumed for the magnetopause as the simplest of boundary conditions (i.e. no plasma flow or magnetic flux through the magnetopause is allowed). Also, observations at various planets indicate that the gas pressure P is significantly larger than the magnetic field pressure $B^2/2\mu_0$ on the magnetosheath side at the magnetopause, and just the reverse on the magnetospheric side. So as far as the flow outside the magnetosphere is concerned, the discontinuity at the magnetopause may thus be approximated satisfactorily by those of the limiting case of a tangential discontinuity in which there is a vacuum on one side, and negligible magnetic pressure on the other side. It is demonstrated further by *Spreiter et al.* [1966] that the gas pressure on the magnetosphere boundary is adequately approximated by the simple Newtonian formula $P = K\rho_\infty v_\infty^2 \cos^2\psi$ where the subscript ∞ refers to the values in the undisturbed solar wind stream, ψ is the angle between the normal to the boundary and the velocity vector of the undisturbed stream, and K is a constant usually taken to be unity. However, we will find below that better accuracy was achieved if K is taken to be 0.84 for $\gamma = 2$. Though theoretically the shape of the magnetopause could be determined at this point, the difficulties associated with the non-linear and mixed elliptic-hyperbolic character of the governing partial differential equations are such that it is necessary at the present time to approximate the magnetosphere boundary with an axisymmetric shape determined from the crossings of the magnetopause by Voyager 2.

Although it has been necessary to invoke the presence of a magnetic field to provide a mechanism for providing interactions between the particles, and to consider the complications of hydromagnetic theory to provide an adequate description of the magnetosphere boundary as a tangential discontinuity and the bow wave as a fast MHD shock, the magnetic field strengths typically encountered in the solar wind and planetary magnetosheaths are sufficiently small as otherwise to produce only secondary effects on the plasma flow. On this basis, one can justify

the neglect of all terms containing the magnetic field strength B in equations (3.1) - (3.6) when calculating the plasma flow. The fluid motion then calculated is just exactly that indicated by ordinary gas dynamic theory. After the gas dynamic equations are used to calculate the plasma density, velocity, and pressure profile throughout the dayside magnetosheath, the deformations of the magnetic field are determined subsequently using the equations

$$\nabla \times (\mathbf{B} \times \mathbf{v}) = 0 \quad (3.12)$$

$$\nabla \cdot \mathbf{B} = 0 \quad (3.13)$$

$$[\mathbf{B}_n] = 0 \quad (3.14)$$

where the $[]$ indicates change across the bow shock. These equations are frequently interpreted as indicating that the magnetic field lines move with the plasma, that is, that the field lines are "frozen in". The predictions of this model are compared to the actual observations of Voyager 2 in the Neptunian magnetosheath.

3.3 Voyager 2 observations of the Sheath

The trajectory of Voyager 2 was discussed in Chapter 1 and shown on Figure 1.2. As it was mentioned there, the inbound bow shock was encountered at $34.0 R_N$ from the planet. After this, the spacecraft was in the dayside magnetosheath for 3.5 hours until it entered the cusp region (a region to be discussed in the next chapter) at about $26 R_N$ from Neptune.

Figure 3.1 shows the plasma parameters and magnetic field components for the inbound magnetosheath and for the solar wind preceding the bow shock crossing. (See Chapter 1 for a complete description of the PLS and MAG instruments and the method of plasma analysis employed.) Errors in the values for the solar wind are smaller than the dot size. We again use the *RTN* coordinate system where the *R* axis points radially outward along the Sun-Neptune line, the *T* axis lies in the solar equatorial plane pointing in the direction of Neptune's motion,

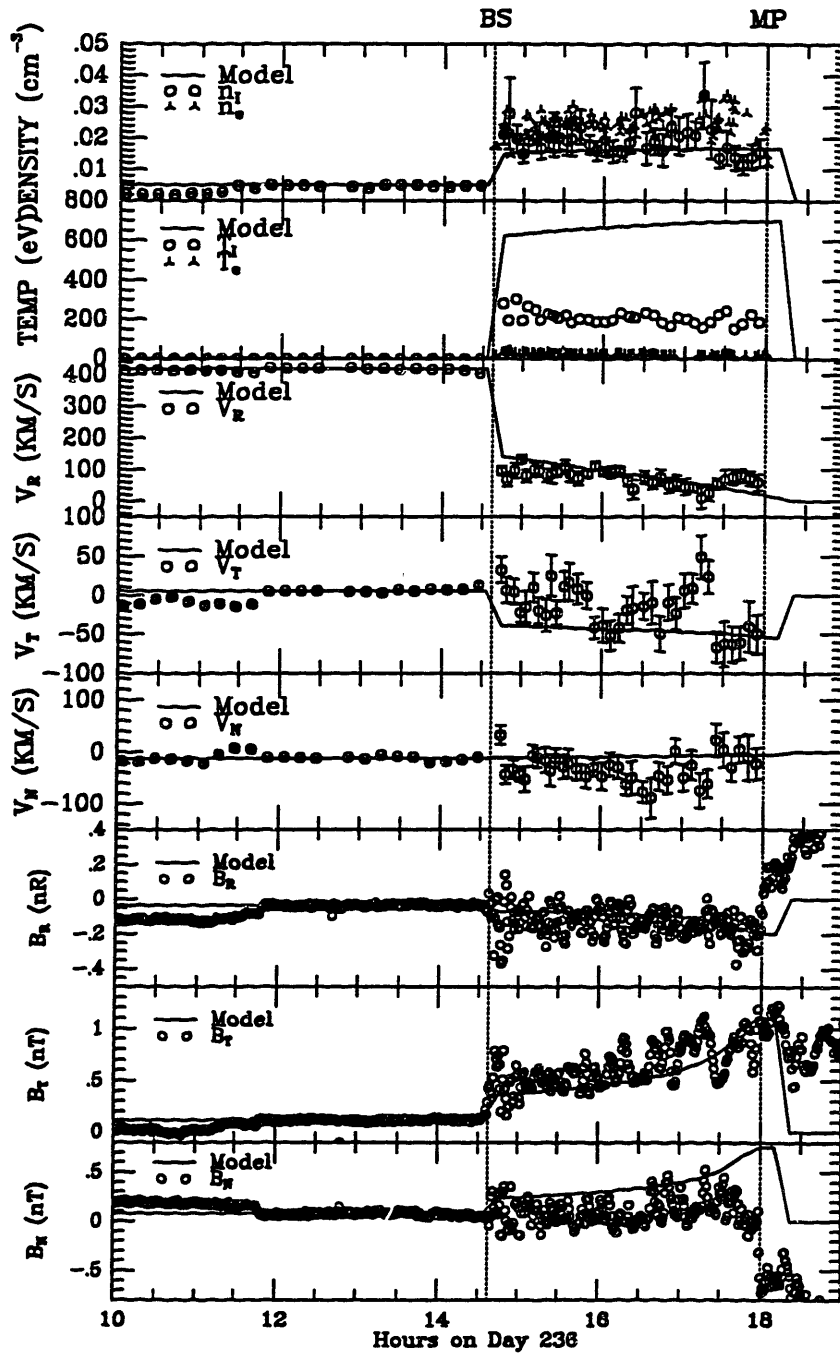


Fig. 3.1. A plot of plasma parameters and the magnetic field components in the solar wind and magnetosheath approaching Neptune. The vertical dotted lines show the bow shock and magnetopause locations and the solid lines show gasdynamic model results.

and the N axis completes a right-handed system, pointing northward. The solid lines are the results of the previously discussed gas dynamic model which take as its input the solar wind conditions and the observed location of the magnetopause. The model calculations were carried out by S. S. Stahara as part of the collaborative work presented in *Richardson et al.* [1993]. The vertical dotted lines show the locations of the magnetopause and bow shock crossings. Salient features are a gradual (and erratic) swing of the flow into the minus \hat{T} direction, a decrease in the radial velocity, and an increase in density as the magnetopause is approached. The ion "temperature" is a weighted average of the two Maxwellian components used to fit the spectra (as was extensively discussed in Chapter 1), and is about 200 eV in the dayside magnetosheath. The electrons are too cold to be detected in the solar wind, but are observed in the magnetosheath with densities comparable to the measured ion density and temperatures on the order of 20 eV.

A more intuitive picture of the plasma velocity flow is shown in Figure 3.2. The flow in the magnetosheath is shown by arrows projected onto the spacecraft trajectory in the (a) R-T and (b) R-N planes, with the magnitude of the flow indicated by the length of the arrows. The solar wind flow is relatively constant and primarily radial. At the bow shock (indicated by the dotted lines), the flow slows, shifts in direction, and becomes much less steady. The flow in the R-T plane rotates in the $-\hat{T}$ direction as Voyager approaches the magnetosphere, as expected since Voyager is in the $-\hat{T}$ direction from the subsolar point. Voyager is slightly below the Sun-Neptune line and the flow thus diverts southward around the planet.

The results of the gas dynamic model discussed in the previous section are superimposed on the Voyager data in Figure 3.1. The measurements in the solar wind and the location of the magnetopause are input parameters to the model so these fit the observations a priori. Another input parameter of the model is γ , the ratio of specific heats. This parameter determines the density jump at the shock (a more detailed and precise analysis of the bow shock was

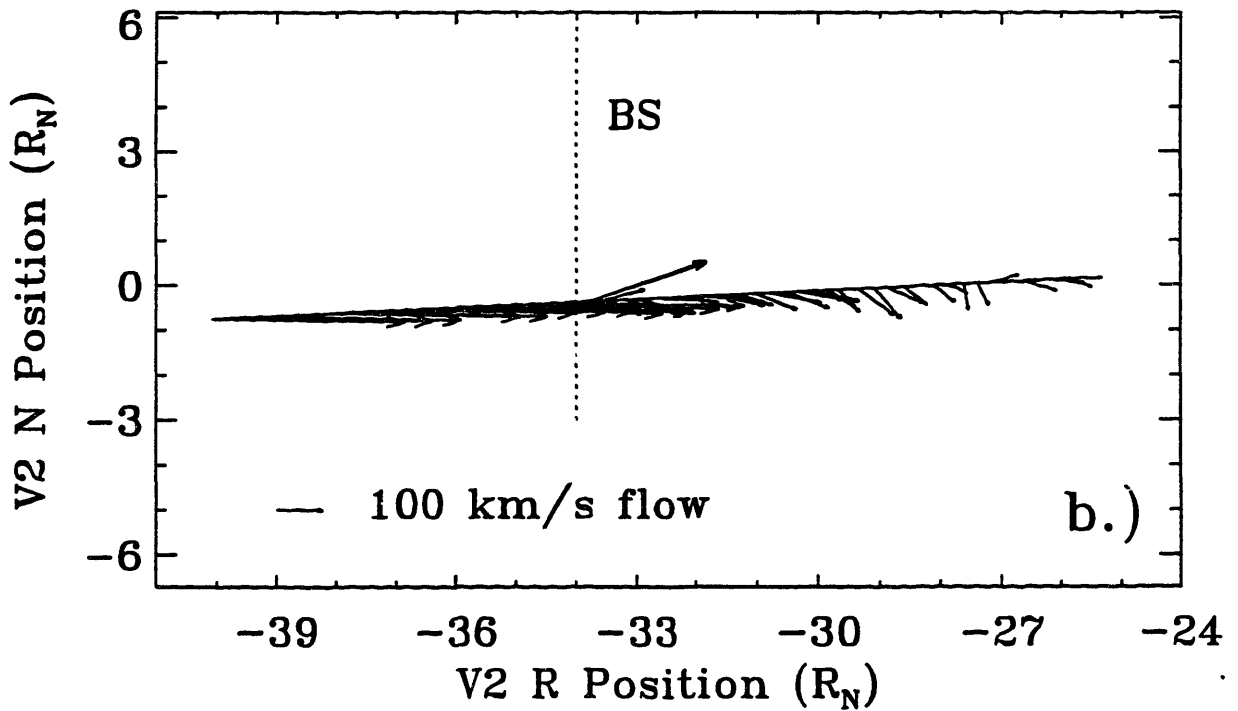
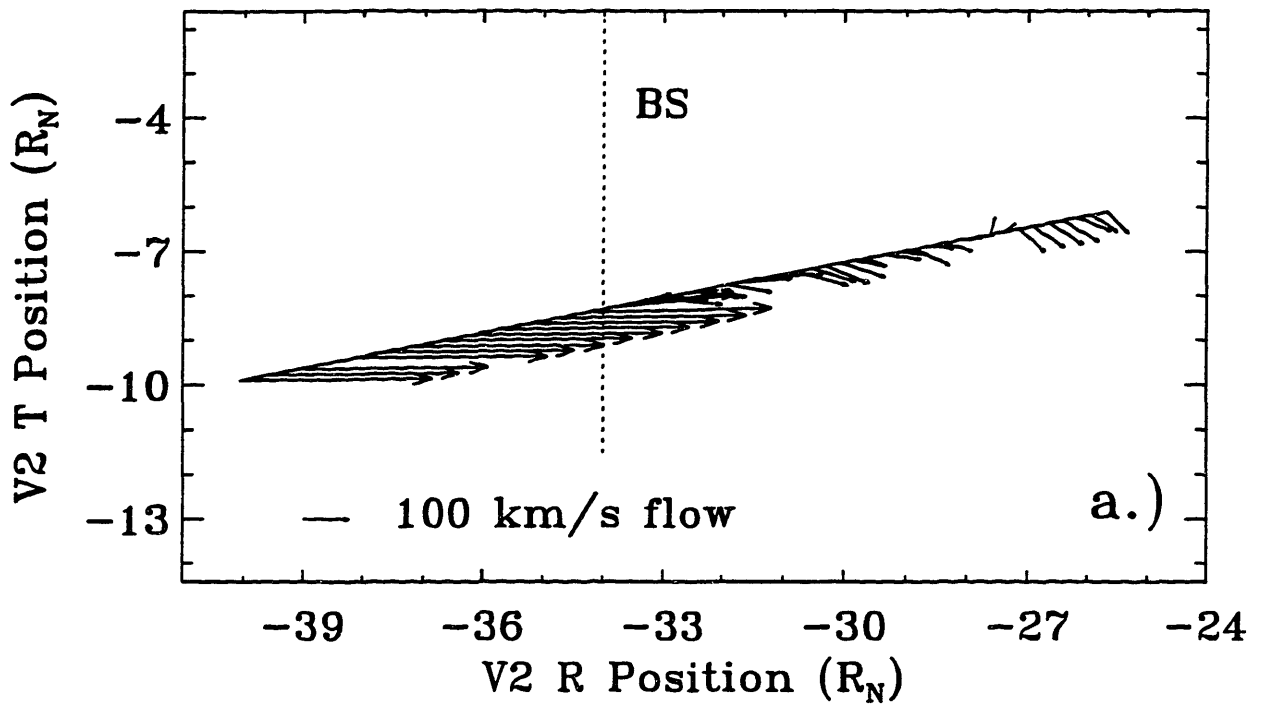


Fig. 3.2. A plot of the vector flow field in the solar wind and magnetosheath in the R-T and R-N planes. The length of the arrows is proportional to the magnitude of the velocity.

presented in Chapter 2) and the distance between the bow shock and magnetopause. Though it is not expected that this simplified model can provide results comparable to our MHD analysis described in the previous chapter, it is found that a value of 2 for γ (the rounded value of the MHD result) not only gives a good agreement at the shock but also gives a reasonable estimate for the size of the magnetosheath. The same value for γ was also successfully used to model the solar wind flow past Jupiter and Saturn [Stahara *et al.*, 1989].

Even though Voyager 2 crossed the magnetopause at very high magnetic latitudes due to Neptune's unusual magnetic configuration [Belcher *et al.*, 1989; Ness *et al.*, 1989; Szabo *et al.*, 1991; see also Chapters 1 and 4], the gas dynamic model and the measured data generally agree except near the shock where small scale, non-MHD features due to the shock are not expected to be reproduced by the model. The density and radial velocity in particular are fit quite well. The normal (N) and tangential (T) velocity components are qualitatively similar but the model predicts normal velocities which are less negative than those observed and tangential velocities which are generally more negative than those observed. The parameter with largest discrepancy between the model and the data is the plasma temperature. The temperature of both the ions and electrons decreases across the magnetosheath as the magnetopause is approached. In addition to being much too large, the model result has the opposite trend.

The magnetic field predicted by the model by convecting the solar wind magnetic field lines through the magnetosheath, also fits the data well on average. The gas dynamic simulation cannot, of course, fit the small scale magnetic field variations observed, but it does get the jumps at the bow shock correctly and also matches the trends in the magnetic field data except close to the magnetopause.

The gas dynamic model does a good job of predicting the plasma and magnetic field signatures observed by Voyager 2, at least as to the large scale variation [Richardson *et al.*, 1993]. And to a certain degree the discrepancies can be explained by our simplifying

assumptions, namely stationary boundaries (which are known not to be accurate from our bow shock and magnetopause analysis in Chapter 2 and 4, and is also noted by Cairns *et al.* [1991]) and an axially symmetric magnetosphere, with the obstacle size based on the magnetopause location observed by Voyager. The inclusion of a time dependent obstacle size and shape, however, is beyond the scope of the current treatment.

Focusing on the measured deviations from the model predictions near the magnetopause crossing in particular, a coherent picture can be surmised. The model calculations depend on the assumption of an unpenetrable magnetosphere at the magnetopause, and therefore, the model predicts a zero perpendicular flow. In contrast, our analysis of the magnetopause in Chapter 4 reveals it to be a rotational or rotational-like discontinuity with a significant plasma flow through it mostly in the radial direction. The observed differences between the gas dynamic model and actual measurements are consistent with this scenario. The ion and electron number densities drop the hour before the MP crossing and the radial, anti-sunward component of the plasma flow increases above the expected values suggesting plasma emptying into the mantle region. Since, the radial component of the plasma flow does not need to drop to zero in this scenario, it is reasonable that the plasma will not heat up as much as a non-penetrable MP, used for the gas dynamic model, would require. The other components of the plasma flow remain in good agreement with the model till the MP crossing. The magnetic field measurements show a discrepancy to a lesser degree near the MP, which is also reasonable since at a rotational discontinuity the normal magnetic field does not need to vanish. In summary, the open magnetosphere model observed at the inbound Neptunian MP gives a good resolution of the discrepancies between the gas dynamic model predictions and the measured data.

CHAPTER 4

THE SUBSOLAR MAGNETOPAUSE AND CUSP

4.1 Introduction

We continue to follow the passage of the solar wind plasma as it interacts with the magnetosphere of Neptune. After the subsonic regions of the magnetosheath, the plasma impinges on the boundary of the magnetosphere. As it was mentioned several times before, because of the particular phasing of the Neptunian day and the fact that the axis of the main magnetic field of the planet is tilted by about 47° with respect to its rotation axis [*Ness et al.*, 1989; *Connerney et al.*, 1991], Voyager 2 appears to have serendipitously encountered the distant polar cusp region of the magnetosphere immediately after crossing the inbound magnetopause (MP) at 18.00 hr on August 24, 1989 [*Belcher et al.*, 1989] (for a description of the different magnetospheric regions see Chapter 1). The preliminary study of this region by *Szabo et al.* [1991] demonstrates that the inbound MP is more consistent with the properties of a MHD rotational discontinuity than that of a tangential discontinuity. This study also suggests that the magnetosheath plasma can enter the upper regions of the polar magnetosphere through the MP, forming a boundary layer showing some of the characteristics of a mantle region. In this chapter, we are going to employ a new MHD fitting technique specifically developed for rotational discontinuities (the technique is described in Section 2), and also the more traditional magnetic minimum variance analysis (described in Section 3) to further analyze the nature of the MP. The results of these methods are presented in Section 4, where also some of the global versus local properties of the MP are presented. These properties suggest the observation of a possible pressure pulse or reconnection bulge on the surface of the MP. Section 5 discusses the observations in the distant polar magnetospheric boundary regions. Evidence is presented for

the existence of regions with characteristics of the Earth's entry layer and plasma mantle.

4.2 The MHD Fitting Technique

Rotational discontinuities (RD-s) are solutions of the MHD jump conditions described in Chapter 2, Section 1.2 (the complete set of MHD jump condition equations are listed in equations (2.1) - (2.6)) with the special condition that the plasma density does not change across the discontinuity. That is, using the notation developed in Chapter 2:

$$\Delta[\rho] = 0 \quad (4.1)$$

where $\Delta[]$ refers to change across the discontinuity. This condition, when substituted, simplifies the jump condition equations to the following form:

$$\Delta[V_n] = 0 \quad (4.2)$$

$$\Delta[B_n] = 0 \quad (4.3)$$

$$\Delta[A_t] = \Delta \left[V_t - \frac{B_t}{\sqrt{\mu_0 \rho}} \right] = 0 \quad (4.4)$$

$$\Delta[T] = 0 \quad (4.5)$$

$$\Delta[|B|] = 0 \quad (4.6)$$

During the above performed substitution, we also gain an explicit expression for the bulk speed of the discontinuity, V_{RD} , even though it does not appear in the final jump condition equations.

The thus obtained formula for V_{RD} is:

$$V_{RD} = V_n - \frac{B_n}{\sqrt{\mu_0 \rho}} \quad (4.7)$$

where in all of the above formulae ρ is the mass density, T the plasma temperature, and V and B are the plasma bulk velocity and the magnetic field, respectively, as measured by the

spacecraft. The subscripts n and t refer to the normal and tangential components of the above quantities. Note that equation (4.4) is a two dimensional vector equation. Also note that equations (4.2) - (4.6) have been expressed as conservation equations. That is V_n , B_n , A_t (a quantity defined in equation (4.4)), T , and $|B|$ are all conserved across a RD.

Even though rotational discontinuities are a valid subset of the solutions of the MHD jump conditions, advanced fitting techniques (i.e. *Viñas and Scudder [1986]* or *Szabo [1993]* described in Chapter 2) break down for this special class of solutions. The reason for this problem is that both methods, as the very first step, express the shock bulk velocity from the mass continuity equation (equation (2.1)) as:

$$V_S = \frac{\Delta[\rho V]}{\Delta[\rho]} \cdot \hat{n} \quad (4.8)$$

where \hat{n} is the shock unit normal. In the case of RD-s, the denominator in the above equation vanishes leading to a singularity, which then plagues the rest of the method. In order to get around this singularity, we have to slightly alter the order of the process of solution described in Chapter 2. All of the required modifications are described in this section.

(I) When we have obtained the simplified set of jump conditions for the RD (equations (4.2) - (4.6)), we have also obtained an expression for the RD bulk speed in equation (4.7). Therefore, there will be no need for the singularity result in equation (4.8). Also, note that only equations (4.2) - (4.4) are dependent on the RD surface normal direction. Therefore, in order to determine the most likely unit normal \hat{n} , we have to solve a system of only 4 equations, namely equations (4.1) - (4.4) where equation (4.4) is two dimensional.

At this stage, we have to point out that in the ideal case of a completely pure rotational discontinuity data set, free of any source of noise, the above four equations reduce to a single one. The reason is that if $\Delta[V_n]$ and $\Delta[B_n]$ are truly equal to zero, then $\Delta[V_t] = \Delta[V]$ and

$\Delta[B_t] = \Delta[B]$, that is, the vector equation (4.4) becomes independent of the RD surface normal \hat{n} . Moreover, if $\Delta[V_n] = 0$ then equation (4.4) would necessitate that $\Delta[B_n] = 0$, too. Therefore, equations (4.2) and (4.3) would not be linearly independent, and only one of the two equations could be used in our calculations. One equation, however, is not sufficient to determine a unique RD normal, rather, it yields a solution plane in which the unit normal has to lie.

In the case of real observations, however, the data always has some fluctuation around the idealized values. Then, for each individual data pair across the discontinuity, the best possible fit for the RD normal will be a slightly altered plane. For each different data pair, the alteration will be different, and therefore, the best fit RD normal planes will not completely overlap. When we will perform the least squares fitting, we are looking for, in some sense, the overlap or intersection between these planes. If the noise fluctuations are truly randomly distributed around the exact MHD values of the magnetofluid parameters, then the intersections of the solution planes will be close to the exact solution, and therefore, we would arrive at a unique RD surface normal direction. Of course, this is only a second order effect, and all of the noise fluctuations will produce only small deviations in the RD surface normal solution plane. Therefore, even in the case of observational data, we would expect the confidence regions of the best fit normal to be elongated in the direction of a preferred plane. Also, this method to obtain a unique direction for the RD surface normal from the plane of possible solutions is highly dependent on the normal distribution of the measured fluctuations around the pure MHD values. Therefore, the fitted best normal direction, within the best fit plane, should be treated with an amount of scepticism.

In equations (4.2) - (4.4), it is assumed that the plasma mass density is constant. However, the actual measurements always show a certain amount of fluctuation around the constant value. To find this constant plasma mass density, we take the error weighted average of the measured values. In the above system of equations, for the plasma velocity and magnetic field

strength we use the observed quantities, leaving the unit RD normal as the only unknown. We express the unit RD normal in spherical coordinates (θ, ϕ) just as it was done in Chapter 2, namely the components of the unit normal are given by $\hat{n}_x = \cos \theta$, $\hat{n}_y = \cos \phi \sin \theta$, and $\hat{n}_z = \sin \phi \sin \theta$. This system of equations then can be solved by the iterative non-linear least squares fit technique of the Levenberg-Marquardt method [Press *et al.*, 1986], also employed in Chapter 2.

If we represent again the individual equations of the RD jump conditions by $Y_j(\mathbf{x}; \mathbf{p}) = 0$, where $\mathbf{x} = (\rho_1, V_1, B_1, T_1, \rho_2, V_2, B_2, T_2)$ are the observed magnetofluid parameters on both sides (sides 1 and 2) of the RD and $\mathbf{p} = (\theta, \phi)$ are the unknown parameters of the RD normal, then we can express $\chi^2(\theta, \phi)$, the norm of the residuals which is minimized by the best fit solution, as

$$\chi^2(\theta, \phi) = \sum_{i=1}^N \sum_{j=1}^K \frac{[Y_j(\mathbf{X}_i; \mathbf{p}) - y_j]^2}{\sigma_{ij}^2} \quad (4.9)$$

where N are the number of data pairs \mathbf{x} across the discontinuity, K is the number of equations in the system, namely 4, and y_j is the theoretically expected value of the model equation Y_j , which, in our case, is zero. Finally, σ_{ij} is the standard deviation in the j -th model equation when the i -th observed data pair is used to calculate the value of the model equation. The standard deviations are propagated from the standard errors in the observed magnetofluid quantities. As it was discussed in Chapter 2, σ_{ij}^2 serves to make χ^2 dimensionless and also acts as a weighting factor for the individual measured data pairs.

Again, two different methods are used to construct the data pairs \mathbf{x} . In one method, each data point on one side of the RD is paired with one data point on the other side, symmetrically moving away from the discontinuity. In the other method, all data points on one side are paired with all data points on the other side. The advantages and disadvantages of the two

methods are discussed in Chapter 2, Section 1.2.

Our method locates the best possible fit parameters θ and ϕ by varying them and observing the effects in the value of χ^2 . When the χ^2 function reaches a minimum, we have a possible solution for our system of equations. If we map out the thus obtained χ^2 function over the locus of all possible solutions (a hemisphere where $0 \leq \theta \leq \pi/2$, $0 \leq \phi \leq 2\pi$), we can find all of the local minima of the function and therefore investigate all likely solutions, removing the question of uniqueness. Just as in the case of shocks, each possible solution has to be investigated separately to see if it represents a valid RD [i.e. there is plasma flow across the surface, and there is a non-vanishing magnetic field normal component] and to see that the calculated asymptotic magnetofluid parameters (which are the plasma and magnetic field parameters necessitated by the chosen RD surface normal and MHD theory) are in good agreement with the observations. The confidence regions of the solution are established as described in Chapter 2, Section 1.4.

(II) Once the best RD normal \hat{n} is established, equation (4.7) is used with the observed data to calculate the RD bulk speed V_{RD} . In the case of RD-s, V_{RD} can be expressed strictly in terms of conserved quantities, namely V_n , B_n , and ρ . Therefore, as opposed to the case of the calculations for a general shock, described in Chapter 2, where differences across the shock have to be formed to calculate the RD bulk speed, we only have to rely on values obtained at individual points of measurement and not on values stemming from data pairs across the RD. At this point, we could employ a one dimensional version of the non-linear least squares technique employed above to obtain the best fit value of V_{RD} ; however, V_{RD} is linear in the model equation, and therefore a unique analytical solution is possible. The χ^2 function to be minimized can be written as:

$$\chi^2(V_{RD}) = \sum_{i=1}^M \frac{\left[V_n - \frac{B_n}{\sqrt{\mu_0 \rho}} - V_{RD} \right]^2}{\sigma_i^2} \quad (4.10)$$

where V_{RD} are the trial values of the RD bulk speed, M is the total number of data points on both sides of the RD, and σ_i is the standard deviation in the calculated bulk speed at the i -th point of measurement with the standard errors propagated from the individual magnetofluid parameters. Just as in the previous cases, σ_i acts as a weighting factor for each data point. Setting the first derivative of χ^2 with respect to V_{RD} equal to zero and checking the second derivatives provides the analytical solution for the best fit V_{RD} :

$$V_{RD} = \frac{\sum_{i=1}^M \frac{V_n - B_n/\sqrt{\mu_0 \rho}}{\sigma_i^2}}{\sum_{i=1}^M \frac{1}{\sigma_i^2}} \quad (4.11)$$

This solution is unique because the second derivative of χ^2 with respect to V_{RD}

$$\frac{\partial^2(\chi^2)}{\partial V_{RD}^2} = 2 \sum_{i=1}^M \frac{1}{\sigma_i^2} \quad (4.12)$$

which is clearly always positive.

(III) Once the RD normal and bulk speed are determined, we can proceed to find the conservation constants defined in equations (4.2) - (4.6). We can write these equations in a more intuitive form:

$$V_n = \mathbf{V} \cdot \hat{\mathbf{n}} \quad (4.13)$$

$$B_n = \mathbf{B} \cdot \hat{\mathbf{n}} \quad (4.14)$$

$$A_t = V_t - \frac{B_t}{\sqrt{\mu_0 \rho}} \quad (4.15)$$

$$T = T \quad (4.16)$$

$$B_{mag} = |B| \quad (4.17)$$

where in all of the equations the left side is a conserved quantity and the right side is the formula to obtain them from the measured magnetofluid parameters. Of course the mass density ρ is also conserved for a RD, but its value has already been determined above. All conservation constants are computed from individual measurement points and not from data pairs taken across the discontinuity (as was also required for the determination of the RD normal). Therefore, when these quantities are calculated, the summation will run over all of the data points on both sides of the RD, as it was done for the determination of the RD bulk speed. Inspection of these equations also reveal that they are all linear and independent. Therefore, the same analytical method can be used to obtain the best fit solutions as was demonstrated for the case of the RD bulk speed. The solutions obtained thereby are:

$$V_n = \frac{\sum_{i=1}^M \frac{V_{n_i}}{\sigma_i^2}}{\sum_{i=1}^M \frac{1}{\sigma_i^2}} \quad (4.18)$$

$$B_n = \frac{\sum_{i=1}^M \frac{B_{n_i}}{\sigma_i^2}}{\sum_{i=1}^M \frac{1}{\sigma_i^2}} \quad (4.19)$$

$$A_t = \frac{\sum_{i=1}^M \frac{V_{t_i} - B_{t_i}/\sqrt{\mu_0 \rho}}{\sigma_i^2}}{\sum_{i=1}^M \frac{1}{\sigma_i^2}} \quad (4.20)$$

$$T = \frac{\sum_{i=1}^M \frac{T_i}{\sigma_i^2}}{\sum_{i=1}^M \frac{1}{\sigma_i^2}} \quad (4.21)$$

$$B_{\text{mag}} = \sum_{i=1}^M \frac{|B_i|}{\sigma_i^2} / \sum_{i=1}^M \frac{1}{\sigma_i^2} \quad (4.22)$$

where the subscript i on the magnetofluid parameters indicate the individual measurements over which the summation is taken. Again, the uniqueness of these solutions is easily demonstrable.

(IV) Finally the self-consistent asymptotic magnetofluid states can be determined. The asymptotic magnetofluid states are the values of the plasma and magnetic field data predicted by the MHD theory employed for the case of the determined discontinuity normal and bulk speed. If the MHD theory is adequate to describe the observed phenomenon and the fitted parameters are correct, then the measured magnetofluid parameters should fluctuate around these asymptotic states. If we find that there is no good correlation between the asymptotic states and the measured parameters, then we have either picked the wrong minima in our solution parameter space, or the employed MHD theory is not sufficient to describe the observed phenomenon. With regards to the ambiguity of the RD surface normal direction discussed earlier, the asymptotic states will help us to see how well we have done in selecting the proper direction for the RD surface normal.

At this point, we have to significantly deviate from the method developed for general MHD shocks. In the case of MHD shocks, a set of equations was found which expressed all of the asymptotic states in terms of the plasma mass density on either side of the shock. That method cannot be used for RD-s because the mass density now is a conserved quantity and not an asymptotic state; that is, it would lead to singularity solutions as was mentioned in Chapter 2. We will demonstrate that a set of equations expressing the asymptotic states depending on only a single parameter is still possible. However, this parameter now will be the magnitude of the solar wind velocity. Though some other parameters could have been chosen as the single fitting parameter (e.g. any component of the velocity), our selection has the advantage that it is

independent from the selection of the coordinate system used to express the magnetofluid parameters. Our job will be then to express the components of the plasma velocity and magnetic field, \mathbf{V} and \mathbf{B} in terms of the magnitude of plasma velocity $|\mathbf{V}|$.

To determine the components of the plasma bulk velocity in terms of the conserved quantities and $|\mathbf{V}|$ we use equations (4.13) and the magnitude of the 2-dimensional vector equation (4.15), to eliminate coordinate system dependences, as well as the definition of $|\mathbf{V}|$

$$|\mathbf{V}| = V_x^2 + V_y^2 + V_z^2 \quad (4.23)$$

If we define the following quantities:

$$\alpha = \frac{\hat{n}_z A_{t_x} - \hat{n}_x A_{t_z}}{\hat{n}_z A_{t_y} - \hat{n}_y A_{t_z}} \quad (4.24)$$

$$\beta(|\mathbf{V}|) = \frac{\frac{\hat{n}_z}{2} \left[|\mathbf{V}|^2 + |\mathbf{A}_t|^2 - \frac{|\mathbf{B}|^2}{\mu_0 \rho} \right] - V_x A_{t_z}}{\hat{n}_z A_{t_y} - \hat{n}_y A_{t_z}} \quad (4.25)$$

$$\Theta = \hat{n}_z^2 (1 + \alpha^2) + (\hat{n}_y \alpha - \hat{n}_x)^2 \quad (4.26)$$

$$Y(|\mathbf{V}|) = 2 \left[(\hat{n}_y \alpha - \hat{n}_x) (V_x - \hat{n}_y \beta) - \hat{n}_z^2 \alpha \beta \right] \quad (4.27)$$

$$\Xi(|\mathbf{V}|) = \hat{n}_z^2 \beta^2 - \hat{n}_z^2 |\mathbf{V}|^2 + (V_x - \hat{n}_y \beta)^2 \quad (4.28)$$

where the subscripts x , y , and z refer to the components of the quantity in an arbitrary Cartesian system. Then the components of the plasma bulk velocity can be expressed as

$$V_x = \frac{-Y(|\mathbf{V}|) \pm \sqrt{Y(|\mathbf{V}|)^2 - 4\Theta\Xi(|\mathbf{V}|)}}{2\Theta} \quad (4.29)$$

$$V_y = \beta(|\mathbf{V}|) - \alpha V_x \quad (4.30)$$

$$V_z = \left[\frac{\hat{n}_y}{\hat{n}_z} \alpha - \frac{\hat{n}_x}{\hat{n}_z} \right] V_x + \frac{V_x}{\hat{n}_z} - \frac{\hat{n}_y}{\hat{n}_z} \beta(|\mathbf{V}|) \quad (4.31)$$

where the only unknown is $|\mathbf{V}|$. Notice that we have two possible set of solutions due to the quadratic nature of the system. Both solutions are valid and the resultant asymptotic magnetic fields will determine which set will be used for the comparison with the actual measurements.

Similarly, we determine the asymptotic value of the components of the magnetic field. We still have the conservation equations (4.14) and (4.16) unused and one component of the 2-dimensional equation (4.15). To eliminate coordinate system introduced singularities, we use the sum of all components of equation (4.15) which is linearly independent from the magnitude of this equation used previously. Again introducing a number of helpful quantities to keep the equations readable:

$$\gamma(|\mathbf{V}|) = (V_x + V_y + V_z - A_x - A_y - A_z)\sqrt{\mu_0\rho} \quad (4.32)$$

where V_x , V_y , and V_z are to be substituted from equations (4.29) - (4.31); and

$$\eta(|\mathbf{V}|) = \frac{\hat{n}_z\gamma - B_n}{\hat{n}_z - \hat{n}_y} \quad (4.33)$$

$$\tau = \frac{\hat{n}_x - \hat{n}_z}{\hat{n}_z - \hat{n}_y} \quad (4.34)$$

$$\xi(|\mathbf{V}|) = \frac{B_n - \hat{n}_y\gamma}{\hat{n}_z - \hat{n}_y} \quad (4.35)$$

$$\zeta = \frac{\hat{n}_x - \hat{n}_y}{\hat{n}_z - \hat{n}_y} \quad (4.36)$$

$$\Gamma(|\mathbf{V}|) = 1 + \tau^2 + \zeta^2 \quad (4.37)$$

$$\Lambda(|\mathbf{V}|) = 2(\eta\tau - \xi\zeta) \quad (4.38)$$

$$\Omega(|\mathbf{V}|) = \eta^2 + \xi^2 - |\mathbf{B}|^2 \quad (4.39)$$

the components of the asymptotic magnetic field strength are given by

$$B_x = \frac{-\Lambda(|V|) \pm \sqrt{\Lambda(|V|)^2 - 4\Gamma(|V|)\Omega(|V|)}}{2\Gamma(|V|)} \quad (4.40)$$

$$B_y = \eta(|V|) + \tau B_x \quad (4.41)$$

$$B_z = \xi(|V|) - \zeta B_x \quad (4.42)$$

where again the only unknown is $|V|$. The magnetic field equations introduced yet another quadratic split increasing the number of possible solutions to four. However, it is important to point out that in practice, all of these solutions have a limited range of validity beyond which the solutions turn complex which has no physical meaning. Within their range of validity, all the possible solutions have to be compared with the observations. Most importantly, however, at this point we have a set of equations expressing the components of the plasma bulk velocity and magnetic field strength in terms of the conservation constants and the magnitude of the plasma bulk velocity. That is, if we can solve for the best fit $|V|$ on both sides of the RD, we immediately gain the rest of the magnetofluid variables.

To find the asymptotic values of the magnitude of the plasma bulk velocity both upstream and downstream of the RD, we again apply the non-linear least squares technique described above. Our model functions are the differences between the measurements and the theoretical predictions of equations (4.29)-(4.31) and (4.40)-(4.42). The definition of $|V|$ is already included in these equations. Of course, we expect all 6 model equations to evaluate to zero; i.e. $Y_j(x_i; \mathbf{p}) = 0$. Here the input variables are $x_i = (V, B)_i$ measured on either the upstream or downstream side of the RD. This time, we have only one fit parameter, namely $|V|$ which for the sake of generality is represented by the one element vector \mathbf{p} . The best fit is determined by evaluating the $\chi^2(|V|)$ function summed over all of the model equations and data points on one side of the discontinuity weighted by the individually propagated standard deviations as it was done in equation (4.10). The minima of the $\chi^2(|V|)$ function represent the solutions of the fit. Uniqueness of the solution can be ascertained by plotting χ^2 as a function of $|V|$ and

individually inspecting all local minima. The determination of the various confidence regions around the solution is again discussed in Chapter 2, Section 1.4.

Once the asymptotic value of $|V|$ is known, equations (4.29)-(4.31) and (4.40)-(4.42) are used to find the asymptotic values of the components of the plasma bulk velocity and magnetic field. Finally, the goodness of our fit can be checked by plotting these asymptotic states along with the conserved plasma mass density and temperatures against their measured equivalents. This technique is going to be employed in Section 4 to analyze the Neptunian inbound magnetopause.

4.3. The Magnetic Variance Technique

Most often for spacecraft observations, and specifically in the case of Voyager 2 at Neptune, magnetic field data is available at a much higher time resolutions than the plasma measurements. Therefore, several techniques have been developed in the past to analyze discontinuities relying only on magnetic field measurements. The most often used technique is the variance analysis of *Sonnerup and Cahill* [1967]. In this section, we give a short review of this technique with some more modern additions.

Since the magnetic field strength B is divergence free, its normal component must be continuous across any infinitely thin interface, as was noted in the MHD jump condition equation (2.2). In practice we may apply this condition to a current layer of finite thickness provided that its radius of curvature and the characteristic length for lateral changes of its structure are much larger than its thickness. Thus we may write

$$\mathbf{B}_1 \cdot \hat{\mathbf{n}} = \mathbf{B}_{i_n} \cdot \hat{\mathbf{n}} = \mathbf{B}_2 \cdot \hat{\mathbf{n}} \quad (4.43)$$

where $\hat{\mathbf{n}}$ is the unit normal vector to the discontinuity, \mathbf{B}_1 and \mathbf{B}_2 denote the field vectors on the opposite sides of the discontinuity but adjacent to it, and \mathbf{B}_{i_n} is a field vector within the

current layer. From these two equations, together with the normalization condition $|\hat{n}|^2 = 1$, the normal vector can be calculated. In fact an explicit expression for \hat{n} can be obtained by inspection. The equations (4.43) simply state that the three vectors \mathbf{B}_1 , \mathbf{B}_2 , and \mathbf{B}_{in} have a common component perpendicular to the discontinuity current layer. Therefore the two vectors $(\mathbf{B}_2 - \mathbf{B}_1)$ and $(\mathbf{B}_2 - \mathbf{B}_{in})$ are tangential to the current layer, and the normal vector can be obtained as their normalized cross product:

$$\hat{n} = \pm \frac{(\mathbf{B}_2 - \mathbf{B}_1) \times (\mathbf{B}_2 - \mathbf{B}_{in})}{|(\mathbf{B}_2 - \mathbf{B}_1) \times (\mathbf{B}_2 - \mathbf{B}_{in})|} \quad (4.44)$$

The sign of the above equation can be conveniently selected to point the discontinuity normal away from the planet.

We, therefore, conclude that two accurate magnetic field vector measurements on opposite sides of the discontinuity and one in its interior in principle suffice to determine the normal vector provided that all three measurements are simultaneous. This latter condition is not met when the measurements are taken from a single spacecraft penetrating the discontinuity. But the method can still be used provided that changes in the current layer structure and attitude are negligible during the time of crossing.

The Voyager 2 MAG experiment provided not three accurate field measurements at the inbound magnetopause crossing but rather dozens of relatively inaccurate ones. It is possible, of course, to lump these measurements into three groups \mathbf{B}_1 , \mathbf{B}_2 , and \mathbf{B}_{in} then average and use equation (4.44). However, a more reliable method is the following:

The normal vector is chosen in such a fashion that the standard deviation of the individual products $\mathbf{B}_i \cdot \hat{n}$ from the average value $\bar{\mathbf{B}} \cdot \hat{n}$ is a minimum. Here \mathbf{B}_i represents an individual field measurement, and $\bar{\mathbf{B}}$ is the average of all N magnetic field measurements used in the calculation. In other words

$$\bar{\mathbf{B}} = \frac{1}{N} \sum_{i=1}^N \mathbf{B}_i \quad (4.45)$$

and the normal vector is obtained by the minimization of

$$\chi^2 = \frac{1}{N} \sum_{i=1}^N (\mathbf{B}_i \cdot \hat{\mathbf{n}} - \bar{\mathbf{B}} \cdot \hat{\mathbf{n}})^2 \quad (4.46)$$

This second method represents an improvement over the first also because it allows for the fact that the measured normal magnetic field component is not constant during the crossing of the discontinuity layer because of various non-stationary effects and the digital nature of the data. However, in the least-mean-square sense, the continuity of this component across the layer is satisfied in the best possible way.

As it is noted by *Sonnerup and Cahill [1967]*, the minimization of equation (4.46) is equivalent to finding the smallest eigenvalue of the covariant matrix

$$M_{ij} = \overline{B_i B_j} - \bar{B}_i \bar{B}_j \quad i, j = 1, 2, 3 \quad (4.47)$$

where B_i and B_j are the Cartesian components of an individual measured magnetic field vector and the overhead bar denotes an average over all of the measurements used in the calculation. The normal vector is the eigenvector of matrix (4.47) corresponding to its smallest eigenvalue. Equivalently, the normal vector coincides with the shortest principal axis of the variance ellipsoid defined by the quadratic form (4.46).

There is, however, a major difficulty associated with this method for the determination of the normal vector when

$$(\mathbf{B}_2 - \mathbf{B}_1) \times (\mathbf{B}_2 - \mathbf{B}_{in}) = 0 \quad (4.48)$$

i.e. when the two nonzero vectors $(\mathbf{B}_2 - \mathbf{B}_1)$ and $(\mathbf{B}_2 - \mathbf{B}_{in})$ are co-linear. In that case any

vector perpendicular to $(\mathbf{B}_2 - \mathbf{B}_1)$ satisfies equation (4.43). In the minimum variance method this problem appears in the form of the two smallest eigenvalues being equal. Then the variance ellipsoid degenerates to an ellipsoid of revolution. It can be shown that this situation arises if the current vectors in the layer are everywhere perpendicular to $(\mathbf{B}_2 - \mathbf{B}_1)$, i.e., if the current is unidirectional. When the two smallest eigenvalues of $M_{\alpha\beta}$ are almost equal, the determination of $\hat{\mathbf{n}}$ becomes inaccurate. *Lepping and Behannon [1980]* show that when $\lambda_2/\lambda_3 < 1.8$ (where the subscripts 1, 2, and 3 on the eigenvalues λ refer to the maximum, intermediate, and minimum values, respectively) the RD normal is too poorly determined to be useful. *Lepping and Behannon [1980]* also obtain an empirical expression for the magnitude of the error $|\Delta B_z|$ in an estimated discontinuity normal component, relative to the total field across the discontinuity. This formula resulted from studies of the relation between precisely known values of the error and the minimum variance eigenvalues λ , rotation angle in the discontinuity plane ω , and the magnitude of the normal component $B \cos \beta$ relative to the total field B . The formula is

$$|\Delta B_z| = \frac{3}{4} B \sin \beta \Lambda^{(3.60+2.44 \log \Lambda)} \left\{ \exp [(120^\circ - \omega)/120^\circ]^3 \right\} \quad (4.49)$$

where $\Lambda = \lambda_3(1/\lambda_1 + 1/\lambda_2)$.

This method of minimum variance along with the above described error estimation will be extensively used in the next section of this chapter to analyze the nature of the Neptunian magnetopause discontinuity.

4.4 Physical and Geometrical Properties of the MP

The observations of Voyager 2 around the inbound MP and cusp region are presented on Figures 4.1 - 4.3. Figure 4.1 shows the plasma number density versus time on the lowest

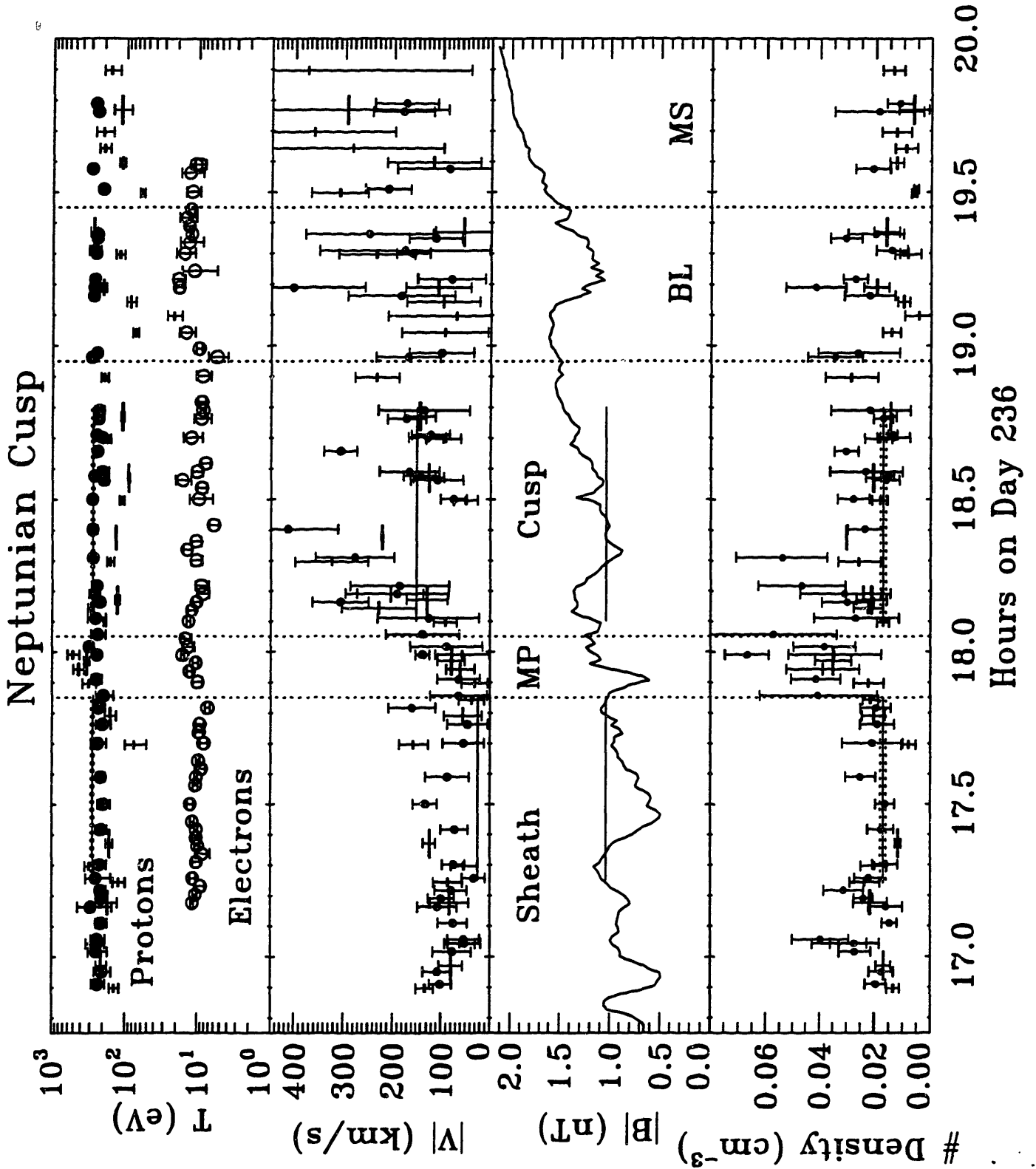


Fig. 4.1. Voyager 2 observations of the MP and cusp. Measurements shown are the proton number density, magnetic field magnitude, plasma bulk velocity magnitude, and the proton and electron temperatures. Superimposed are the fit results of the MHD rotational discontinuity fit represented by horizontal lines.

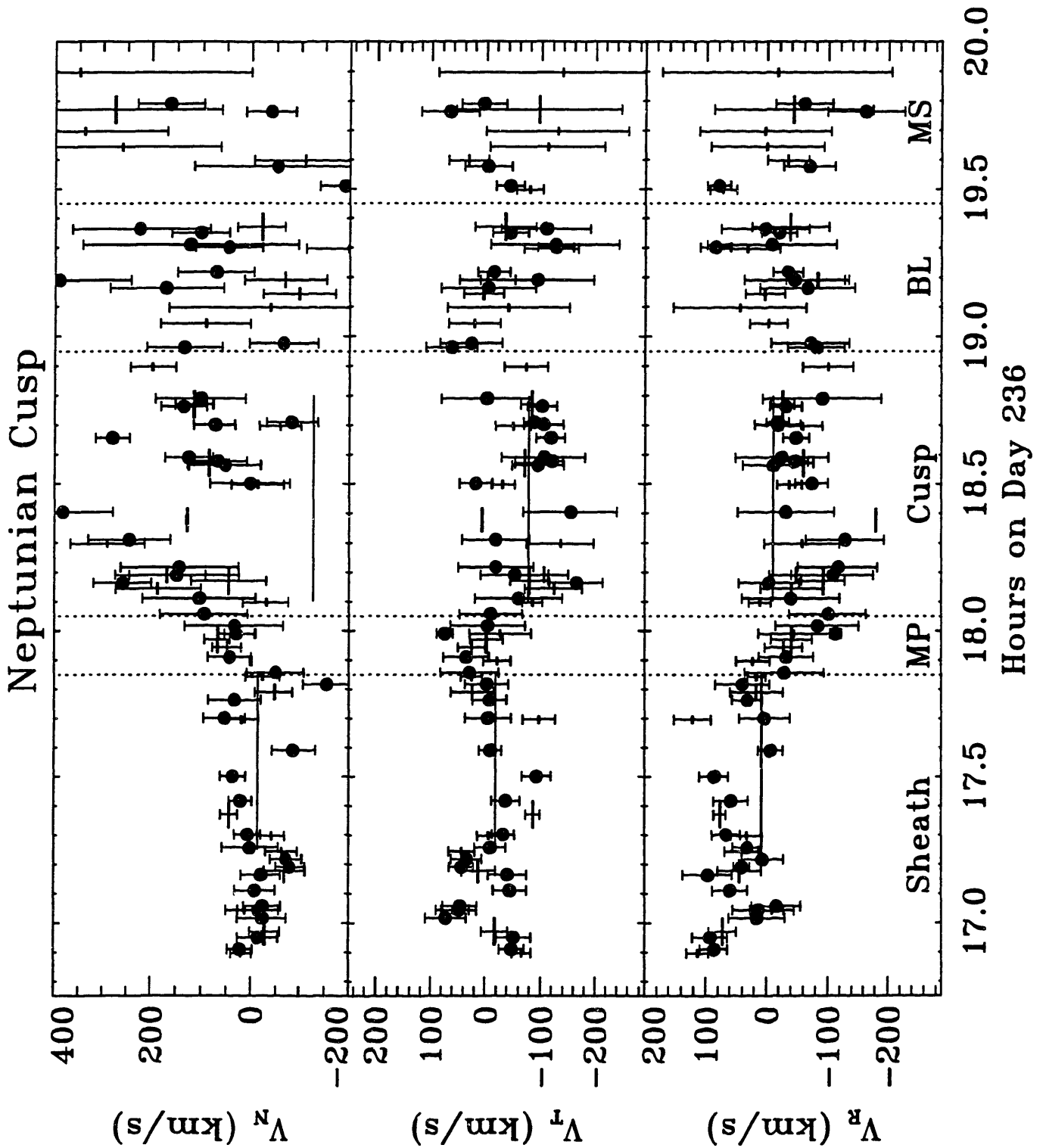


Fig. 4.2. Voyager 2 observations of the MP and cusp. Measurements shown are the plasma bulk velocity components in Neptune centered RTN coordinate system. The solid dots represent single L mode fits, whereas the small horizontal bars stand for fits obtained from averaged L mode spectra. The length of the horizontal bars show the length of the averaging intervals.

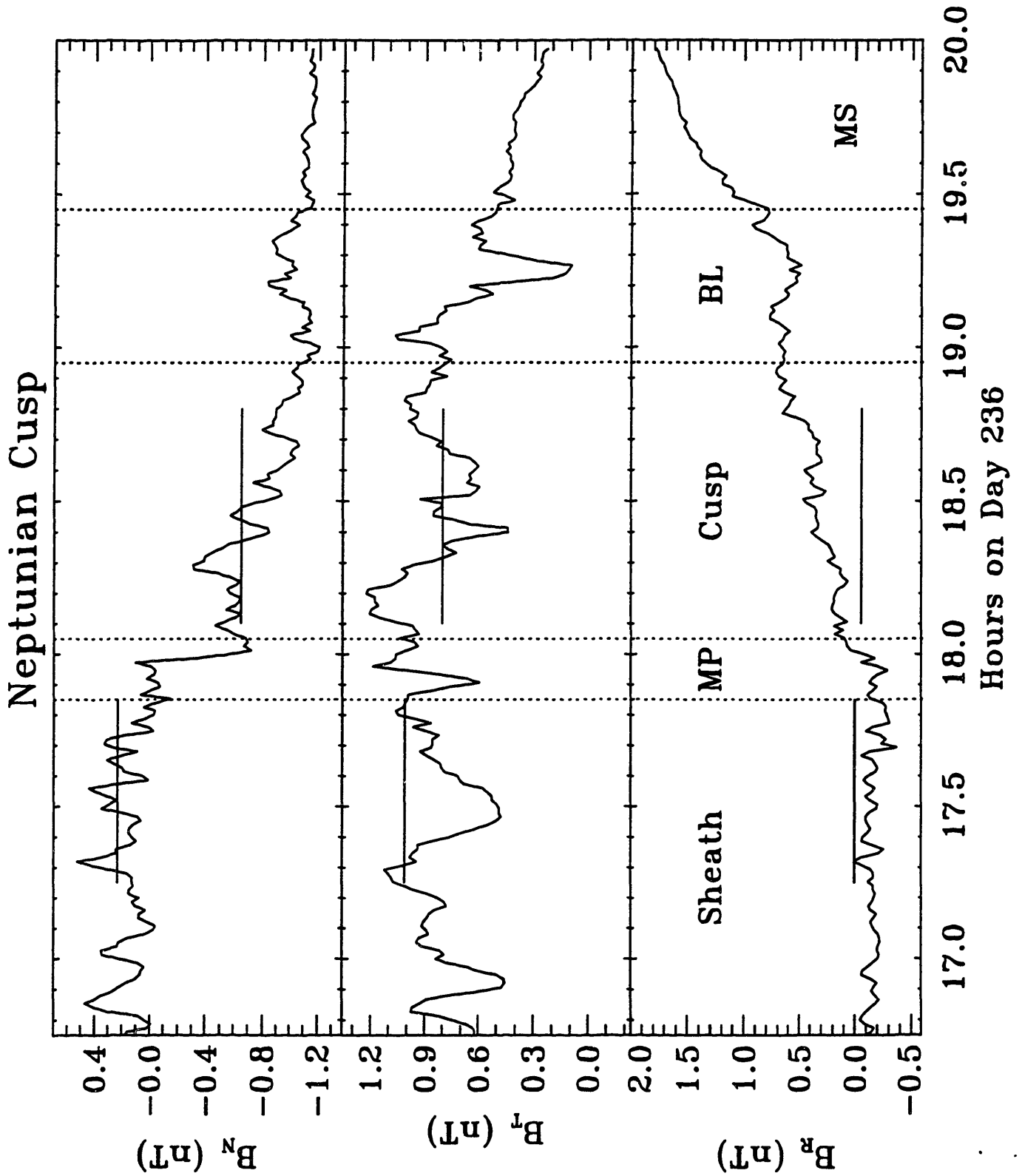


Fig. 43. Voyager 2 observations of the MP and cusp. Measurements shown are the RTN components of the 48 sec averaged magnetic field data. Long horizontal lines represent again the results of the MHD fit method.

panel. The solid dots with error bars represent densities obtained from single L-mode spectra (for a detailed description of the PLS instrument and data analysis used, see Chapter 1, Section 2.1 and 2.2), whereas the small horizontal bars with error bars show the densities obtained from averaged L-mode spectra. The length of the horizontal bar represents the length of the averaging interval. The long horizontal solid and dotted lines show the MHD fit results to be discussed later in this section. Also marked on the graph are the MP current layer, the cusp region, and a turbulent boundary layer (BL) at the upper border of the magnetosphere (MS) proper. The second panel presents the magnetic field magnitude in the same regions, with the plasma bulk velocity magnitudes shown on the third panel. On the top panel, the ion and electron "temperatures" are presented. Figure 4.2 shows the RTN components of the plasma bulk velocity in the same regions. The Neptune centered RTN coordinate system has been defined in the previous chapters (e.g. Chapter 2, Section 2). The solid dots and horizontal bars have the same meaning as described for the lower most panel of Figure 4.1. Finally, Figure 4.3 presents the 48s averaged magnetic field components in RTN coordinates. The MAG experiment has been described in Chapter 1, Section 2.3.

A magnetic variance analysis using the method of *Sonnerup and Cahill* [1967], described in the previous section, was employed throughout the MP and cusp regions using a "sliding" analysis interval of 9.6 minutes each. They were set to slide only 0.48 minutes so that the analysis acts as a smoothing filter through partial overlapping of analysis intervals. Based on the work of *Lepping and Behannon* [1980], results were rejected when the ratio of intermediate to smallest eigenvalue was less than 1.8. This limitation, however, presented no problem right at the MP discontinuity itself where the magnetic field vector rotated an immense 45°. This large rotation angle enabled a very reliable determination of the discontinuity surface normal as $\hat{n}_{MV} = (0.234, 0.963, -0.137)$ expressed in RTN coordinates pointing inward [*Lepping et al.*, 1992]. The unusually large tangential component of the surface normal suggests a significantly

indented MP surface near the spacecraft crossing (we expect it to be primarily radial here). *Lepping et al.* [1992] find, that for this surface normal direction, mass density flux conservation requires a MP bulk speed of 148 km/s along the normal, which is, curiously, in the opposite direction from the one expected from a rigidly corotating magnetospheric feature. However, in spite of the extremely large MP bulk speed and the significant plasma flow through the surface, pressure balance still holds.

When we apply the non-linear least squares MHD rotational discontinuity fitting technique, described in Section 2 of this chapter, a markedly different picture presents itself. However, before we can use the MHD fit method, we have to determine the MHD regions of validity both upstream and downstream from the MP, as is the case with all the types of MHD fitting techniques. These regions have to be sufficiently far away from the discontinuity so that non-MHD effects do not enter into our calculations, but not so far away as to include large-scale variations in the magnetosheath and cusp. Considering the data on Figures 4.1 - 4.3, the MP current layer (not to be included in the MHD regions) seems to be marked by large-scale fluctuations especially in the number density in the time interval 17.85 - 18.05 hrs. The beginning of the magnetosheath MHD region is not as evident. Several different intervals were tried. The longest one (used in all three plots to show the MHD results) begins right after the last large fluctuation in the sheath at 17.25 hr. The most stable results were obtained when this region was limited to the time interval 17.70 - 17.85 hrs. On the cusp side of the MP, the end of the MHD regions is again not obvious. The longest region tried in our fitting lasted till 18.90 hr. Shortening the interval did not produce significant improvement in our results.

After we have the MHD regions defined, the fitting technique described in Section 2 can be employed to find the most likely MP surface normal, bulk velocity, and asymptotic magnetofluid variables. In order to justify using the method developed to fit strictly rotational discontinuities (RD-s), we first have to show that the plasma density is indeed constant to a

good approximation. The error weighted average of the proton number density in the above described MHD regions is $0.0017 \pm 0.0003 \text{ cm}^{-3}$. This value is in very good agreement with the observations on the magnetosheath side, and also on the cusp side with the exception of two measurement points as shown on the lower most panel of Figure 4.1. This good agreement justifies the use of our MHD RD fitting method. Figure 4.4 shows the various confidence intervals of the fitted MP normal on a unit sphere. It is evident from this graph that the confidence regions are elongated along a plane cutting through the sphere as expected (see the discussion at step (I) in Section 2). With absolute confidence, we can only state that the RD surface normal lies somewhere in the plane containing the R axis, rotated from the T axis by $\approx 45^\circ$ toward the N axis. If indeed the fluctuations of the data around the MHD values are truly random, then we can believe the differentiation of the technique made within this plane. Then best fit MP normal is $\hat{n}_{\text{MHD}} = (-0.940, 0.342, -0.018)$ in RTN coordinates pointing away from Neptune. A small black diamond marks the location of the best fit on Figure 4.4. However, it is apparent that even the 1σ (68.3%) confidence region is very large and encompasses almost half of the best fit plane.

The fitted MP bulk velocity is $1 \pm 17 \text{ km/s}$ along the normal, much more moderate than what is predicted by the magnetic variance method, though the direction of the motion cannot be ascertained because of the large error bar. The best fit value of the conserved quantities of the plasma temperature and magnetic field magnitude are $T = 278 \pm 14 \text{ eV}$ and $|\mathbf{B}| = 1.1 \pm 1.2 \text{ nT}$. Both of these values are shown on Figure 4.1 indicating good agreement with the observations, though the magnetic field magnitude does have a large error bar due to the strongly fluctuating field. Finally the asymptotic magnetofluid parameters are determined and plotted on Figures 4.2 and 4.3. The error bars are again too large to be shown on these plots. However, the best fit values show remarkably good agreement with the observations with the possible exception of the N component of the plasma bulk velocity where the observations

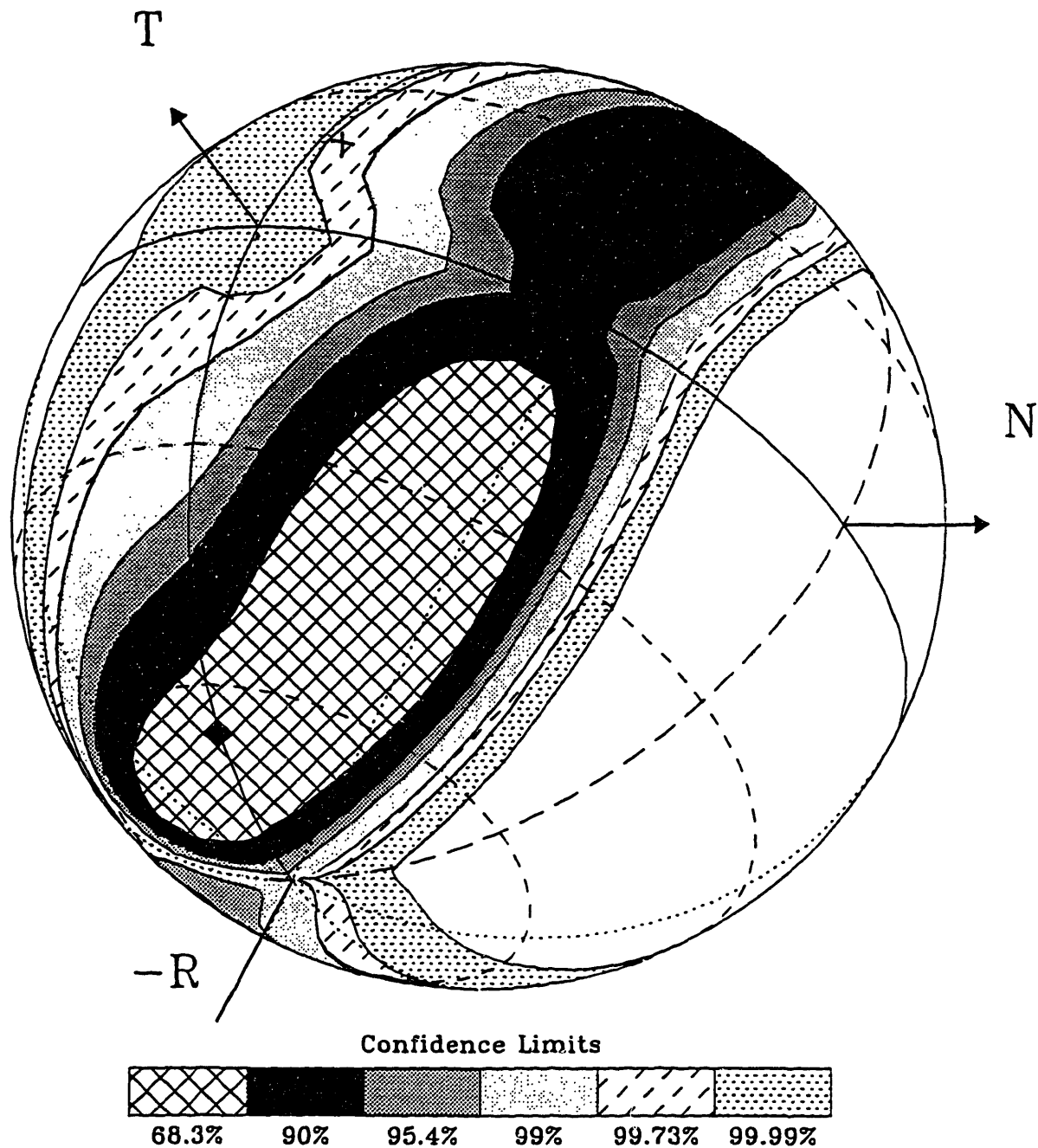


Fig. 4.4. Confidence limits of the MP surface normal as determined by the MHD rotational discontinuity fit. The confidence regions are shown on a unit sphere, the locus of all possible unit normal directions. A small black diamond represents the best fit direction, and an X marks the direction determined by the magnetic variance analysis.

never settle down to a steady value.

The relatively good agreement between the predicted MHD fit values and the observed magnetofluid parameters ensures the validity of the assumption of a rotational discontinuity for the MP and also the correctness of the MP surface normal determination. However, the surface normal direction determined by the MHD method differs from that of the magnetic variance method by the enormously large angle of $\cos^{-1}(\hat{n}_{MV} \cdot \hat{n}_{MHD}) = 83.6^\circ$. The direction of the surface normal \hat{n}_{MV} determined by the magnetic variance method is shown by an X on Figure 4.4. In spite of the large confidence regions of the MHD method, the variance analysis result falls into only the 99.73% confidence level which can hardly be taken as an agreement. Even if we allow \hat{n}_{MHD} to take any direction within all of the best fit plane, the minimum difference angle from \hat{n}_{MV} is $\approx 40^\circ$, which is still very significant.

For resolution of this apparent disagreement we have to look into the regions of observation these two methods rely on. As it was described in Section 3 of this chapter, the magnetic variance method relies on observations made only inside the MP layer or just outside of it. This method is highly reliable and the results at Neptune have a high confidence level, therefore, they cannot be dismissed but have to be looked at as revealing highly local characteristics of the MP surface. The MHD fit technique, on the other hand collects data from the much wider MHD regions, discussed above. These regions span up to 30,000 km before and after the MP layer and, therefore, the results reflect more the average, overall characteristics of the MP surface. In light of this realization, we can resolve the apparent disagreement between the results of the two techniques by introducing a ripple or a crest on the surface of the MP. Figure 4.5 shows two possible scenarios of the Voyager 2 MP crossing in the R-T plane. In both cases the very local surface normal at the MP crossing of the spacecraft points to the direction determined by the magnetic variance method, while the overall MP surface normal is still in the direction determined by the MHD fit method. Since

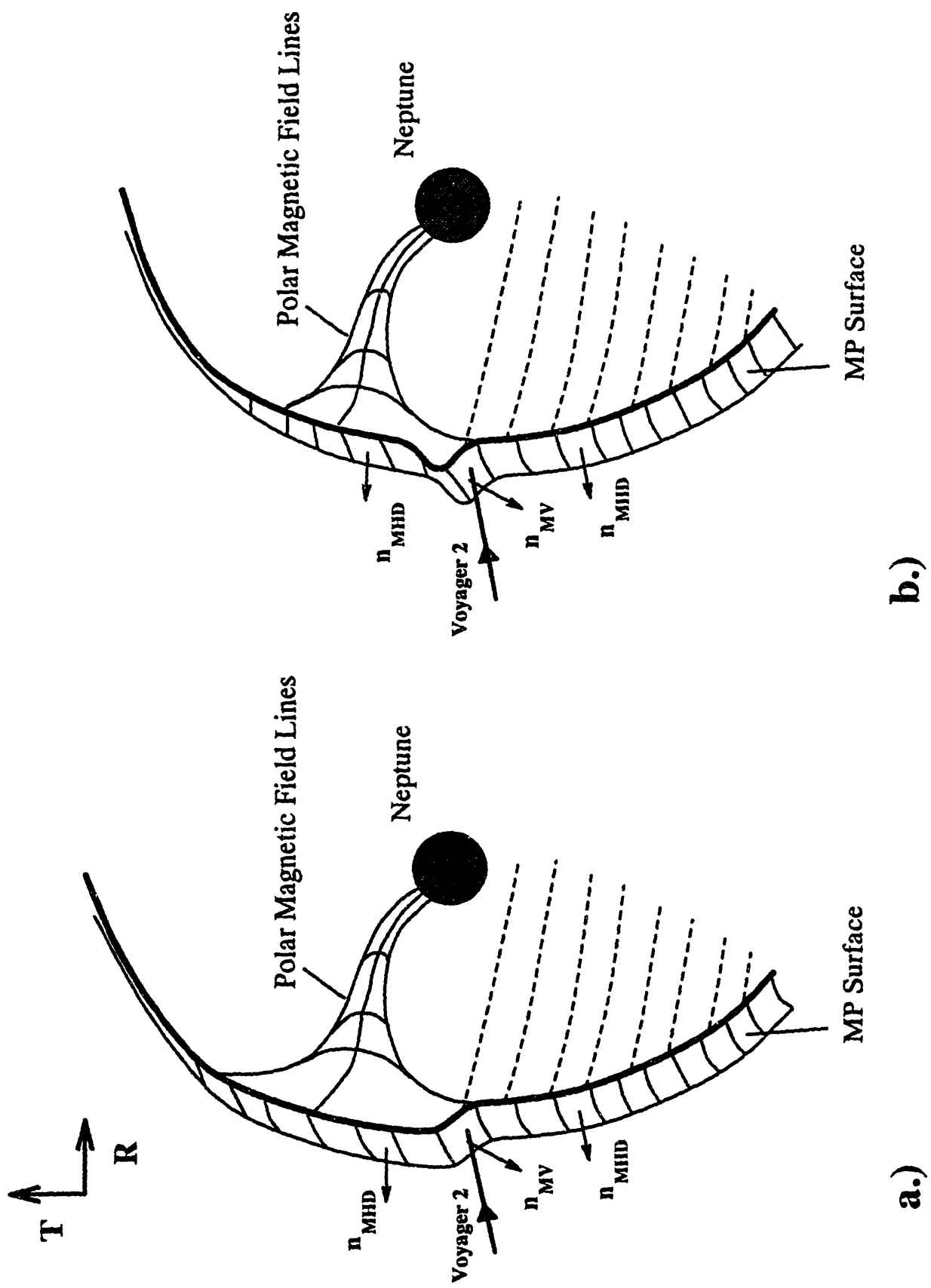


Figure 4.5. Schematics of possible magnetopause shapes in the R-T plane.

Voyager 2 crossed the inbound MP only once, there is no way to distinguish between the two scenarios depicted in Figure 4.5. However, for scenario b.), we can put a lower limit on the size of the bulge as many proton gyroradii.

To further motivate this interpretation of the results, we note that if the MP normal direction determined by the magnetic variance analysis represents the large scale orientation of the MP surface then it would indicate a major indentation over the weaker cusp field lines, as it is depicted in Figure 4.6, and necessitate that the spacecraft be in the +T direction from the cusp pole. Figure 4.7 shows the spacecraft trajectory near the MP in the T-N plane with the southern dipole axis position at the distance of the MP superimposed. Clearly, Voyager is in the -T direction from the cusp pole if it is not significantly moved from the dipole axis position. Even though at other planets it has been observed that the cusp pole moves away from the dipole axis toward the subsolar point [Siscoe, 1988], it has never been observed to be moved across the subsolar point which would be required to put the spacecraft in the +T direction from the cusp pole. Therefore, it is likely that the magnetic variance analysis reflects only local characteristics of the MP surface orientation.

Such a ripple or bulge is not unusual on the surface of planetary MP surfaces (see for example *Chen et al.* [1993] and references within). They can be caused by either pressure pulses propagating in the shocked magnetosheath plasma (evidence for pressure fluctuations in the Neptunian sheath can be seen on Figures 4.1 - 4.3), or by magnetic field lines merging at the MP which is also a possibility as the Neptunian MP was identified as a rotational discontinuity. The exact nature, however, of this surface ripple cannot be determined from a single crossing of the MP.

4.5 The Cusp: Entry Layer or Mantle?

Observational evidence for the open nature of the magnetosphere became available quite

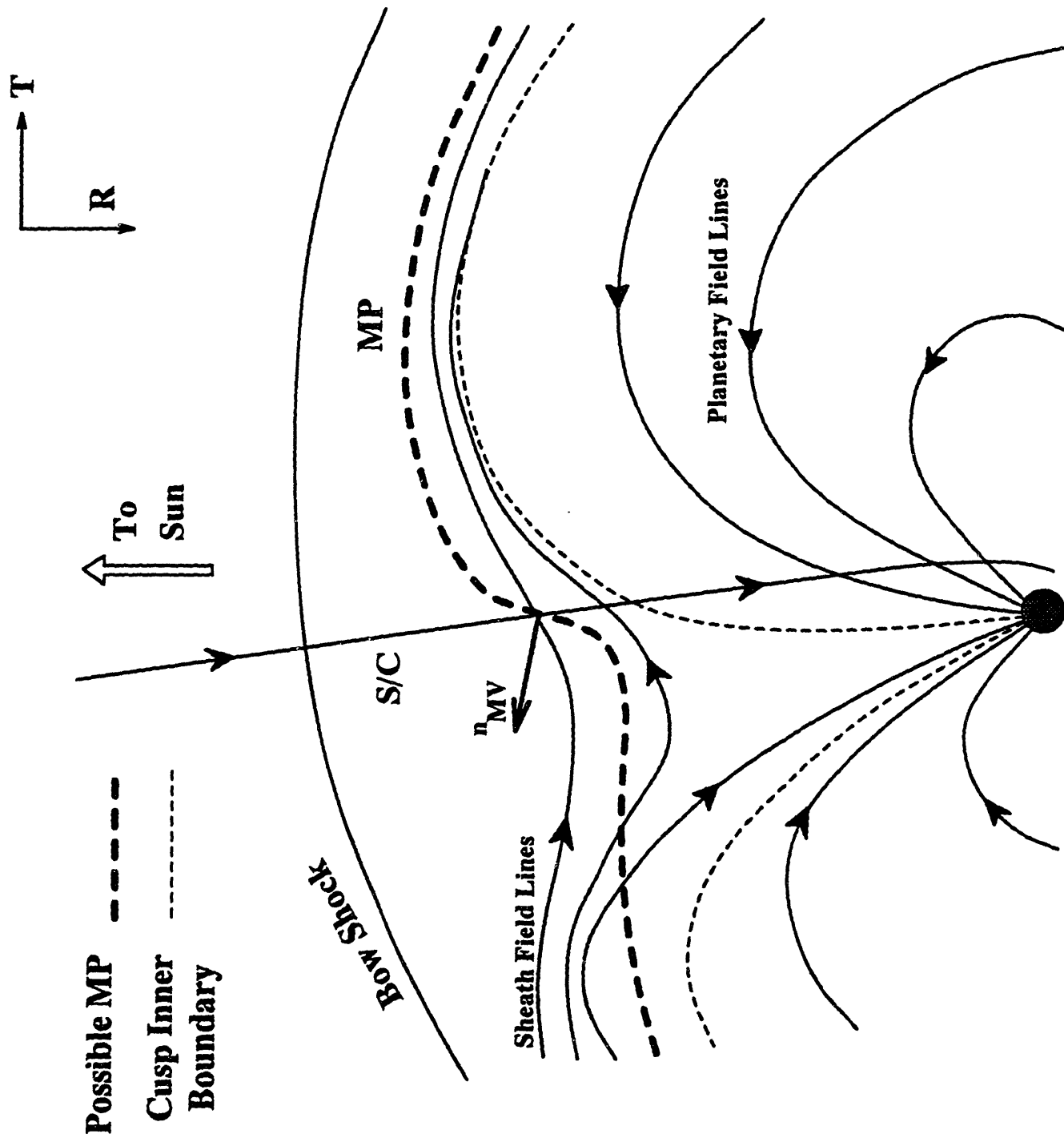


Fig. 4.6. A sketch of Neptune's magnetic field lines and possible MP shape around the inbound cusp region based on the results of the magnetic variance analysis.

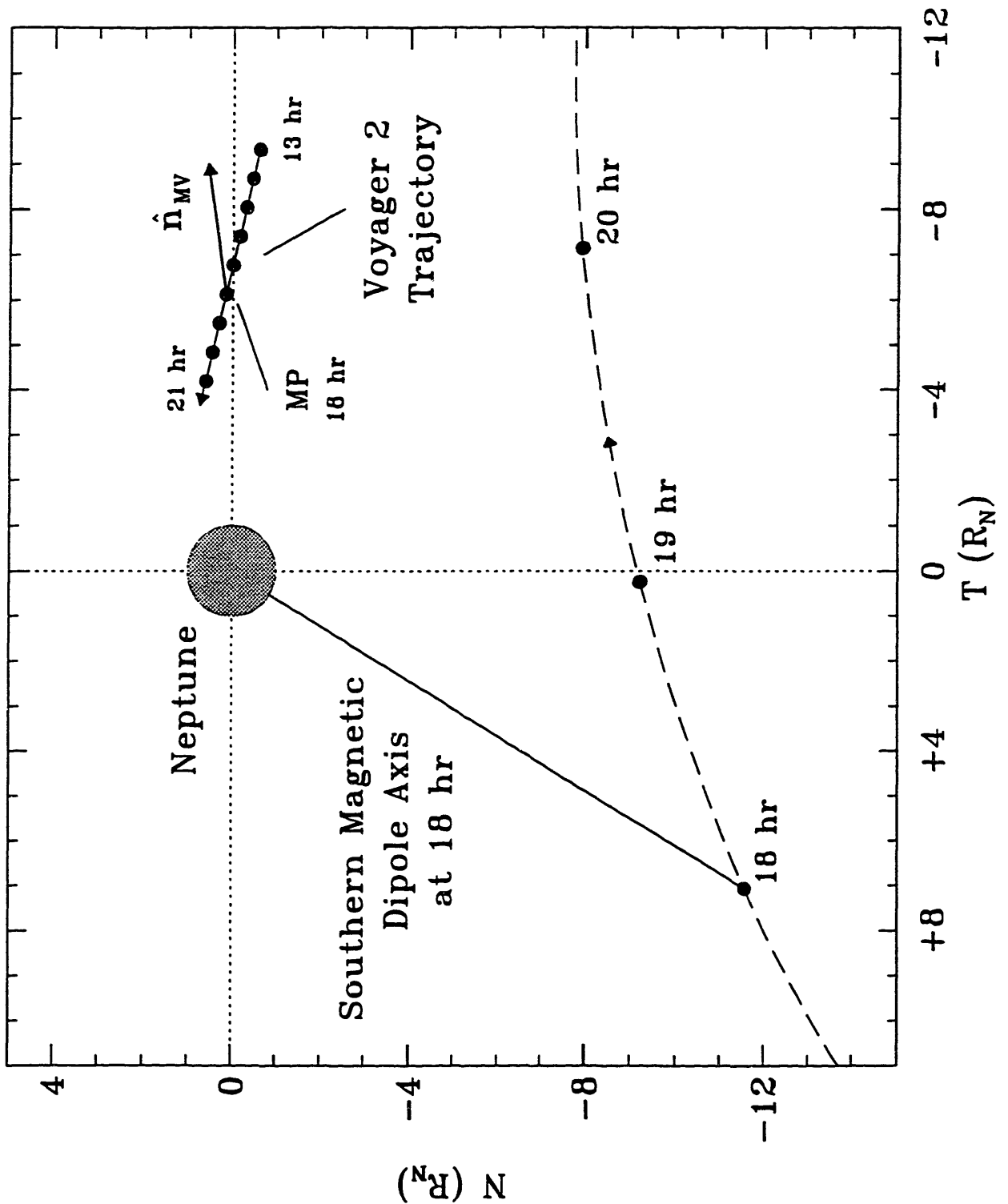


Fig. 4.7. The Voyager 2 trajectory near the MP crossing in the T-N plane. Also shown is the projection of the southern magnetic dipole axis to a sphere of radius of the MP stand-off distance. The solid dots are hourly tick marks. The MP was crossed by Voyager at 18 hr. \hat{n}_{MV} is the MP surface normal determined by the magnetic variance analysis.

some time ago in the case of Earth (for a comprehensive review of this topic see *Siscoe* [1988]). And by now, plasma of magnetosheath origin has been identified in boundary layers in the Earth outer magnetosphere at just about all magnetic latitudes. The nature of entry of the plasma through the MP and the characteristics of the boundary layers are, however, markedly different at different latitudes. Figure 4.8 gives a quick overview of the different boundary regions. This figure is reproduced from the work of *Haerendel et al.* [1978]. They identify three distinct regions of the Earth dayside boundary layer. At the lowest magnetic latitudes, where magnetosheath plasma enters mainly via diffusion, the boundary layer is labeled as Low Latitude Boundary Layer (LLBL). This region is of the least interest to our current investigation since Voyager 2 crossed the Neptunian MP at very high magnetic latitudes. On the subsolar side of the Earth's distant polar cusp region, *Paschmann et al.* [1976] observed magnetic field line merging from the Earth's magnetosheath which allows sheath plasma to enter the upper magnetosphere. The boundary layer formed by the entering sheath plasma is termed Entry Layer (EL) and is characterized by highly variable plasma bulk velocities (both in direction and in magnitude) and no particular correlation with the local magnetic field lines. On the night side of the Earth's distant polar cusp, *Rosenbauer et al.* [1975] identified a boundary layer containing plasma of sheath origin stably flowing in the anti-parallel direction to the magnetic field. This region, called the Plasma Mantle (PM), is also characterized by constant plasma temperatures but with a strong anisotropy, and a slow mode expansion fan (plasma density slowly decreasing with decreasing radial distance accompanied by a slowly increasing magnetic field magnitude).

As we have argued in the earlier sections, the Neptunian MP does allow some of the magnetosheath plasma to enter the upper magnetosphere, and indeed Voyager 2 observed plasma of sheath characteristics for almost two hours after the MP crossing before the densities dropped below the instrument threshold. Referring back to the plots of the observations

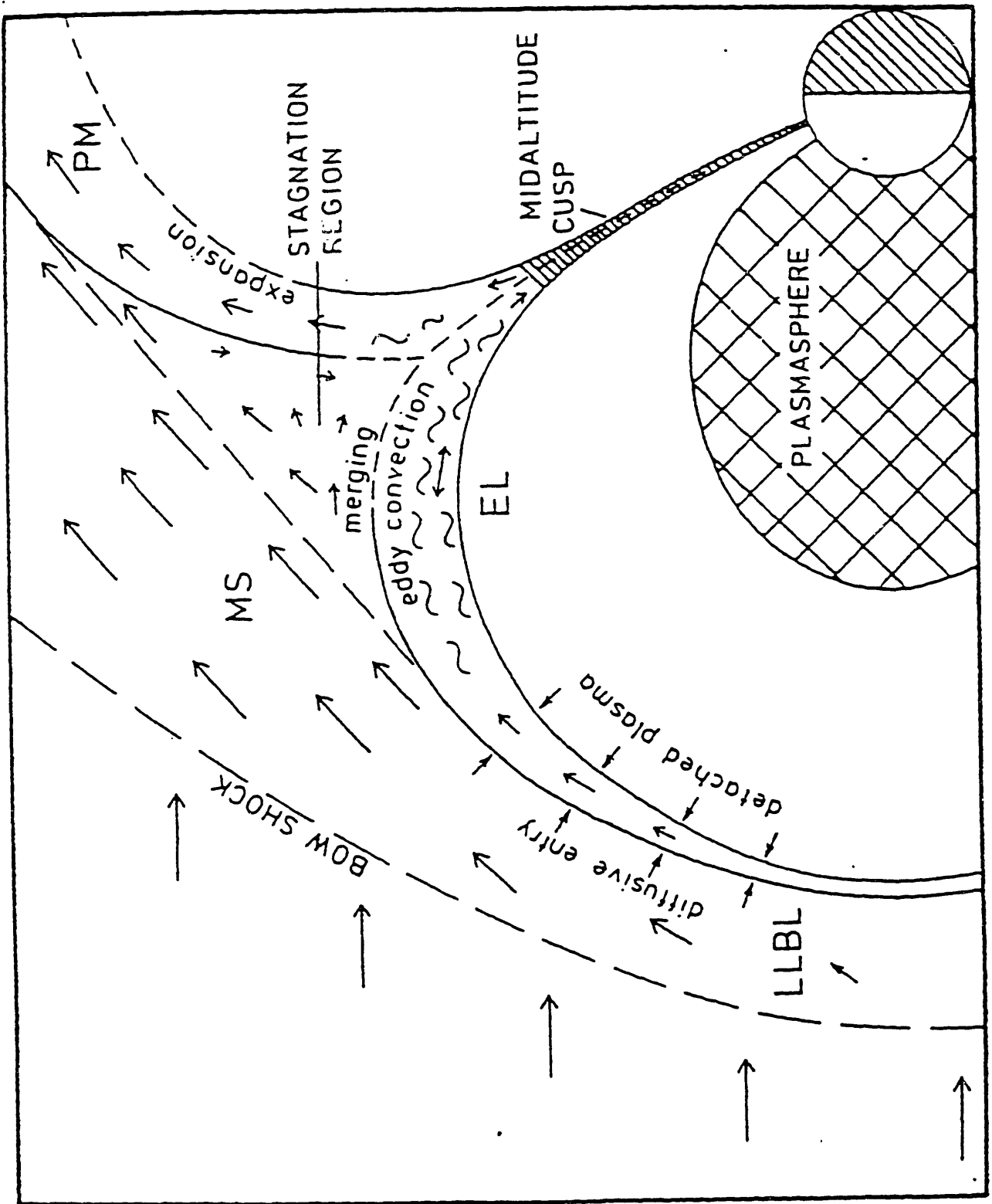


Fig. 4.8. Schematic diagram of the different regions of the Earth's MP boundary layer [Haerendel et al., 1978]. For a description of the different regions see the text.

(Figures 4.1 - 4.3), close after the MP crossing, till about 18.40 hr, all the magnetofluid parameters undergo large fluctuations, and if we plot (see Figure 4.9) the direction of plasma flow (solid dots) on the top of the anti-field directions (continuous line) we can observe very little correlation especially in the East-West angle. However, after 18.40 hr until about 19.00 hr the flow becomes more orderly and more or less anti-fieldward in direction. Also the plasma temperature is very constant, while the magnetic field magnitude slowly increases with a general tendency of the plasma number density to decrease, characteristic of slow mode expansion fans. Based on these observations, we would label the first region of the Neptunian cusp (between 18.05 and 18.40 hrs) as an entry layer or at least showing the same characteristics as the EL at Earth. The second cusp region, in the same way, would be labeled as plasma mantle. The existence of a dayside plasma mantle region at Neptune is not surprising, since plasma mantle signatures are reported from the Neptunian magnetotail [Zhang *et al.*, 1990; Richardson *et al.*, 1993], and some of the tailside mantle plasma most come from dayside merging regions.

Lepping et al. [1992] identify another magnetic rotational discontinuity at around 19.50 hr marking the entrance of the spacecraft into the magnetosphere proper where the magnetic field lines point in the directions expected from the planetary dipole field. Before this boundary, between 19.00 and 19.50 hrs, the observed magnetofluid parameters become highly fluctuating again. We refer to this region as boundary layer (BL) for the lack of a proper identification.

In summary, the use of both the magnetic variance and MHD fitting technique yield the result that the Neptunian dayside MP is a rotational discontinuity allowing the flow of shocked solar wind plasma into the upper regions of the planetary magnetosphere, forming a boundary layer generally referred to as the polar cusp. Based on the Voyager 2 magnetofluid observations, we identify regions in the Neptunian cusp similar to the Earth's entry layer and plasma mantle. This plasma mantle region might be a significant plasma source of the observed

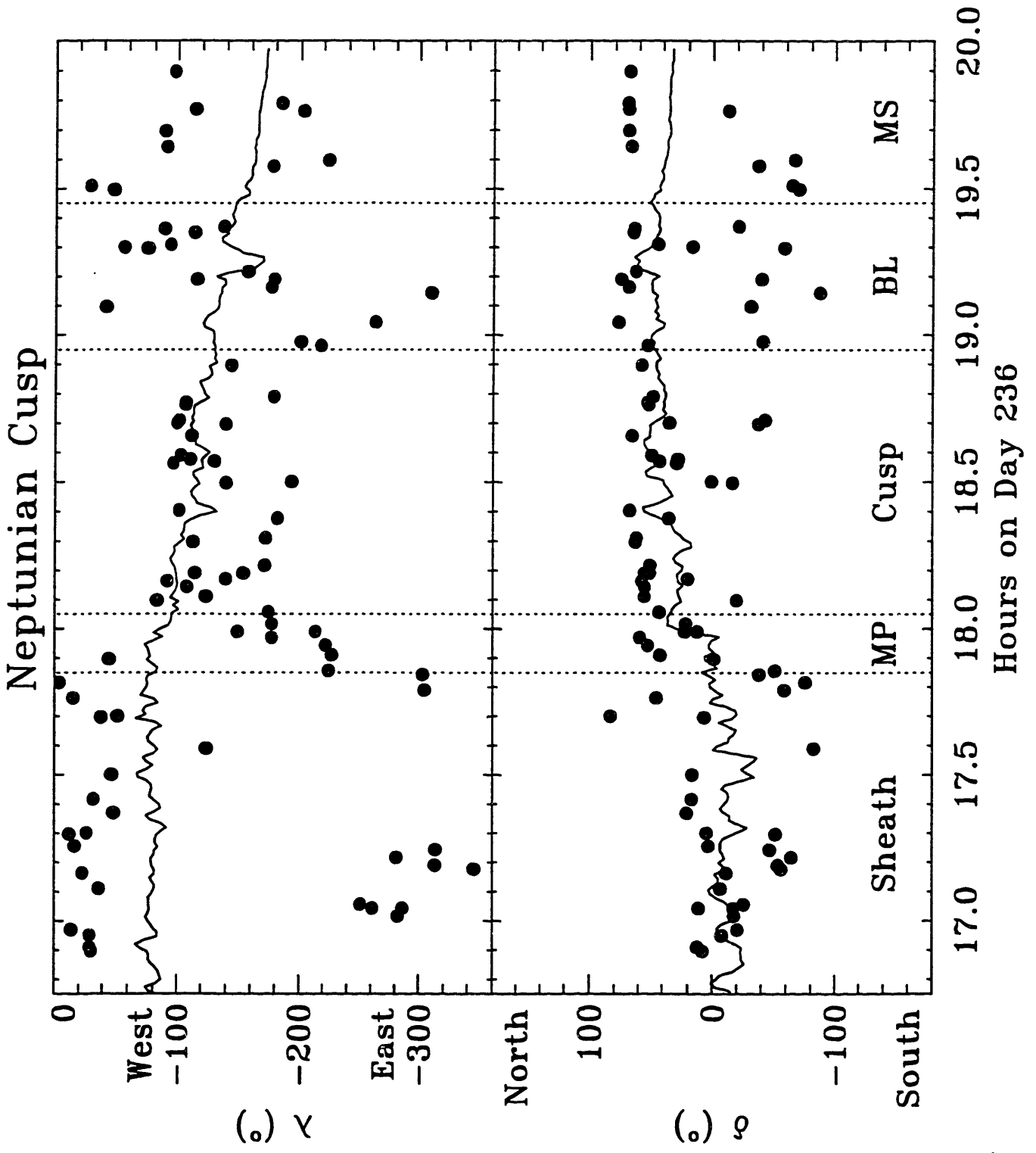


Fig. 4.9. East-West and North-South angles of the plasma bulk velocity (solid dots) and the reverse magnetic field (continuous lines) directions at the Neptunian MP and cusp regions.

tailside mantle regions. Also a ripple on the surface of the MP is conjectured based on the differing MP surface normals yielded by the magnetic variance and MHD fitting methods.

CHAPTER 5

CONCLUSIONS

In this thesis, we have followed the solar wind plasma traveling from region to region as it interacted with the Neptunian magnetosphere. Some of these regions were found to be very similar to those found at other magnetized planets, while some showed unique characteristics never before encountered. This analysis also prompted the development of two new magnetohydrodynamic (MHD) methods, one fitting generalized strong shocks, the other the special case of rotational discontinuities. Prompted by our observations, a number of different theories, describing various observed phenomena, are presented.

As part of our study of the inbound bow shock, we have extended the non-linear least squares, MHD jump conditions fitting technique of *Viñas and Scudder* [1986] to include plasma temperature observations in the form of the conservation of the normal momentum flux and energy density flux. This improved technique not only completes the set of fitted "Rankine-Hugoniot" jump condition equations, but also incorporates the effect of the individual errors in the measured data points, serving as a weighting function to our fitting procedure. Also, this technique allows the formation of all possible data pairs across the shock, thus improving the statistics of the analysis. The method proved very successful in fitting model synthetic shocks as well as the data obtained by Voyager 2 at the inbound Neptunian bow shock. Even though in this thesis no further application of this method is presented, the author firmly believes that this improved procedure will enable more refined studies of the other planetary bow shock encounters.

Our improved analysis technique reveals that the nearly subsolar Neptunian bow shock is a low β , high Mach number, quasi-perpendicular strong shock slowly moving away from the

planet toward the Sun. The calculated asymptotic magnetofluid states are in good agreement with the spacecraft observations further verifying the validity of our fit results. The new technique was able to determine that in the upstream regions, the ratio of specific heats γ is around 1.9 with a considerable uncertainty. This result, indicating about two degrees of freedom, is consistent with observations at other planets. On the downstream side of the shock, the value of γ is resolved to a much higher degree of accuracy, and is equal to 1.4, suggesting an increased number of degrees-of-freedom.

Once the bulk speed of the bow shock was determined, and knowing the velocity of the spacecraft, we were able to determine the scale lengths of the various shock microstructure features. Resolving these features is significant not only because it has never been done before for the case of Neptune, but because it adds a new example with a new set of parameters to the list of already analyzed planetary shock features, allowing the further refinement of the related plasma theories. The observed shock foot length was found to be in the best agreement with the model predictions of *Schwartz et al.* [1983] and that of *Goodrich* [1985]. Compared to similar features at other planets, the Neptunian foot was found almost twice as wide as that of the Earth as reported by *Sckopke et al.* [1983], and very similar to that found at Uranus by *Bagenal et al.* [1987]. The Neptunian shock ramp was found to be significantly thicker than any other observed planetary ramps or what typical theories predict with the possible exception of *Leroy et al.* [1982]. We were able to model the wide Neptunian shock ramp only if we adopted the anomalously high value of $\eta/4\pi = 5.3 \times 10^{-5}$ s for the electron resistivity. The shock overshoot region length and magnitude were found in good agreement with those predicted by theory and empirical relationships [*Sckopke et al.*, 1983; *Goodrich*, 1985; *Russell et al.*, 1982; and *Leroy*, 1983].

The observed magnetofluid parameters in the Neptunian magnetosheath were found to be well modeled by a simple gas dynamic simulation with convected magnetic fields [*Spreiter et*

al., 1966]. Significant discrepancies were only observed by Voyager 2 near the magnetopause (MP) crossing. We suggested that these differences from the gas dynamic predictions are largely due to Neptune's unique magnetic configuration and the serendipitous timing of the Voyager 2 MP crossing. The MP encountered was established to be rotational in nature, therefore allowing the sheath plasma to flow through the MP surface. This feature could explain the less than expected plasma density and temperatures in the nearby sheath regions and also the unusual magnetic field orientations.

Voyager 2 encountered the Neptunian MP at very high magnetic latitudes while it was still facing into the shocked solar wind flow. To analyze this unusually positioned MP, the traditional magnetic variance analysis was supplemented by our newly developed MHD rotational discontinuity fitting technique. The two independent methods agreed that the observed MP is a rotational or rotational-like discontinuity. However, they significantly disagreed about the orientation of the MP surface normal. To resolve this apparent discrepancy, we proposed a model of the MP surface which includes a large ripple traveling along the local magnetic field lines. This model seems to be able to account for all of the observed phenomena at the MP. This analysis, however, is far from complete, since the MHD fitting was not able to find exact matches with the measured magnetofluid parameters. It is suggested that a dissipational version of the MHD method be developed in the future in the hope of explaining some of the discrepancies from our current theories.

Finally, the upper regions of the Neptunian magnetosphere were analyzed. These regions contain the sheath plasma that entered through the open boundary of the MP. We have found that the upper region is more turbulent without any correlation and is very similar to the entry layer of the Earth. Lower in the cusp region, we have observed a more orderly flow of the plasma along the magnetic field lines and also have noted that the plasma observations showed signs of a slow mode expansion fan characteristic of plasma mantle regions. These open

magnetospheric regions of the entry layer and the plasma mantle are suggested to be the plasma source for the previously observed tailside plasma mantle [*Zhang et al.*, 1990; *Richardson et al.*, 1993].

Though it is truly exciting to analyze data from previously unvisited regions of our solar system, it is the hope of the author that this study is not only going to introduce Neptune as a strange new beast in the already sizable zoo of observed planetary magnetospheres, but that it would reveal the Neptunian system as a useful test site for our ever increasing understanding of space plasma physics, and therefore encourage future missions to the companions of our planet Earth.

REFERENCES FOR CHAPTER 1

- Barnett, A. S., and S. Olbert, The response function of modulated grid Faraday cup plasma instruments, *Rev. Sci. Instrum.*, *57*, 2432-2440, 1986.
- Behannon, K. W., M. H. Acuña, L. F. Burlaga, R. P. Lepping, N. F. Ness, and F. M. Neubauer, Magnetic field experiment for Voyager 1 and 2, *Space Sci. Rev.* *21*, 235, 1977.
- Belcher, J. W., C. K. Goertz, and H. S. Bridge, The low energy plasma in the Jovian magnetosphere, *Geophys. Res. Lett.*, *7*, 17-21, 1980.
- Belcher, J. W., H. S. Bridge, F. Bagenal, B. Coppi, O. Divers, A. Eviatar, G. S. Gordon, Jr., A. J. Lazarus, R. L. McNutt, Jr., K. W. Ogilvie, J. D. Richardson, G. L. Siscoe, E. C. Sittler, Jr., J. T. Steinberg, J. D. Sullivan, A. Szabo, L. Villanueva, V. M. Vasylunas, and M. Zhang, Plasma observations near Neptune: Initial results from Voyager 2, *Science*, *246*, 1478-1482, 1989.
- Bridge, H. S., J. W. Belcher, R. J. Butler, A. J. Lazarus, A. M. Mavretic, J. D. Sullivan, G. L. Siscoe, and V. M. Vasylunas, The plasma experiment on the 1977 Voyager mission, *Space Sci. Rev.*, *21*, 259-287, 1977.
- Howe, H. C., Jr., Pioneer 6 plasma measurements in the magnetosheath, *J. Geophys. Res.*, *75*, 2429-2437, 1970.
- Hundhausen, A. J., S. J. Bame, and J. R. Asbridge, Plasma flow pattern in the earth's magnetosheath, *J. Geophys. Res.*, *74*, 2799-2806, 1969.
- Lepping, R. P., J. E. P. Connerney, R. Kennon, T. Vollmer, and N. F. Ness, Voyager 2 Neptune magnetic field data: Summary plots and major characteristics, Laboratory for Extraterrestrial Physics, NASA/GSFC Document, May 1993.
- Montgomery, M. D., J. R. Asbridge, and S. J. Bame, Vela 4 plasma observations near the earth's bow shock, *J. Geophys. Res.*, *75*, 1217-1231, 1970.

- Ness, N. F., M. H. Acuna, L. F. Burlaga, J. E. P. Connerney, R. P. Lepping, and F. M. Neubauer, Magnetic fields at Neptune, *Science*, 246, 1473-1477, 1989.
- Olbert, S., in *Physics of the Magnetosphere*, R. L. Carovillano, J. F. McClay, and H. R. Radoski, eds, p. 641, Reider, Dordrecht, Holland, 1969.
- Richardson, J. D., Ion distribution functions in the dayside magnetosheaths of Jupiter and Saturn, *J. Geophys. Res.*, 92, 6133-6140, 1987.
- Scherb, F., *Space Res.*, 4, 797, 1964.
- Sckopke, N., G. Paschmann, S. J. Bame, J. T. Gosling, and C. T. Russell, Evolution of ion distributions across the nearly perpendicular bow shock: Specularly and nonspecularly reflected-gyrating ions, *J. Geophys. Res.*, 88, 6121-6136, 1983.
- Sittler, E. C., Jr., K. W. Ogilvie, and R. S. Selesnick, Survey of electrons in the Uranian magnetosphere: Voyager 2 observations, *J. Geophys. Res.*, 92, 15,263-15,281, 1987.
- Spreiter, J. R., A. Y. Alksne, and B. Abraham-Shrauner, *Planetary Space Sci.* 14, 1207, 1966.
- Tyler, G. L., D. N. Sweetnam, J. D. Anderson, S. E. Borutzki, J. K. Campbell, V. R. Eshleman, D. L. Gresh, E. M. Gurrola, D. P. Hinson, N. Kawashima, E. R. Kursinski, G. S. Levy, G. F. Lindal, J. R. Lyons, E. A. Marouf, P. A. Rosen, R. A. Simpson, and G. E. Wood, Voyager radio science observations of Neptune and Triton, *Science*, 246, 1466-1473, 1989.
- Vasyliunas, V. M., Deep space plasma measurements, in *Methods of Experimental Physics*, 9B, R. H. Lovbergs, ed., 49-88, 1971.
- Warwick, J. W., D. R. Evans, G. R. Peltzer, R. G. Peltzer, J. H. Romig, C. B. Sawyer, A. C. Riddle, A. E. Schweitzer, M. D. Desch, M. L. Kaiser, W. M. Farrel, T. D. Carr, I. de Pater, D. H. Staelin, S. Gulkis, R. L. Poynter, A. Boischof, F. Genova, Y. Leblanc, A. Lecacheux, B. M. Pederson, and P. Zarka, Voyager planetary radio astronomy at Neptune, *Science*, 246, 1498-1501, 1989.

Wolfe, J. H., and D. D. McKibben, Pioneer 6 observations of a steady state magnetosheath, *Planet. Space Sci.*, 16, 953-969, 1968.

Zhang, M., J. D. Richardson, and E. C. Sittler, Jr., Voyager 2 electron observations in the magnetosphere of Neptune, *J. Geophys. Res.*, 96, 19,085-19,100, 1991.

REFERENCES FOR CHAPTER 2

- Abraham-Shrauner, B., Determination of magnetohydrodynamic shock normals, *J. Geophys. Res.*, *77*, 736-739, 1972.
- Abraham-Shrauner, B., and S. H. Yun, Interplanetary shocks seen by Ames plasma probe on Pioneer 6 and 7, *J. Geophys. Res.*, *81*, 2097-2102, 1976.
- Bagenal, F., J. W. Belcher, E. C. Sittler, and R. P. Lepping, The Uranian bow shock: Voyager 2 inbound observations of a high Mach number shock, *J. Geophys. Res.*, *92*, 8603-8612, 1987.
- Barnett, A. S., and S. Olbert, The response function of modulated grid Faraday cup plasma instruments, *Rev. Sci. Instrum.*, *57*, 2432-2440, 1986.
- Belcher, J. W., et al., Plasma observations near Neptune: Initial results from Voyager 2, *Science*, *246*, 1478-1482, 1989.
- Bridge, H. S., J. W. Belcher, R. J. Butler, A. J. Lazarus, A. M. Mavretic, J. D. Sullivan, G. L. Siscoe, and V. M. Vasyliunas, The plasma experiment on the 1977 Voyager mission, *Space Sci. Rev.*, *21*, 259-287, 1977.
- Goodrich, C. C., Numerical simulations of quasi-perpendicular collisionless shocks, in *Collisionless Shocks in the Heliosphere, Review of Current Research, Geophys. Monogr. Ser.*, Vol. 35, edited by B. T. Tsurutani and R. G. Stone, pp. 153-168, AGU, Washington, D.C., 1985.
- Howe, H. C., Jr., Pioneer 6 plasma measurements in the magnetosheath, *J. Geophys. Res.*, *75*, 2429-2437, 1970.
- Hundhausen, A. J., S. J. Bame, and J. R. Asbridge, Plasma flow pattern in the earth's magnetosheath, *J. Geophys. Res.*, *74*, 2799-2806, 1969.
- Lepping, R. P., and P. D. Argentiero, Single spacecraft method of estimating shock normals, *J.*

- Geophys. Res.*, 76, 4349-4359, 1971.
- Lepping, R. P., J. E. P. Connerney, R. Kennon, T. Vollmer, and N. F. Ness, Voyager 2 Neptune magnetic field data: Summary plots and major characteristics, Laboratory for Extraterrestrial Physics, NASA/GSFC Document, May 1993.
- Leroy, M. M., D. Winske, C. C. Goodrich, C. S. Wu, and K. Papadopoulos, The structure of perpendicular bow shocks, *J. Geophys. Res.*, 87, 5081-5094, 1982.
- Leroy, M. M., Structure of perpendicular shocks in collisionless plasma, *Phys. Fluids*, 26, 2742-2753, 1983.
- Montgomery, M. D., J. R. Asbridge, and S. J. Bame, Vela 4 plasma observations near the earth's bow shock, *J. Geophys. Res.*, 75, 1217-1231, 1970.
- Moses, S. L., F. V. Coroniti, C. F. Kennel, F. L. Scarf, E. W. Greenstadt, W. S. Kurth, and R. P. Lepping, High time resolution plasma wave and magnetic field observations of the Jovian bow shock, *Geophys. Res. Lett.*, 12, 183, 1985.
- Ness, N. F., M. H. Acuna, L. F. Burlaga, J. E. P. Connerney, R. P. Lepping, and F. M. Neubauer, Magnetic fields at Neptune, *Science*, 246, 1473-1477, 1989.
- Paschmann, G., N. Sckopke, S. J. Bame, and J. T. Gosling, Observations of gyrating ions in the foot of the nearly perpendicular bow shock, *Geophys. Res. Lett.*, 9, 881-884, 1982.
- Press, W. H., B. P. Flannery, S. A. Teukolsky, and W. T. Vetterling, *Numerical Recipes, The Art of Scientific Computing*, Cambridge University Press, pp. 521-538, 1986.
- Quest, K. B., Electron resistivity in high Mach number perpendicular shocks, *J. Geophys. Res.*, 91, 8805-8816, 1986.
- Richardson, J. D., Ion distribution functions in the dayside magnetosheaths of Jupiter and Saturn, *J. Geophys. Res.*, 92, 6133-6140, 1987.
- Russell, C. T., M. M. Hope, and W. A. Livesey, Overshoots in planetary bow shocks, *Nature*, 296, 45, 1982.

- Schwartz, S. J., M. F. Thomsen, and J. T. Gosling, Ions upstream of the Earth's bow shock: A theoretical comparison of alternative source populations, *J. Geophys. Res.*, **88**, 2039, 1983.
- Schwartz, S. J., Solar wind and the Earth's bow shock. In *Solar System Magnetic Fields, Geophys. and Astrophys. Monogr.*, ed. E. R. Priest, Hingham:Kluwer Academic Publishers, pp. 25-36, 1985.
- Scokopke, N., G. Paschmann, S. J. Bame, J. T. Gosling, and C. T. Russell, Evolution of ion distributions across the nearly perpendicular bow shock: Specularly and nonspecularly reflected-gyrating ions, *J. Geophys. Res.*, **88**, 6121-6136, 1983.
- Sittler, E. C., Jr., and J. D. Scudder, An empirical polytropic law for solar wind thermal electrons between 0.45 and 4.76 AU: Voyager 2 and Mariner 10, *J. Geophys. Res.*, **85**, 5131-5137, 1980.
- Sittler, E. C., Jr., K. W. Ogilvie, and R. S. Selesnick, Survey of electrons in the Uranian magnetosphere: Voyager 2 observations, *J. Geophys. Res.*, **92**, 15,263-15,281, 1987.
- Slavin, J. A., E. J. Smith, J. R. Spreiter, and S. S. Stahara, Solar wind flow around the outer planets: Gas dynamic modeling of the Jupiter and Saturn bow shocks, *J. Geophys. Res.*, **90**, 6275-6286, 1985.
- Spreiter, J. R., and S. S. Stahara, Magnetohydrodynamic and gasdynamic theories for planetary bow waves, in *Collisionless Shocks in the Heliosphere, Review of Current Research, Geophys. Monogr. Ser.*, Vol. 35, edited by B. T. Tsurutani and R. G. Stone, pp. 85-107, AGU, Washington, D.C., 1985.
- Stahara, S. S., R. R. Rachiele, J. R. Spreiter, and J. A. Slavin, A three dimensional gasdynamic model for solar wind flow past nonaxisymmetric magnetospheres: Application to Jupiter and Saturn, *J. Geophys. Res.*, **94**, 13,353-13,365, 1989.
- Szabo, A., An improved solution to the "Rankine-Hugoniot" Problem, submitted to the *J. Geophys. Res.*, 1993.

- Viñas, A. F., and J. D. Scudder, Fast optimal solution to the "Rankine-Hugoniot problem", *J. Geophys. Res.*, 91, 39-58, 1986.
- Wolfe, J. H., and D. D. McKibben, Pioneer 6 observations of a steady state magnetosheath, *Planet. Space Sci.*, 16, 953-969, 1968.
- Zhang, M., J. D. Richardson, and E. C. Sittler, Jr., Voyager 2 electron observations in the magnetosphere of Neptune, *J. Geophys. Res.*, 96, 19,085-19,100, 1991.

REFERENCES FOR CHAPTER 3

- Belcher, J. W., H. S. Bridge, F. Bagenal, B. Coppi, O. Divers, A. Eviatar, G. S. Gordon, Jr., A. J. Lazarus, R. L. McNutt, Jr., K. W. Ogilvie, J. D. Richardson, G. L. Siscoe, E. C. Sittler, Jr., J. T. Steinberg, J. D. Sullivan, A. Szabo, L. Villanueva, V. M. Vasyliunas, and M. Zhang, Plasma observations near Neptune: Initial results from Voyager 2, *Science*, **246**, 1478-1482, 1989.
- Cairns, I. H., C. W. Smith, W. S. Kurth, D. A. Gurnett, and S. Moses, Remote sensing of Neptune's bow shock: Evidence for large-scale shock motions, *J. Geophys. Res.*, **96**, 19,153-19,169, 1991.
- Landau, L. D., E. M. Lifshitz, and L. P. Pitaevskii, *Electrodynamics of Continuous Media*, Landau and Lifshitz Course of Theoretical Physics, vol. 8, pp. 225ff., Institute of Physical Problems, USSR Academy of Sciences, Moscow, translated by J. B. Sykes, J. S. Bell, and M. J. Kearsley, Pergamon Press, 1984.
- Ness, N. F., M. H. Acuna, L. F. Burlaga, J. E. P. Connerney, R. P. Lepping, and F. M. Neubauer, Magnetic fields at Neptune, *Science*, **246**, 1473-1477, 1989.
- Richardson, J. D., G. L. Siscoe, S. S. Stahara, J. R. Spreiter, and A. Szabo, The magnetosheath of Neptune: Models and Observations, in preparation for publication, 1993.
- Russell, C. T., Planetary bow shocks, in *Collisionless Shocks in the Heliosphere: Reviews of Current Research*, *Geophys. Monogr. Ser.*, vol. 35, edited by B. T. Tsurutani and R. G. Stone, pp. 109-130, AGU, Washington D.C., 1985.
- Slavin, J. A., E. J. Smith, J. R. Spreiter, and S. S. Stahara, Solar wind flow around the outer planets: Gas dynamic modeling of the Jupiter and Saturn bow shocks, *J. Geophys. Res.*, **90**, 6275-6286, 1985.
- Spreiter, J. R., A. L. Summers, and A. Y. Alksne, Hydromagnetic flow around the

magnetosphere, *Planet. Space Sci.*, 16, 223, 1966.

Spreiter, J. R., and S. S. Stahara, Magnetohydrodynamic and gasdynamic theories for planetary bow waves, in *Collisionless Shocks in the Heliosphere: Reviews of Current Research*, *Geophys. Monogr. Ser.*, vol. 35, edited by B. T. Tsurutani and R. G. Stone, pp. 85-107, AGU, Washington D.C., 1985.

Stahara, S. S., R. R. Rachiele, J. R. Spreiter, and J. A. Slavin, A three dimensional gasdynamic model for solar wind flow past nonaxisymmetric magnetospheres: Application to Jupiter and Saturn, *J. Geophys. Res.*, 94, 13,353-13,365, 1989.

Szabo, A., A. J. Lazarus, R. L. McNutt, Jr., G. L. Siscoe, R. P. Lepping, and N. F. Ness, Magnetopause and cusp observations at Neptune, *J. Geophys. Res.*, 96, 19,149-19,153, 1991.

REFERENCES FOR CHAPTER 4

- Belcher, J. W., H. S. Bridge, F. Bagenal, B. Coppi, O. Divers, A. Eviatar, G. S. Gordon, Jr., A. J. Lazarus, R. L. McNutt, Jr., K. W. Ogilvie, J. D. Richardson, G. L. Siscoe, E. C. Sittler, Jr., J. T. Steinberg, J. D. Sullivan, A. Szabo, L. Villanueva, V. M. Vasyliunas, and M. Zhang, Plasma observations near Neptune: Initial results from Voyager 2, *Science*, 246, 1478-1482, 1989.
- Chen, S.-H., M. G. Kivelson, J. T. Gosling, R. J. Walker, and A. J. Lazarus, Anomalous aspects of magnetosheath flow and of the shape and oscillations of the magnetopause during an interval of strongly northward interplanetary magnetic field, *J. Geophys. Res.*, 98, 5727-5742, 1993.
- Connerney, J. E. P., M. H. Acuña, and N. F. Ness, The magnetic field of Neptune, *J. Geophys. Res.*, 96, 19,023, 1991.
- Haerendel, G., G. Paschmann, N. Sckopke, H. Rosenbauer, and P. C. Hedgecock, The frontside boundary layer of the magnetosphere and the problem of reconnection, *J. Geophys. Res.*, 83, 3195-3216, 1978.
- Lepping, R. P., and K. W. Behannon, Magnetic field directional discontinuities, 1: Minimum variance errors, *J. Geophys. Res.*, 85, 4695-4703, 1980.
- Lepping, R. P., L. F. Burlaga, A. J. Lazarus, V. M. Vasyliunas, A. Szabo, J. T. Steinberg, N. F. Ness, and S. M. Krimigis, Neptune's polar cusp region: Observations and magnetic field analysis, *J. Geophys. Res.*, 97, 8135-8144, 1992.
- Ness, N. F., M. H. Acuna, L. F. Burlaga, J. E. P. Connerney, R. P. Lepping, and F. M. Neubauer, Magnetic fields at Neptune, *Science*, 246, 1473-1477, 1989.
- Paschmann, G., G. Haerendel, N. Sckopke, H. Rosenbauer, and P. C. Hedgecock, Plasma and magnetic field characteristics of the distant polar cusp near local noon: The entry layer, *J.*

- Geophys. Res.*, 81, 2883-2899, 1976.
- Press, W. H., B. P. Flannery, S. A. Teukolsky, and W. T. Vetterling, *Numerical Recipes, The Art of Scientific Computing*, Cambridge University Press, pp. 521-538, 1986.
- Richardson, J. D., G. L. Siscoe, S. S. Stahara, J. R. Spreiter, and A. Szabo, The Magnetosheath of Neptune: Models and observations, submitted to *J. Geophys. Res.*, 1993.
- Rosenbauer, H., H. Grunwaldt, M. D. Montgomery, G. Paschmann, and N. Sckopke, HEOS 2 plasma observations in the distant polar magnetosphere: The plasma mantle, *J. Geophys. Res.*, 80, 2723-2737, 1975.
- Siscoe, G. L., The magnetospheric boundary, in *Physics of Space Plasmas (1987), SPI Conference Proceedings and Reprint Series, Number 7*, edited by T. Chang, G. B. Crew, and J. R. Jasperse, p. 73, Scientific Publishers, Inc., Cambridge, MA, 1988.
- Sonnerup, B. U. O., and L. J. Cahill, Jr., Magnetopause structure and attitude from Explorer 12 observations, *J. Geophys. Res.*, 72, 171-183, 1967.
- Szabo, A., A. J. Lazarus, R. L. McNutt, Jr., G. L. Siscoe, R. P. Lepping, and N. F. Ness, Magnetopause and cusp observations at Neptune, *J. Geophys. Res.*, 96, 19,149-19,153, 1991.
- Szabo, A., An improved solution to the "Rankine-Hugoniot" Problem, submitted to the *J. Geophys. Res.*, 1993.
- Viñas, A. F., and J. D. Scudder, Fast optimal solution to the "Rankine-Hugoniot problem", *J. Geophys. Res.*, 91, 39-58, 1986.
- Zhang, M., V. M. Vasyliunas, G. L. Siscoe, R. P. Lepping, N. F. Ness, Evidence for a diurnally rocking plasma mantle at Neptune, *Geophys. Res. Lett.*, 17, 2285, 1990.

REFERENCES FOR CHAPTER 5

- Bagenal, F., J. W. Belcher, E. C. Sittler, and R. P. Lepping, The Uranian bow shock: Voyager 2 inbound observations of a high Mach number shock, *J. Geophys. Res.*, 92, 8603-8612, 1987.
- Goodrich, C. C., Numerical simulations of quasi-perpendicular collisionless shocks, in *Collisionless Shocks in the Heliosphere, Review of Current Research, Geophys. Monogr. Ser.*, Vol. 35, edited by B. T. Tsurutani and R. G. Stone, pp. 153-168, AGU, Washington, D.C., 1985.
- Leroy, M. M., D. Winske, C. C. Goodrich, C. S. Wu, and K. Papadopoulos, The structure of perpendicular bow shocks, *J. Geophys. Res.*, 87, 5081-5094, 1982.
- Leroy, M. M., Structure of perpendicular shocks in collisionless plasma, *Phys. Fluids*, 26, 2742-2753, 1983.
- Richardson, J. D., G. L. Siscoe, S. S. Stahara, J. R. Spreiter, and A. Szabo, The magnetosheath of Neptune: Models and Observations, in preparation for publication, 1993.
- Russell, C. T., M. M. Hope, and W. A. Livesey, Overshoots in planetary bow shocks, *Nature*, 296, 45, 1982.
- Schwartz, S. J., M. F. Thomsen, and J. T. Gosling, Ions upstream of the Earth's bow shock: A theoretical comparison of alternative source populations, *J. Geophys. Res.*, 88, 2039, 1983.
- Sckopke, N., G. Paschmann, S. J. Bame, J. T. Gosling, and C. T. Russell, Evolution of ion distributions across the nearly perpendicular bow shock: Specularly and nonspecularly reflected-gyrating ions, *J. Geophys. Res.*, 88, 6121-6136, 1983.
- Spreiter, J. R., A. L. Summers, and A. Y. Alksne, Hydromagnetic flow around the magnetosphere, *Planet. Space Sci.*, 16, 223, 1966.
- Viñas, A. F., and J. D. Scudder, Fast optimal solution to the "Rankine-Hugoniot problem", *J.*

Geophys. Res., 91, 39-58, 1986.

Zhang, M., V. M. Vasyliunas, G. L. Siscoe, R. P. Lepping, N. F. Ness, Evidence for a diurnally rocking plasma mantle at Neptune, *Geophys. Res. Lett.*, 17, 2285, 1990.

ACKNOWLEDGEMENTS

I am grateful to my thesis advisor, Professor John W. Belcher for guidance in my studies and research and for financial support. I wish to thank Dr. John D. Richardson, Dr. Alan J. Lazarus, and Dr. George Gordon, Jr. for their relentless help in my research projects. For their support, encouragement, and patience, I thank Anne Bowes, Professor Hale V. D. Bradt, Professor Herbert Bridge, Professor Bruno Coppi, Dr. Ralph L. McNutt, Jr., Pamela Milligan, Karolen I. Paularena, Dr. George Siscoe, Dr. John T. Steinberg, Louis Villanueva, and Dr. Ming Zhang. I also thank Dr. Ronald P. Lepping for providing the magnetic field data used in this thesis and for numerous helpful comments and collaborative work.

This work was supported by NASA under contract 953733 from the Jet Propulsion Laboratory to the Massachusetts Institute of Technology and under the Neptune Data Analysis Program Grants NAGW-1210?

BIOGRAPHY

The author was born on October 23, 1965 in Debrecen, Hungary. He immigrated to the United States with his parents and brother in 1982 and became a naturalized citizen of this country in March, 1991. He graduated from High School in Indianapolis in 1984, and attended the University of Chicago, where he obtained a BA degree in physics in 1988. While at the University of Chicago, he worked in the Pioneer 10, 11 high energy particle group under the guidance of Professor John A. Simpson and Dr. R. B. McKibben. He came to MIT in July, 1988, and worked as a research assistant in the low-energy plasma group at the Center for Space Research analyzing the Voyager 2 data collected at Neptune. After graduation, he intends to stay at MIT for a number of month as a post doctoral fellow continuing some of the same work reported in this thesis.